HEAD MOTION CORRECTION IN MAGNETIC RESONANCE IMAGING USING NMR FIELD PROBES

Dissertation

der Mathematisch-Naturwissenschaftlichen Fakultät
der Eberhard Karls Universität Tübingen
zur Erlangung des Grades eines
Doktors der Naturwissenschaften
(Dr. rer. nat.)

vorgelegt von
Martin Georg Eschelbach
aus Leonberg

Tübingen
2018

Gedruckt mit Genehmigung der Mathematisch-Naturwissenschaftlichen Fakultät der Eberhard Karls Universität Tübingen.

Tag der mündlichen Qualifikation:	16.11.2018
Dekan:	Prof. Dr. Wolfgang Rosenstiel
1. Berichterstatter:	Prof. Dr. Klaus Scheffler
2. Berichterstatter:	Prof. Dr. Dr. Fritz Schick

CONTENTS

ABBREVIATIONS AND CONSTANTS

ABBREVIATIONS

ADC analog-to-digital converter

CT computed tomography

DTI diffusion tensor imaging

FID free induction decay

FOV field of view

fMRI functional magnetic resonance imaging

FP NMR field probe

GRE gradient echo

LNA low noise amplifier

MPT Moiré phase tracking

MRI magnetic resonance imaging

MRT magnetic resonance tomography

NMR nuclear magnetic resonance

PA power amplifier

PCB printed circuit board

PLL phase-locked Loop

PMC prospective motion correction

RF radio frequency

RMSE root-mean-squared error

SD standard deviation

SNR signal-to-noise ratio

T/R transmit/receive

UDP User Datagram Protocol

CONSTANTS

$\hbar = \frac{h}{2\pi}$	1.05×10^{-34} m^2kg/s	Reduced Planck constant
$\gamma_{^1H}$	42.57 MHz/T	Gyromagnetic ratio ^{1}H
$\gamma_{^{19}F}$	40.05 MHz/T	Gyromagnetic ratio ^{19}F
k_B	1.38×10^{-23} J/K	Boltzmann constant

1 SUMMARY

Magnetic Resonance Imaging (MRI) is a widely used imaging technology in medicine. Its advantages include good soft tissue contrast and the use of non-ionizing radiation in contrast to for example computed tomography (CT). One drawback are the long acquisition times that are needed. They depend on the diagnostic use case but are usually within the range of minutes. These long scan times make the images prone to patient motion during image acquisition which can lead to blurring or ghosting artifacts. Those artifacts might render the diagnostic value of the images useless which requires the image to be reacquired or the patient to be sedated before the scan to prevent motion artifacts. This is where motion correction comes into play. One can distinguish between retrospective and prospective motion correction (PMC) methods. Retrospective motion correction tries to improve image quality after the image acquisition by post-processing and possibly using additional motion tracking information, if available. Prospective motion correction relies on a motion tracking modality that is used to provide motion information to update imaging parameters during image acquisition. Both motion correction methods can also be used in combination with each other. This thesis, however, will focus on the implementation and validation of a system for prospective head motion correction.

The system consisted of four nuclear magnetic resonance (NMR) field probes using the design of Barmet et al. [1]. Those field probes were attached to the head and used to measure the spatiotemporal evolution of magnetic fields. By switching spatially varying magnetic fields, this information can be used to track the field probes' positions and calculate the corresponding head motion in order to perform prospective motion correction.

The first step was the development and evaluation of a stand-alone system for signal

transmission to and signal acquisition from the field probes. This stand-alone solution used microelectronic components and was needed to acquire field probe measurements independent of the MR scanner hardware. The second step was to improve the accuracy of position determination of the field probes. The position was determined by using linear magnetic field gradients which are applied on each spatial axis. Real gradients, however, have a characteristic nonlinear behavior which needed to be characterized and evaluated. This was done by using a single field probe in different known positions as well as by using a field camera consisting of 16 field probes. In the last step, the entire prospective motion correction system needed to be evaluated in different imaging scenarios and was finally compared against another PMC modality that employs an optical camera and a Moiré phase tracking (MPT) marker attached to the head.

The results show that prospective motion correction with NMR field probes is feasible and can, in most cases, compete with optical tracking. However, there are some drawbacks, some inherent to our implementation such as long calculation times and semi-rigid field probe fixation, some inherent to field probe tracking in general, such as insufficient knowledge of gradient behavior or the need to modify pulse sequence gradients. In some usage scenarios, e.g. when a direct line of sight from a camera to a marker or the face of the patient is not possible, the field probe might be advantageous but in other use cases, camera based systems might be the better and easier-to-use alternative.

2 ZUSAMMENFASSUNG

Die Magnetresonanztomographie (MRT) ist ein in der Medizin weitverbreitetes bildgebendes Verfahren. Ihre Vorteile sind unter anderem der gute Gewebekontrast und die Verwendung von nichtionisierender Strahlung im Gegensatz zur Computertomographie (CT). Ein Nachteil ist die Länge der Zeit, die notwendig ist um ein Bild aufzunehmen. Sie hängt natürlich vom jeweiligen diagnostischen Anwendungsfall ab, bewegt sich aber normalerweise im Bereich von Minuten. Diese langen Aufnahmezeiten machen die Bilder anfällig für Patientenbewegungen, welche zu unscharfen Bildern oder sogenannten Ghostingartefakten, bei denen sich Bildteile wiederholen, führen. Diese Artefakte können dazu führen, dass eine Diagnose nicht mehr möglich ist, was entweder eine erneute Aufnahme des Bildes notwendig macht oder eine Sedierung des Patienten, um Bewegung zu vermeiden. Hier kommen Bewegungskorrekturverfahren ins Spiel, wobei man dabei zwischen retrospektiver und prospektiver Korrektur unterscheidet. Retrospektive Bewegungskorrekturverfahren versuchen nach der bereits erfolgten Bildaufnahme die Bildqualität zu verbessern indem die Bilder nachbearbeitet werden. Hierbei können auch Bewegungsinformationen, die zusätzlich zum Bild aufgenommen wurden, verwendet werden. Prospektive Bewegungskorrektur benötigt in jedem Fall diese zusätzlichen Bewegungsinformationen, die noch während der Bildaufnahme dazu verwendet werden die Bildgebungsparameter so zu verändern, dass der Bildausschnitt der Bewegung folgt. Beide Korrekturmethoden können auch in Kombination angewandt werden. Diese Arbeit beschäftigt sich jedoch mit der Entwicklung und Validierung eines Systems zur prospektiven Bewegungskorrektur.

Das entwickelte System bestand aus vier Kernspinresonanz-Magnetfeldsensoren (NMR field probes) nach dem Entwurf von Barmet et al. [1]. Diese Sensoren wurden am Kopf der Probanden befestigt und konnten die räumliche und zeitliche Veränderung des Magnetfeldes messen. Das Ziel war es, dadurch die Sensorpositionen zu bestimmen und die

zugehörigen Kopfbewegungen zu berechnen, um mit diesen Informationen die prospektive Bewegungskorrektur zu implementieren. Dabei war der erste Schritt die Entwicklung eines eigenständigen Sende- und Empfangssystems zur Signalgeneration und -akquise der Sensoren. Dieses System bestand aus mikroelektronischen Komponenten und war nötig, um die Messungen der Sensoren unabhängig von der Hardware des Kernspintomographen durchführen zu können. Im zweiten Schritt sollte die Genauigkeit der Positionsbestimmung der Sensoren verbessert werden. Die Position der Sensoren wurde durch lineare Magnetfeldgradienten bestimmt, die nacheinander auf allen räumlichen Achsen geschaltet wurden. Echte Gradienten besitzen allerdings ein charakteristisches nichtlineares Verhalten, das ausgemessen werden musste, um das lineare Modell der Positionsbestimmung zu verbessern. Dazu wurden Messungen mit einem Sensor in verschiedenen bekannten Positionen durchgeführt sowie zusätzlich Messungen mit einer sogenannten Feldkamera, welche aus 16 dieser Sensoren besteht. Im letzten Schritt wurde dann das fertige System zur Bewegungskorrektur für verschiedene Bildgebungssequenzen getestet und schließlich mit einem anderen Bewegungskorrektursystem verglichen, welches auf einer optischen Kamera basiert, die die Spur eines am Kopf befestigten Markers verfolgt.

Die Ergebnisse zeigen, dass prospektive Bewegungskorrektur mit NMR field probes möglich ist und in den meisten Fällen mit der optischen Methode mithalten kann. Es gibt jedoch Nachteile, wovon einige mit unserer speziellen Implementierung zusammenhängen, wie beispielsweise die langen Berechnungszeiten und die nicht ganz starre Befestigung der Sensoren am Kopf, und andere Nachteile, die mit dem generellen Funktionsprinzip der Sensoren einhergehen wie die ungenügende Kenntnis des Gradientenverhaltens oder die Notwendigkeit, die Pulssequenzen am Kernspintomographen abzuändern. In manchen Anwendungsfällen können field probes jedoch auch Vorteile haben, beispielsweise wenn keine direkte Sichtverbindung zu einem Marker oder dem Gesicht des Patienten möglich ist, in anderen Fällen werden kamerabasierte Systeme jedoch oft die bessere Alternative sein, da sie einfacher zu handhaben sind.

3 SUMMARIZED PUBLICATIONS

This dissertation is written as a cumulative thesis based on the following three publications. A comprehensive list of all publications can be found in the appendix.

Publication 1:

J. Handwerker, **M. Eschelbach**, P. Chang, A. Henning, K. Scheffler, M. Ortmanns, J. Anders. **An active TX/RX NMR probe for real-time monitoring of MRI field imperfections** IEEE Biomedical Circuits and Systems Conference (BioCAS), Rotterdam, pp. 194-197, 2013. doi: 10.1109/BioCAS.2013.6679672

Publication 2:

P. Chang, S. Nassirpour, **M. Eschelbach**, K. Scheffler and A. Henning. **Constrained Optimisation for Position Calibration of an NMR Field Camera** Magnetic Resonance in Medicine, 80:380-390, 2018. doi: 10.1002/mrm.27010

Publication 3:

M. Eschelbach, A. Aghaeifar, J. Bause, J. Handwerker, J. Anders, E.-M. Engel, A. Thielscher and K. Scheffler. **Comparison of Prospective Head Motion Correction with NMR Field Probes and an Optical Tracking System** Magnetic Resonance in Medicine, 81:719–729, 2019. doi: 10.1002/mrm.27343

4 INTRODUCTION

This chapter will give a short introduction into nuclear magnetic resonance (NMR), magnetic resonance imaging (MRI), NMR field probes and head motion correction in MRI. A more detailed overview can be found for example in Levitt [2], Haacke et al. [3] and Robitaille et al. [4]. Parts of this introduction are also loosely following the elaborations on the theory of MRI that were compiled for my Diploma thesis [5].

4.1 NUCLEAR MAGNETIC RESONANCE

The main principle of NMR is the interaction of the nuclear spin $\vec{I}$ with an external magnetic field[1] $\vec{B}_0$. For an interaction with the magnetic field the total nuclear spin has to be non-vanishing (i.e. $\vec{I} \neq 0$). This is the case if the number of protons and/or the number of neutrons in a nucleus is odd (e.g. in ^{1}H, ^{19}F and ^{23}Na).

With a given nuclear spin $\vec{I}$ there is a corresponding magnetic moment $\vec{\mu}$:

$$\vec{\mu} = \gamma \vec{I}, \tag{4.1}$$

which is connected to the nuclear spin by the so called gyromagnetic ratio γ. The gyromagnetic ratio is an experimental constant which is a characteristic property of a certain nucleus.

According to quantum mechanics, the projection of $\vec{I}$ onto any axis (for example z) is

[1] In the context of MRI, the terms *magnetic field strength* and *magnetic field* always refer to the magnetic flux density B, not to the H-field which might be more correct historically and physically.

quantized:

$$I_z = m_I \hbar$$

with $m_I = -I, -I+1, ..., I-1, I$ being the magnetic quantum number and $\hbar$ the reduced Planck constant. For every m_I there is a corresponding eigenstate of the nucleus. So the total number of eigenstates is $2I + 1$. If there is no external magnetic field, all eigenstates are associated with the same energy. If we introduce an external magnetic field (assumed being oriented along the z-axis, $\vec{B_0} = B_0 \hat{e}_z$), however, there will be a splitting into $2I + 1$ energy levels since the potential energy of a nuclear spin in a magnetic field is related to its magnetic moment $\vec{\mu}$:

$$E = -\vec{\mu} \cdot \vec{B_0} = -\mu_z B_z = -\gamma m_I \hbar B_z.$$

This splitting of energy levels in the presence of a magnetic field is called Zeeman effect. The energy difference in between two levels can be calculated:

$$\Delta E = \hbar \omega_0$$

for a constant field $\vec{B_0}$. The frequency ω_0 is the so called Larmor frequency, which is defined by the *Larmor equation*:

$$\omega_0 = \gamma B_0 \tag{4.2}$$

The Larmor equation is the central equation for NMR since it describes the linear dependence of the frequency on the magnetic field.

Considering the Ehrenfest theorem, the expectation value of the magnetic moment $\langle \vec{\mu} \rangle$ follows the laws of classical physics. Therefore, in a homogenous static magnetic field we can modify equation 4.1 to

$$\langle \vec{\mu} \rangle = \gamma \vec{I}$$
$$\vec{N} = \langle \vec{\mu} \rangle \times \vec{B_0},$$

with $\vec{N}$ being the torque on the nuclear spin. If we now use $\vec{N} = d\vec{I}/dt$ to connect those equations, we arrive at

$$\frac{d\langle\vec{\mu}\rangle}{dt} = \gamma\langle\vec{\mu}\rangle \times \vec{B}_0 = \gamma B_0 \langle\vec{\mu}\rangle \times \hat{e}_z = \omega_0 \langle\vec{\mu}\rangle \times \hat{e}_z.$$

This equation describes a precession of the expectation value of the magnetic moment $\langle\vec{\mu}\rangle$ around the axis of the static magnetic field, $\vec{B}_0$, with the Larmor frequency ω_0.

Now we want to zoom out from inspecting a single nucleus and consider an assembly of spins on a macroscopic scale. We introduce a quantity called the *magnetization* $\vec{M}$. The magnetization in a volume V with i nuclei and corresponding magnetic moments $\vec{\mu}_i$ is calculated as the mean value of the magnetic moments in that volume:

$$\vec{M} = \frac{1}{V}\sum \vec{\mu}_i.$$

For an assembly of spins in a strong external magnetic field, $\vec{B}_0 = B_0\hat{e}_z$, the equilibrium magnetization is non-vanishing and also oriented in $\hat{e}_z$ direction. The nuclear spins tend to align along the magnetic field, since this configuration resembles a smaller potential energy as shown before. At room temperature, however, there is, according to Boltzmann statistics, only a small excess ΔN of spins aligned with the field. Their number can be calculated by

$$\Delta N \cong N\frac{\hbar\omega_0}{2k_bT} = N\frac{\hbar\gamma B_0}{2k_bT},$$

with N being the total number of spins in the target volume, the Boltzmann constant k_b and the temperature T. As one can see it is proportional to the strength of the static magnetic field. The spin excess at 1.5 Tesla for example is around 5 per million at body temperature [6]. But since (at least in proton experiments) the spin density is very high, the resulting macroscopic magnetization M_0 is still big enough to be detected.

If the interaction of the single nuclei with their environment is neglected one can form an equation for the variation of the magnetization:

$$\frac{d\vec{M}}{dt} = \gamma\vec{M} \times \vec{B}_{ext}. \tag{4.3}$$

In a real sample, however, two additional interaction effects come into play. One, is

the longitudinal relaxation which causes the longitudinal magnetization M_z to return to the equilibrium state $M_0\hat{e}_z$ through thermal interaction with other molecules. The corresponding time constant for the exponential relaxation is called T_1. The other effect is the transversal relaxation which describes a decay of transversal magnetization $\vec{M}_\perp$ due to dephasing of the individual magnetic moments of the nuclear spins due to their interactions with each other which causes microscopic variations in the magnetic environment experienced by each spin. The corresponding time constant for the exponential decay is T_2. If we consider additional inhomogeneities of the static magnetic field, we will get an even faster dephasing and a shorter apparent relaxation time called T_2^*. If these effects are taken into account, the time dependence of the magnetization for spin-1/2 nuclei can be described by the following set of differential equations first postulated by Felix Bloch [7]:

$$\frac{d\vec{M}(t)}{dt} = \gamma\vec{M}(t) \times \vec{B}_{ext}(t) + \frac{1}{T_1}(M_0 - M_z(t))\hat{e_z} - \frac{1}{T_2}\vec{M_\perp}(t) \tag{4.4}$$

In the equilibrium state, however, there is no temporal change of the magnetization vector which could be detected by a nearby pickup coil. Thus, the magnetization vector has to be rotated towards the x-y plane. This can be done by exciting the sample with an electromagnetic field perpendicular to the static field and oscillating with the corresponding Larmor frequency ω_L, which (seen from the rotating frame) leads to a nutation of the magnetization towards the x-y plane (Figure 4.1). The angle of this nutation is referred to as the flip angle α. A coil is used for emitting these radio frequency (RF) pulses and the emitted magnetic field is referred to as B_1^-. Now that the magnetization is flipped, it starts precessing around the z-axis. If a receive coil is placed nearby, according to Faraday's law of induction, the precessing magnetization creates a varying magnetic field which will induce a voltage in the receive coil. This is the receive signal which is then amplified, demodulated and digitized.

In the simplest case with one excitation and subsequent acquisition of the signal, we will get a signal that is called free induction decay (FID). The FID is the voltage evolution induced by the precessing transversal magnetization $M_\perp$. After signal demodulation with the demodulation frequency $\omega_d = \omega_0 + \delta\omega$ with $\delta\omega$ being the offset from the Larmor frequency ω_0, we get a real and imaginary part of the FID that is proportional to a the complex representation of the transversal magnetization, $M_\perp = M_x + iM_y$. Thus, with a precessing transversal magnetization we will get two signals that have a sinusoidal

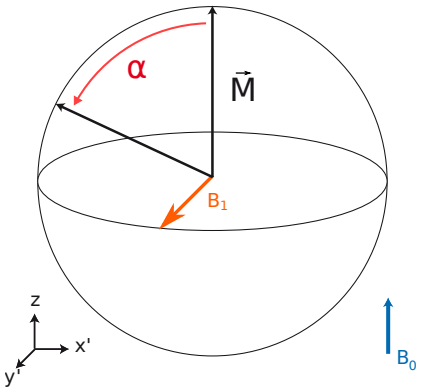

Figure 4.1: The magnetization $\vec{M}$ is flipped towards the x-y plane (shown in the rotating frame) by a flip angle α using an excitation pulse with the Larmor frequency ω_L.

shape with an envelope representing the decay of the transversal magnetization with the relaxation time T_2^* as shown in Figure 4.2.

The general signal evolution, $S(t)$, after demodulation can be described by

$$S(t) = \int M_\perp(\vec{r}) B_\perp(\vec{r}) e^{-i\phi(\vec{r},t)} d^3r, \tag{4.5}$$

where $B_\perp$ is the component of the receive coil field B_1 that lies in the transverse plane.

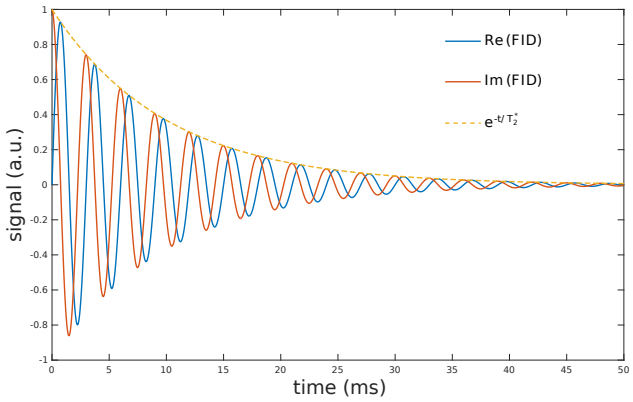

Figure 4.2: FIDs following the form $s(t) = \sin(\delta\omega \cdot t - \phi) \cdot e^{-t/T_2^*}$ with a T_2^* of 10 ms.

4.2 MAGNETIC RESONANCE IMAGING

So how do we get from the measured signal to a two or three-dimensional MR image? In order to do this, we need additional spatial encoding. This is done via magnetic gradient fields that are applied in addition to the static magnetic field and are created by dedicated gradient coils. These magnetic gradient fields (commonly just referred to as *gradients*) are usually considered to vary linearly along each spatial axis. This will give rise to a spatial dependence of the local Larmor frequency. For applied linear gradients $\vec{G}_{x,y,z}$ with known strengths along each axis (usually given in mT/m) we can calculate this local frequency

$$\omega_L(\vec{r}, t) = \gamma(B_0 + \vec{G}_{x,y,z}(t) \cdot \vec{r}), \tag{4.6}$$

and the accumulated phase

$$\phi(\vec{r}, t) = \gamma \int_0^t (B_0 + \vec{G}_{x,y,z}(\tau) \cdot \vec{r})\, d\tau. \tag{4.7}$$

If we now define $\vec{k}(t)$:

$$\vec{k}(t) = \frac{\gamma}{2\pi} \int_0^t \vec{G}_{x,y,z}(\tau)\, d\tau, \tag{4.8}$$

which is a vector in the so called k-space, we can modify the signal equation 4.5 to

$$S(t) = \int M_\perp(\vec{r}) B_\perp(\vec{r}) e^{-i2\pi\vec{k}(t)\vec{r}}\, d^3r. \tag{4.9}$$

Here, we can see that the acquired signal $S(t)$ is connected to the spatial distribution of the transversal magnetization $M_\perp$ (weighted with $B_\perp$) by the Fourier transform [8].

This principle of the spatial encoding can be demonstrated on the example of a simple pulse sequence. A pulse sequence is a programmed time scheme that is interpreted by the scanner and defines when, how strong and how long the RF pulses and gradients are supposed to be. A pulse sequence diagram for a 2D gradient echo sequence is shown in figure 4.3. If we imagine a patient inside the scanner's bore lying along the z-axis and we now apply a linear gradient field $B_z(z) = G_z z$ along the z-axis, the resonance frequency of the nuclei will change linearly with the z-coordinate due to the Larmor equation:

$$\omega_L(z) = \gamma(B_0 + B_z(z)) = \omega_0 + \gamma G_z z. \tag{4.10}$$

If we now apply an excitation pulse with a frequency of $\omega_L(z_0)$, only nuclei on a plane with $z = z_0$ will be excited. So we end up with an excited slice at z_0 in the x-y-plane whose thickness is determined by the frequency bandwidth of the RF pulse. The corresponding gradient is also called the slice selection gradient. The spins are now dephased due to the previously applied gradient. To reverse this effect, a gradient along the same axis but with opposite amplitude is played out. Next, a gradient perpendicular to the slice selection gradient (e.g. along the x-axis) is applied which will result in different local precession frequencies along that axis. After turning this gradient off again, the precession frequencies will return to their previous values but there will be a relative phase offset that increases linearly along the respective gradient axis. This process is called phase encoding and the corresponding gradient is called the phase encoding gradient. For each repetition, this gradient has a different amplitude which is indicated by the arrow in figure 4.3. This change in amplitude will lead to different relative phase offsets

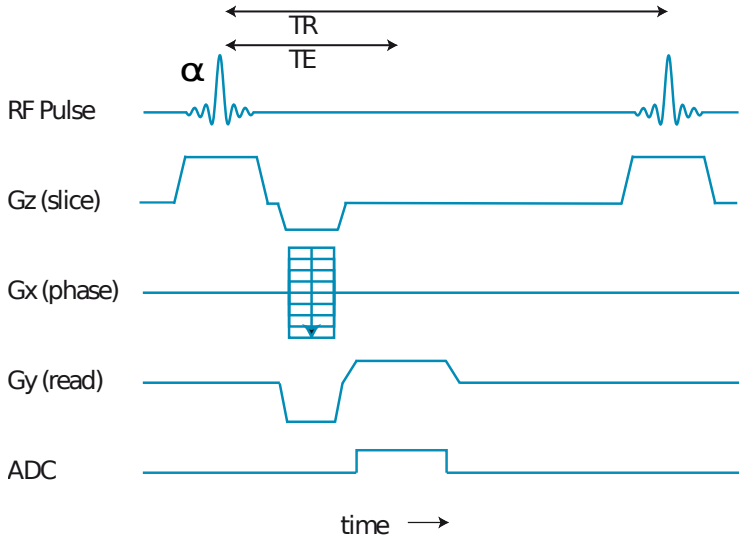

Figure 4.3: Sequence diagram of a basic 2D gradient echo sequence. An RF pulse with flip angle α is played out while the desired slice is selected with G_z. Then the phase gradient G_x is applied with a different amplitude for each repetition. After the echo time TE the readout gradient G_y is applied while recording the signal with the ADC. The entire process is repeated after the repetition time TR.

for each repetition and thus allows for spatial encoding along the respective axis. Before the signal acquisition, a gradient (in this case G_y) is applied to deliberately dephase the spins. During the readout of the analog-to-digital converter (ADC), the same gradient, also called readout gradient, is applied with the opposite amplitude. This leads to a rephasing of the spins and the formation of a signal echo after the echo time, TE.

For every repetition of the pulse sequence in figure 4.3 we get one signal over time course from the entire slice. This signal contains different frequencies due to the readout gradient. This is one line in k-space along the readout direction. This process is repeated multiple times with different amplitudes of the phase encoding gradient until the entire k-space is filled. If we now apply an inverse 2D Fourier transformation, we will get a two-dimensional spectrum showing the signal strength for every pair of frequency and phase. If we consider the magnitude of this spectrum only, this is already the final image, showing the signal intensities for each position along the direction of the readout and phase gradient.

This is just an easy example for a better understanding of spatial encoding. With a linear combination of gradients, slice-orientations and k-space trajectories can be arbitrarily modified. Also, instead of slice selective excitation one can also acquire 3D images by using two phase encoding gradients for additional spatial information.

4.3 NMR FIELD PROBES

NMR field probes are basically a simple NMR experiment. A solenoid is wound around a sealed glass capillary containing an NMR active liquid (in our case containing either ^{1}H or ^{19}F). The solenoid is then used for excitation of the sample as well as for the reception of the NMR signal.

The field probes used in this work were based on design principles from Barmet et al. [1, 9]. They consisted of a small glass capillary (inner diameter: 800 μm) with a length of approximately 1 cm which and was filled with the NMR active liquid. The capillary was sealed on both ends using UV-hardening glue. Around the capillary there was a copper solenoid (6 turns, wire diameter 200 m), which was designed to maximize the signal-to-noise ratio (SNR) following the guidelines of Minard and Wind [10]. The capillary was encapsulated in epoxy that was susceptibility matched to the copper wire to improve B_0 homogeneity inside the capillary [11]. The entire probe head was connected to a small printed circuit board (PCB) with variable capacitors for tuning the circuit to the desired resonance frequency and for matching it to an impedance of 50 Ω to minimize transmission losses.

If we acquire an FID with the field probe, we can use the measured phase ϕ of the complex signal to determine the magnetic field strength B at the probe's position $\vec{r}$,

$$\gamma \int_0^t B(\vec{r}, \tau) d\tau = \phi(\vec{r}, t) + \omega_d t \tag{4.11}$$

$$B(\vec{r}, t) = \frac{1}{\gamma}(\dot{\phi}(\vec{r}, t) + \omega_d) \tag{4.12}$$

with a known demodulation frequency ω_d. This information can now be used to measure field drifts and fluctuations or the behavior of magnetic field gradients (see Section 4.2).

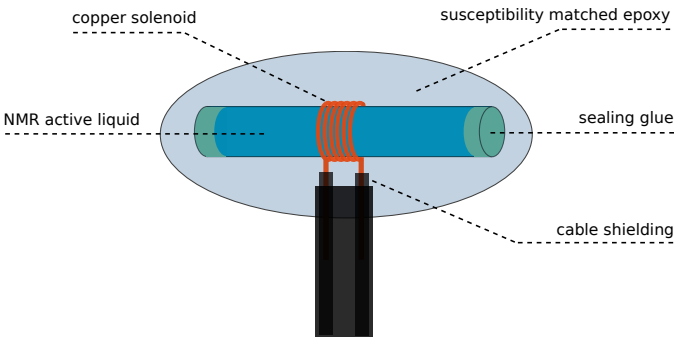

Figure 4.4: Basic schematic of an NMR field probe.

A description of the entire measurement setup can be found in the publication summaries (Chapter 6).

4.4 HEAD MOTION CORRECTION IN MRI

Head motion during image acquisition can pose a serious problem affecting image quality. It can lead to incorrect phase accumulation, an irregular sampling of k-space, spin history effects and B_0 fluctuations [12]. These effects introduce various image artifacts such as ghosting and blurring. In a clinical environment this is especially an issue for patient groups that are prone to move or have difficulties to hold still such as children, patients with dementia or stroke patients. But even in research environments with trained subjects, minor head motion can pose a limitation when aiming for high image resolutions or acquiring images for longer periods of time.

The easiest approach to prevent motion artifacts is the fixation of the head. This is usually done with special cushions. Additional fixation such as bite-bars [13] or neck restraints can be used to further eliminate head motion. However, extreme measures in this category usually come with a decrease in patient comfort.

Thus, several methods have been proposed to correct for head motion and the resulting artifacts [14]. They can coarsely be divided into retrospective and prospective motion correction methods. Retrospective motion correction uses the already acquired image(s) and tries to remove or reduce motion artifacts by post-processing. This can be done with

the image data alone, for example by iteratively improving a metric of image quality such as the entropy of spatial gradients [15], or by additionally including knowledge about the motion trajectory acquired by a motion tracking modality. Prospective motion correction on the other hand tries to update the position of the imaging field of view during image acquisition and thus also needs a method of motion tracking to provide the necessary data for the update.

Motion tracking can be achieved by a broad variety of mechanisms, some of which will be introduced briefly. There are MR-based tracking methods such as self-navigation, where the motion is inferred from the imaging data by using repeated sampling of parts of k-space (e.g. PROPELLER [16]). Another MR-based method is the acquisition of additional navigator echoes, e.g. acquiring a projection of the image along one axis [17], or FID navigators [18] that utilize the use of receiver coils with multiple coil elements and the signal change in each element with head motion. Then, there is image based motion tracking, which is usually used when multiple images of the same volume are acquired, as for example in fMRI or diffusion tensor imaging (DTI). Here, one can perform a coregistration of the acquired volumes against each other to infer motion parameters and subsequently correct for the misalignment. Intra-volume motion is usually neglected or considered insignificant in these approaches. Another method for motion tracking is the use of optical cameras that track one [19] or multiple markers [20] attached to the head or features of the face itself [21]. The advantage here is the high precision and the relative independence from the used pulse sequence. Motion tracking can also be achieved with so called active markers, which can be RF coils, small NMR active containers or a combination of those. If the position of multiple of those markers can be estimated, their consecutive positions can be coregistered to infer head motion parameters. An overview of selected motion tracking methods by their respective qualities is shown in Figure 4.5. If the tracking source is intended for the use in prospective motion correction, one should additionally consider the latency as a fourth quality.

NMR field probes can be characterized as active markers. In order to perform head motion correction with NMR field probes, the probes have to be attached to the head. In our study, this was done by taping four probes to the nose bridge and temples of the subject since a more elaborate attachment scheme was prevented by the spatial constraints of the receive helmet. To estimate head motion, the position of each field probe has to be calculated. This is done by switching bipolar localization gradients (for details see section 6.3). In addition the effects of nonlinear gradient behavior have to be

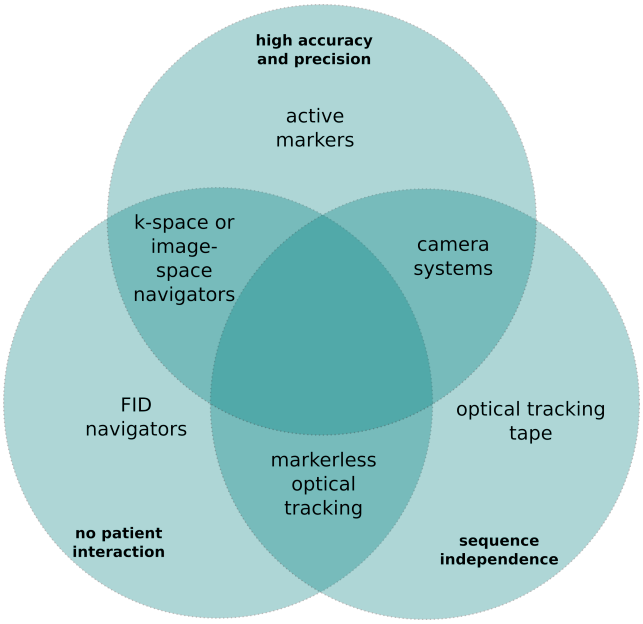

Figure 4.5: A Venn diagram sorting different head motion tracking modalities by their qualities according to Maclaren et al. [22].

taken into account as well in order to get a more precise position estimate (see section 6.2). The position changes over time of a set of field probes (at least three are necessary but accuracy will increase with additional probes) can then be used to calculate the six degrees of freedom rigid motion parameters. This was done using an algorithm from Umeayama [23]. The resulting motion parameters are then sent to the scanner via UDP and can subsequently be used to update the field of view to follow the head's motion.

5 OBJECTIVES

The goal of this work was to implement a working system for prospective head motion correction using NMR field probes.

The first step was to separate the field probe measurements from the actual MRI experiment by establishing an alternative to using the MR scanner's hardware for excitation of the field probes and demodulation of their signal. To this end an external transmit and receive chain consisting of microelectronic building blocks was established. **Publication 1** shows that it is possible to do sample excitation and signal processing with this specifically designed hardware.

To get an accurate position estimate of the field probes it is crucial to have an understanding of gradient behavior. **Publication 2** investigates the effects of gradient nonlinearities on the position measurements of field probes and especially an array of field probes used as a so called field camera. Here, we propose different methods on how to find the most accurate position estimate of a field probe (array).

Publication 3 finally demonstrates that using the knowledge gained from the previous work it is possible to implement prospective head motion correction with NMR field probes. The motion tracking and prospectively corrected images are then compared to another established method in head motion correction which is optical motion tracking using a camera and an MPT (Moiré phase tracking) marker.

6 PUBLICATION SUMMARIES

This chapter will provide a quick walkthrough of the implementation and the results of prospective head motion correction with NMR field probes by using the three publications as a guideline. All figures are taken from the respective publications and are used with the permission of *IEEE* and *John Wiley & Sons, Inc.*.

6.1 PUBLICATION 1: AN ACTIVE TX/RX NMR PROBE FOR REAL-TIME MONITORING OF MRI FIELD IMPERFECTIONS

NMR field probes [1] have a wide range of applications by measuring the magnetic field and its temporal changes inside the MR scanner with a high precision. These applications include the measurement of gradient imperfections such as eddy current effects [24], long term drifts of the scanner frequency [25] or the gradients or field fluctuations induced by patients (e.g. breathing, movement). However, when using the MR scanner's receive chain and spectrometer, the field probes are blocking hardware which could otherwise be used for imaging purposes. Thus, the goal of this work was to establish a separate transmit and receive chain as well as a built-in spectrometer for NMR field probes using microelectronic components.

The probe head used in this study was built as described in the introduction (Section 4.3). It contained copper sulfate ($CuSO_4$) doped water as an NMR active sample. The doping was done to shorten the T_1 relaxation of the sample to allow higher measurement repetition rates. The probe was connected to a custom built PCB hosting the transmit- and receive electronics as well as a circuit with variable capacitors to tune it to the resonance frequency ($f_{^1H} = 399.72$ MHz at 9.4 T) and match it to an input impedance of 50 Ω. A picture of the PCB and a schematic of the electronic components can be

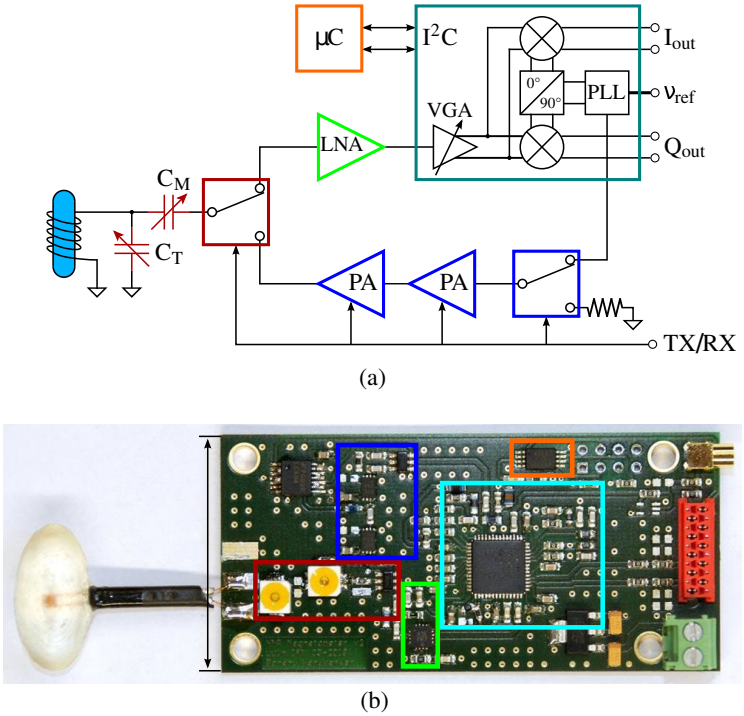

Figure 6.1: (a) Block diagram of the NMR magnetometer and (b) photograph of the transceiver PCB with the attached field probe. In the block diagram and the photograph, corresponding blocks are highlighted with the same color. ©2013 IEEE

found in Figure 6.1.

The PCB further housed a transmit-/receive switch to switch between transmission (excitation of the sample) and signal reception (receiving the induced voltage in the microcoil). In receive mode the signal was first amplified by a low noise amplifier (LNA) before being fed into an integrated RF receiver which contained a variable gain amplifier (VGA), a quadrature demodulator and a phase-locked loop (PLL) for frequency generation. The PLL was provided with an external reference frequency of $f_{ref} = 9.993$ MHz which was upconverted by a factor of 40 to the local oscillator frequency f_{LO} which was close to the proton Larmor frequency, $f_{^1H}$. f_{LO} was used for the excitation of the NMR sample and for the demodulation of the received signal. The demodulation of the signal in the scanner improved SNR and reduced the necessary bandwidth for the ADC. An additional microcontroller (μC) was used to program the registers of the receiver on

each power-up.

In transmit mode, the frequency f_{LO} is fed into two power amplifiers (PA) which are connected in series. During reception, both PAs are shut off to reduce power consumption and to avoid interference with the received signal. The transmit power which is controlled by the programmable output of the PLL was set to 15.5 dBm in all experiments as a compromise between pulse length and distortion.

For the experiments, the field probe and the PCB board were placed close to the isocenter of a 9.4 T human MR scanner (Magnetom, Siemens Healthcare, Elangen, Germany). The PLL was provided with the reference frequency by an external signal generator. The PCB was connected to an interface box housing additional anti-aliasing filters (AAFs) outside the MR scanner room with a shielded twisted pair Ethernet cable. The interface box was then connected to a commercial ADC (NI PCIe-6363, National Instruments, Austin, TX, USA). Signal transmission and data acquisition were executed and supervised by a custom LabVIEW program. The synchronization with the MR scanner (as far as necessary) was achieved with a TTL trigger signal played out during pulse sequences of the scanner.

Three measurements were performed. One plain FID acquisition to compare the signal duration and linewidth of the spectrum to previous measurements and to values found in literature. Then another measurement with multiple acquisitions while switching a gradient and checking the stability of the measured frequency over time, and a third measurement with different gradient strengths applied during multiple measurements to evaluate the linear dependency between frequency and applied gradient as well as the standard deviations of the respective frequency measurements.

The length of the FID and the full width at half maximum were comparable to previous measurements using the scanner's spectrometer and receive chain [26] if one takes into account that the samples were doped in this study which shortened T_2* as well to some extent. This implies that the additional electronic components close to the field probe did not significantly influence the signal. The measurement of frequency stability while switching a gradient of 2 mT/m in z-direction showed a standard deviation of $\sigma = 0.31$ Hz. If we define the frequency resolution to be 3σ, this corresponds to a magnetic field resolution of $2\pi 3\sigma/\gamma_{^1H} = 22$nT which was also in the range of previous measurements [26]. The measurement of the Larmor frequency as a function of gradient strength yielded

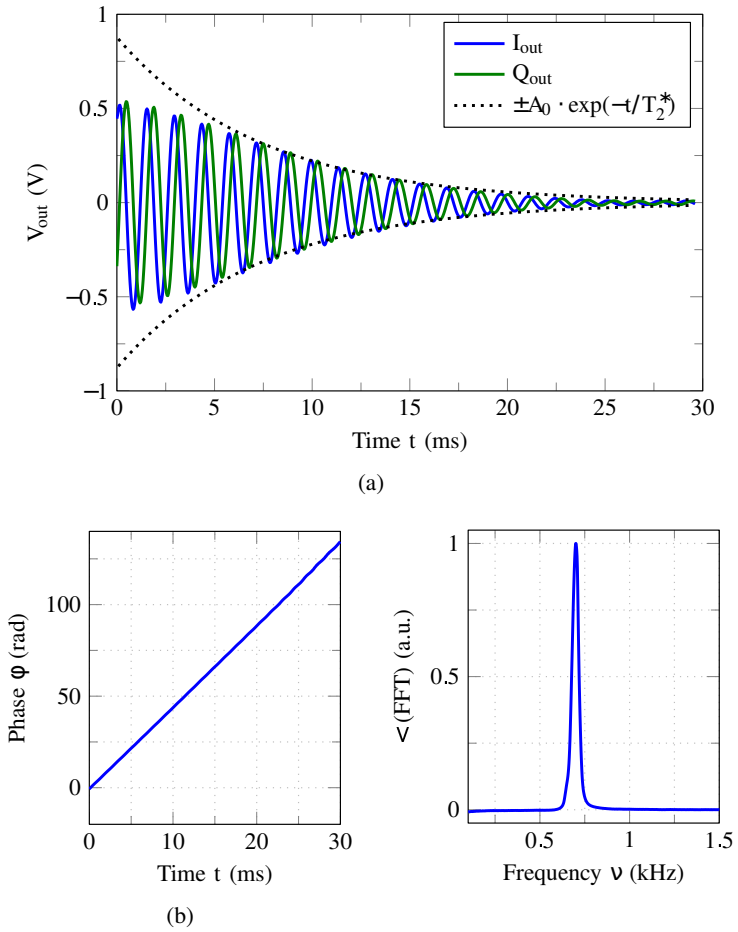

Figure 6.2: (a) Time-domain FID of the field probe containing $CuSO_4$ doped water located in the scanner isocenter and fit of the envelope signal ($T_{ACQ} = 1$ s, $F_S = 1$ MHz; measured $T_2^* = 7.4$ ms). (b) Corresponding unwrapped phase of the complex signal and (c) real part of the FFT showing the resonance frequency peak $\hat{\nu}_0 = 708$ Hz with $FWHM_\nu = 43$ Hz ©2013 IEEE

a very linear behavior. This is important for measuring the field probe's position where the measured position should ideally be independent of the chosen gradient strength. As expected, The measurements also showed that line broadening increased with gradient strength as well.

In conclusion we showed that a stand-alone PCB-based NMR field probe setup could achieve similar performance as a setup using the scanner's electronics. In addition, no influence of the presence of the PCB with the electronic components inside the scanner on the acquired signal could be detected. Another advantage of the presented system is the down-conversion of the acquired signal in the scanner which eliminates the need to route RF-cables through the bore which could otherwise hamper concurrent imaging experiments. Thus, the system qualifies for a use in prospective motion correction which requires online tracking data acquired during imaging experiments.

Contributions:

J. Handwerker designed and implemented the PCB, filter board and software for signal processing and wrote most of the manuscript with advice from J. Anders and M. Ortmanns. P. Chang helped with conducting the measurements and with the design of the field probes. A. Henning and K. Scheffler advised in the measurement setup. I built the NMR field probes, conducted the measurements and wrote parts of the manuscript.

6.2 PUBLICATION 2: CONSTRAINED OPTIMIZATION FOR POSITION CALIBRATION OF AN NMR FIELD CAMERA

An exact position information from each field probe is an important factor for reliable and accurate motion correction. Knowing the field probe positions is also crucial for field cameras which are basically an array of multiple field probes. Field cameras are used to measure the spatiotemporal evolution of the magnetic field in a volume. This leads to a variety of applications such as the correction of eddy current effects [27–29], frequency stabilization [30] and field stabilization by using the acquired information to generate compensating B_0 shim fields. The measurements of a field camera are acquired by probing the field at certain field probe positions and for multiple time steps and subsequently interpolating its evolution in space as well as in time. Therefore, an accurate position information for the field probes is needed to calculate the spatial distribution of the measured B-field. The position of the field probes is usually determined by switching gradients of known strengths in all three dimensions. Close to the isocenter, gradients can be considered to vary linearly along their respective spatial axis but further away nonlinear effects will influence the position determination. The goal of this work was to investigate the influence of these effects on position determination and to propose a method on how to minimize measurement errors by compensating for gradient nonlinearities and by using additional information to constrain possible field probe positions.

In this study, we measured the shim fields produced by a commercial 28 channel shim insert that was inserted into a 9.4 T whole body MRI scanner. This was done using a field camera consisting of 12 field probes (see Figure 6.3). The field probes contained water doped with $CuSO_4$x$5H_2O$ to shorten T_1 [9]. The field camera measurements were evaluated using different field probe position estimation strategies and the resulting field maps were compared against B_0 maps acquired with a high resolution double-echo 2D gradient echo (GRE) sequence.

To locate the actual positions of the field probe coils in respect to each other, a CT scan of the entire field camera was taken in order to avoid the influence of gradient distortions which would have been present in MR images. The resolution of the scan was 1 x 1 x 0.6386 mm^3 in x, y and z direction, respectively. The measured positions could now be used as a reference and as a comparison against results from MR measurements.

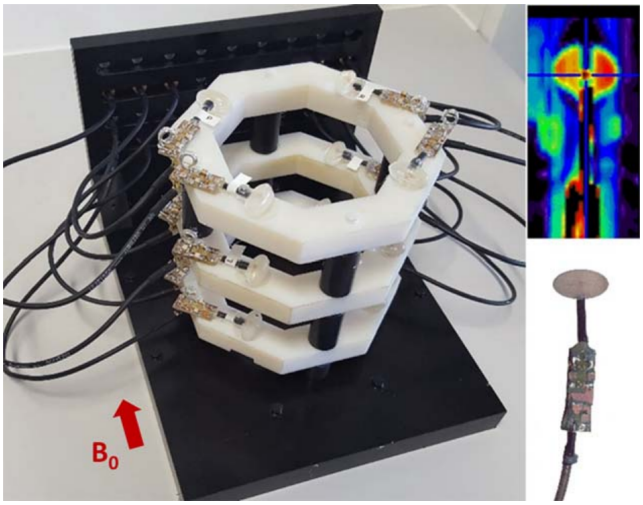

Figure 6.3: The field camera (left) consists of 12 field probes (bottom right). The direction of the B_0 field is also indicated. The CT scan of the field probe (top-right) shows that the sample within the epoxy mold can be easily identified.

For the comparison against the B_0 maps obtained from the GRE sequence, three different field probe position estimation methods were used: First, the assumption of linear gradients (*lin*). Second, position calculation with measured gradient nonlinearities (*nonlin*). And lastly, a combination of the nonlinear position estimation and the knowledge of the relative positions of the field probes acquired from the CT scan. This method was called constrained nonlinear estimation (*connonlin*).

In order to estimate the field probe positions incorporating nonlinear gradient behavior (*nonlin*), the gradients had to be measured first. Therefore, we performed measurements with a single field probe that was moved on a regular LEGO grid to have defined positions. This was done for 9 x 9 points in the x-z-plane and for 4 different heights along y. The spacing between measurement points was 32 x 30 x 32 mm in x, y and z, respectively. The obtained data was then used to model nonlinear gradient behavior ($\boldsymbol{G}(\boldsymbol{r})$) by decomposing the measured values into up to fourth order spherical harmonic functions:

$$\boldsymbol{G}(\boldsymbol{r}) = \sum_{l=0}^{N} \sum_{m=-l}^{l} k_l^m S_l^m(\boldsymbol{r}) \tag{6.1}$$

where k_l^m is the coefficient corresponding to the spherical harmonic function S_m, and where N is the maximum order of the decomposition; l is the degree; and m is the order. With this model $\boldsymbol{G}(\boldsymbol{r})$ we could find the optimal (close to actual) position by solving the least squares minimization problem:

$$\min_{\boldsymbol{r}} = ||\boldsymbol{f_{meas}} - \gamma \boldsymbol{G}(\boldsymbol{r})||^2 \tag{6.2}$$

with $\boldsymbol{f_{meas}}$ as the frequency measured by the field probes for each gradient and γ being the gyromagnetic ratio for protons. The minimization problem was solved using a Newton optimization algorithm with the field probe position calculated from assuming linear gradients (*lin*) as a starting point. For the constrained optimization (*connonlin*) where the positions of the field probes relative to each other are known and fixed one only has to calculate a rigid body motion of the field camera in respect to the scanner's isocenter. This motion is described by three translational and three rotational parameters $\tau = [x, y, z, \theta, \phi, \rho]$. This changes the minimization from 6.2 to:

$$\min_{\tau=[x,y,z,\theta,\phi,\rho]} = \sum_{p=1}^{N_p} ||\boldsymbol{f_{meas}} - \gamma \boldsymbol{G}(\boldsymbol{r}(\boldsymbol{\tau}))||^2. \tag{6.3}$$

To compare the three different methods against the results from the B_0 mapping sequence, the field camera was moved to eight different positions inside the scanner for each shim configuration. This yielded 96 points for each configuration (given 12 field probes and eight different positions). However, all sample points outside of a 100 mm radius from the isocenter were discarded to be consistent with the field of view (FOV) of the B_0 mapping. A current of 1 A was applied to each shim channel subsequently and there was a pause of at least 5 s before each field camera measurement to allow any eddy currents to settle. The field camera measurements were then evaluated using the *lin*, *nonlin* and *connonlin* methods, each yielding a different set of spherical harmonics coefficients. With these coefficients the field was reconstructed on a 200 x 200 x 200 mm^3 cube. The differences between these reconstructed fields and the B_0 maps were compared using the standard deviation (SD) and the Pearson correlation coefficient $\rho_{X,Y}$ which is a measure of the correlation between two signals ranging from negative correlation -1 to perfect correlation 1.

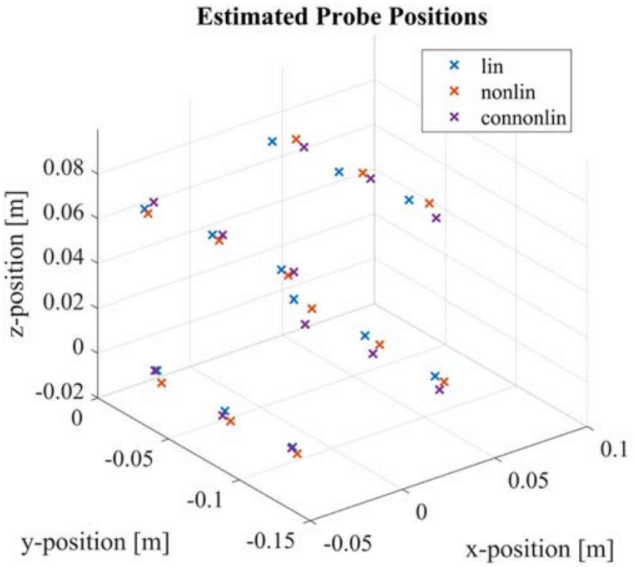

Figure 6.4: The positions of the field probes (for one position of the field camera) using each of the three position optimization methods.

Since the B_0 maps sampled the FOV with a lot more points than the camera, deviations between the two maps might not have exclusively stemmed from the assumption of false field probe positions but also from the smaller number of sampling points. Thus we also created a downsampled decomposition of the reference maps by only using the sampling points at the field probe positions derived from the *connonlin* method. This yielded the most accurate (in terms of deviation against the reference) field estimate that could theoretically be derived from the field camera measurements.

In addition, we performed simulations to investigate the influences of the three position estimation methods on the calculated fields. This was done assuming the field probe positions derived from the CT scan and subsequently calculating the measured frequency under gradients in x, y and z-direction using the fourth order nonlinear gradient model. These frequencies were used to derive position estimates for each field probe with each of the three models. The derived positions were used to decompose ideal theoretical shim fields with and without added Gaussian noise. The calculated coefficients of those shim fields were then used to reconstruct the field on a 100 x 100 x 100 m^3 cube. These fields could subsequently be compared again against the ideal theoretical shim fields.

A comparison of the position estimates for all three methods in one field camera position

is shown in Figure 6.4. The average deviation between the *connonlin* and *nonlin* method was 5.0 $\pm$ 1.4 mm with a maximum deviation of 7.0 mm. The deviation between the *connonlin* an *lin* method is even higher with an average of 8.8 $\pm$ 4.0 mm and a maximum of 14.5mm.

The validation of two models against the B_0 maps is shown in Figure 6.5. The displayed data shows the frequencies of the measured shim fields reconstructed from the B_0 maps and from the field probe data. In addition, the root-mean-squared error (RMSE) was calculated for the each measured and simulated shim field. The mean deviation per voxel was much better for most shim fields when using the *connonlin* method. The comparison with simulated values yielded similar results and when adding noise to the simulations, also the magnitude of the deviation was in a comparable range as the measured values.

The different comparisons show that the proposed field probe position estimation methods *nonlin* and *connonlin* can significantly improve the quality of the field measurements compared to the linear estimation which was previously used in literature. Thus, if no knowledge of the relative position of the field probes to each other is available, at least the gradient nonlinearities should be taken into account and corrected for to improve the quality of the calculated field estimates.

Contributions:

P. Chang devised the concept of optimising position calibration, built the field camera, conducted and evaluated the measurements and wrote the majority of the manuscript (including images) with help and advice from A. Henning. S. Nassirpour measured the shim fields for each shim coil of the shim insert and analysed the B_0 imaging data. K. Scheffler gave advice on the manuscript and on the field probes. I helped with building the field probes and conducted the single field probe measurements to derive the model for the nonlinear gradient behavior.

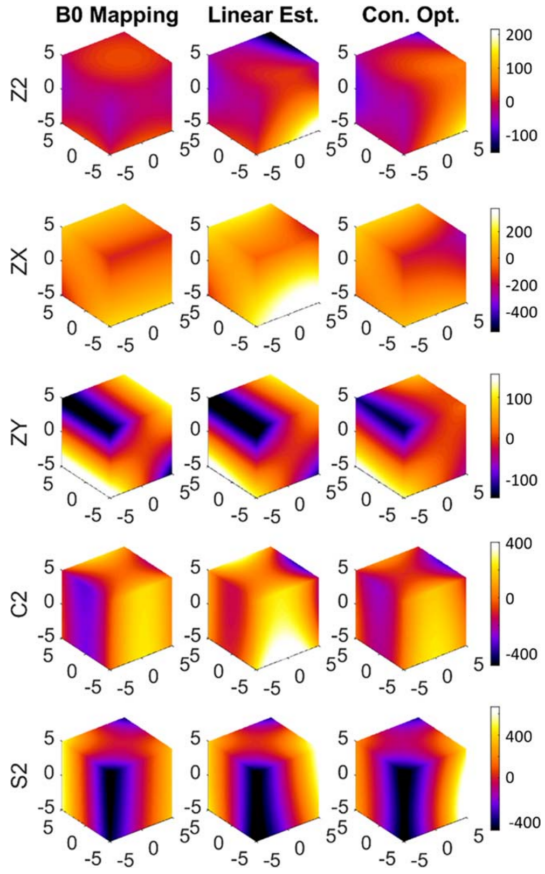

Figure 6.5: Shim fields for the second-order terms measured using B_0 mapping (original reference maps) and measured using the field camera (with linear estimation and constrained optimization for position calibration). The fields are shown in Hz (for 1.0 A).

6.3 PUBLICATION 3: COMPARISON OF PROSPECTIVE HEAD MOTION CORRECTION WITH NMR FIELD PROBES AND AN OPTICAL TRACKING SYSTEM

Applying the knowledge acquired by researching the previous two publications, this paper now shows the use of NMR field probes for prospective head motion correction in human subjects. The results are then compared against another motion correction method which is based on an optical camera. Here, we also made the transition to fluorine-based field probes since they ideally won't interfere with the imaging experiments because of the separation in the frequency domain (see e.g. [31], [32]).

A lot of different methods have been proposed to mitigate the effects of motion on MR images [14]. This includes retrospective methods which are applied after the image has been recorded, and prospective methods that try to continuously update position and orientation of the FOV during image acquisition. This paper compares the motion correction capabilities and limitations of two prospective motion correction modalities, ^{19}F NMR field probes [32] and an optical MPT camera-marker system [22] in human subjects.

Both systems, aside from their motion tracking performance, have their technical advantages and disadvantages. The optical tracking system has a fast sampling rate ($\sim$85 Hz) and is almost independent from the imaging sequence. However, it does require a direct line of sight from the camera to the marker and a cross-calibration from camera coordinates to the MR scanner's coordinate frame. NMR field probes on the other hand do not need a line of sight and they naturally operate in the scanner coordinate frame. Tracking those field probes, however, usually requires additional tracking gradients that have to be inserted into the sequence as has been done in this work. But it has recently been shown [33] that it is also possible to use native sequence gradients to localize the field probes.

The NMR field probes in this work used Hexafluorobenzene (C_6F_6) as NMR active sample. The receive electronics were the ones described in 6.1 and are shown in Figure 6.6a. The localization of the field probe was done with three bipolar gradients along each axis (see Figure 6.6b). Bipolar gradients were used so that B_0 fluctuations are canceled out when averaging over the positive and negative plateau. A linear regression was used to determine the phase change, $\dot{\phi}_{\pm(\boldsymbol{r})}$, of both plateaus which could be used to

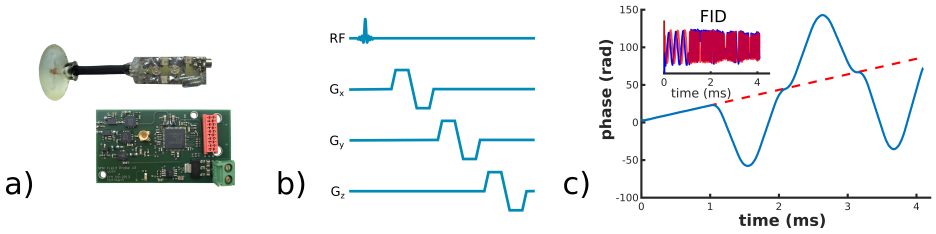

Figure 6.6: a) 19F NMR Field probe with tuning/matching-circuitry and PCB for signal processing. b) Bipolar gradients used for position tracking of the field probes. c) Corresponding measured phase and FID for one field probe when applying three orthogonal bipolar gradients.

calculate the gradient strength $\boldsymbol{g}(\boldsymbol{r})$ at the probe's position $\boldsymbol{r}$. One could now create the matrix $\boldsymbol{G}$ with the applied gradient strengths as diagonal entries. Under the assumption of linear gradients the position of one field probe could now be calculated as:

$$\boldsymbol{r} = \boldsymbol{G}^{-1}\boldsymbol{g}(\boldsymbol{r}). \tag{6.4}$$

Since we knew from our previous work that the assumption of linear gradients does not hold true, we had to correct our position estimation by using the nonlinear version of equation 6.4. This was done by adding a spatial dependency to our matrix of applied gradient strengths, thus it became $\boldsymbol{G}(\boldsymbol{r})$ and our equation changed to

$$\boldsymbol{g}(\boldsymbol{r}) = \boldsymbol{G}(\boldsymbol{r})\boldsymbol{r}. \tag{6.5}$$

Now, $\boldsymbol{r}$ could be determined by solving the minimization problem

$$\boldsymbol{r} = \arg\min_{\boldsymbol{r}}(\boldsymbol{G}(\boldsymbol{r})\boldsymbol{r} - \boldsymbol{g}(\boldsymbol{r})), \tag{6.6}$$

while choosing the result from the linear equation 6.4 as a starting value for $\boldsymbol{r}$. The calculation of the field probe positions and the corresponding motion was done in a custom LabVIEW program using an algorithm proposed by Umeyama [23]. The calculation for four field probes took approximately 70 ms.

The MPT system (Kineticor Inc, HI, USA) consisted of an optical camera that was mounted inside the scanner bore and tracked an MPT marker with a frame-rate of 85 Hz. A cross-calibration was needed to transform the camera-obtained data into the

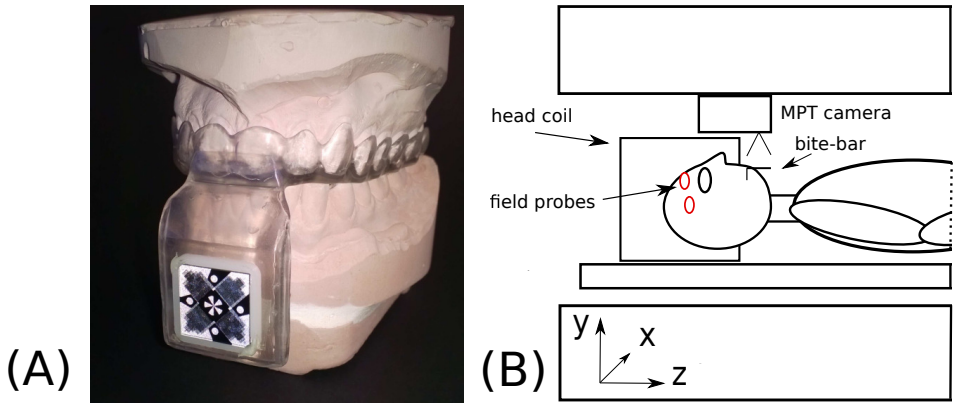

Figure 6.7: a) MPT marker on custom-made bite-bar. b) Positioning of the MPT tracking camera and the field probes in the scanner bore for a closed coil setup.

scanner coordinate frame. The cross-calibration could be obtained by acquiring MR images of a structured phantom in different positions while concurrently measuring its orientation with the camera as well [34].

All presented measurements were carried out on a 9.4 T human whole body MR scanner (Siemens Healthcare, Erlangen, Germany) equipped with a custom-built 16Tx/31Rx head coil [35].

We performed three measurements, one with a motion stage to compare tracking values of both system, and two measurements with subjects. The motion stage consisted of a sledge hosting a field probe and an MPT marker and an attached micrometer caliper to compare measurements from both systems against a ground truth. For the subject measurements, the field probes were attached to the subjects' temples and nose bridge with medical tape. The MPT marker was attached using a custom made bite-bar for each subject (Figure 6.7a). Four subjects were scanned with a 2D gradient echo (GRE) sequence while asked to perform different motion patterns. Two subjects were measured while asked to hold still and using an MP2RAGE sequence [36].

The measurements with the motion stage showed that in a distance of almost 20 cm from the isocenter, even the applied gradient nonlinearity correction could not entirely compensate the gradient effects. After a 3 cm motion the MPT measurements and field probe measurements differed by 750 μm.

For the 2D GRE sequence the subjects were asked to subsequently perform no motion, small motion, fast motion and big motion. Each motion condition was imaged once without prospective correction, with field probe correction and with MPT correction. For all measurements, whether the correction was switched on or not, the motion trajectories were recorded with both tracking modalities. Those trajectories were then used to additionally compare the tracking values of both systems against each other beyond the visual inspection of the prospectively corrected images. This comparison yielded a close correlation between the measured values of both systems with correlation coefficients above 0.9 for all six degrees of freedom other than the translation in y with a correlation coefficient of 0.61 which could partly be attributed to the low range of motion along that axis.

The prospectively corrected and uncorrected 2D GRE images for one subject are depicted in Figure 6.8. Both motion correction modalities are clearly able to improve image quality substantially under the presence of subject motion. Especially for the case of big motion however, the quality of the images is still a little decreased when compared to the images without voluntary motion.

The acquired MP2RAGE images for all three motion correction scenarios in one subject are shown in Figure 6.9. Motion correction visibly increases image quality in both scans when it was applied. However, the camera system outperforms the field probes when looking at small details as highlighted in the images.

However, there are still some methodological issues that are dependent on the motion correction method in general and there are other issues that are inherent only to our specific implementation of either method. One crucial point is the fixation of the marker and the field probes to the subjects. Here, the bite-bar provides a more rigid attachment compared to the medical tape used for the field probes. The setup could clearly be improved by a more rigid method of attachment, but this was difficult to implement due to the spatial constraints inside the tightly fitting receive helmet. The motion stage measurement as well as the previous publication showed that knowledge of nonlinear gradient behavior is also important for the position estimation of the field probes. The estimation could probably be improved further by including higher order corrections or conducting additional measurements of the nonlinearities. Furthermore, in our implementation, the processing time for the field probe signals is still rather high and might be further reduced by using faster software of dedicated hardware. The camera system

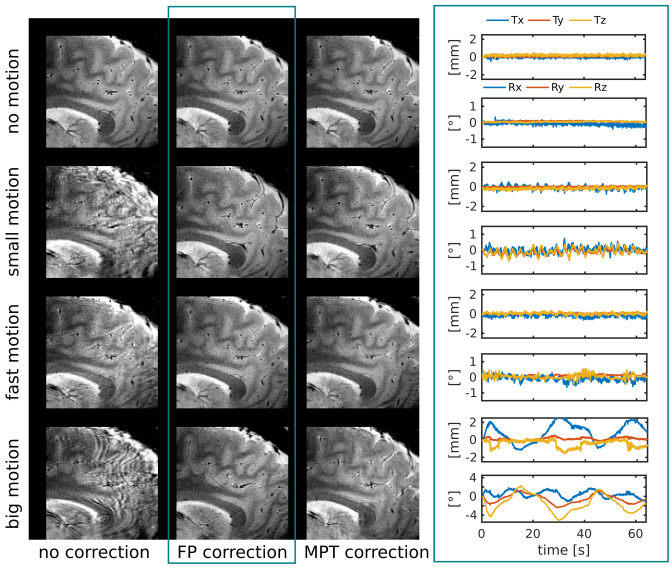

Figure 6.8: 2D Gradient echo images with an in-plane resolutioon of 0.5 mm x 0.5 mm and a through-plane resolution of 1.6 mm. Zoomed images for all twelve imaging conditions in one subject along with one field probe motion trajectory for each motion condition.

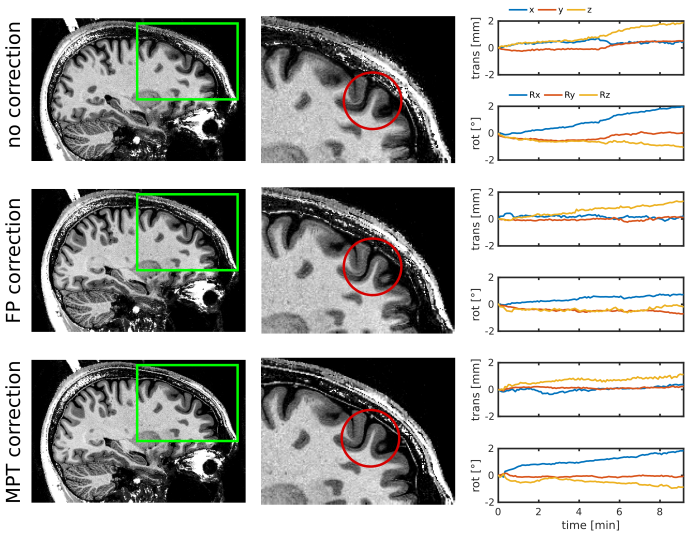

Figure 6.9: MP2RAGE images (0.5 mm3 isotropic, acquisition time 9:03 min) for three motion correction conditions with corresponding motion trajectories acquired with the camera.

on the other hand relies on the quality of the cross-calibration, which directly influences the calculated motion parameters.

Nevertheless, both motion correction methods were able to increase image quality substantially in both imaging scenarios. In addition, the measured values of both systems were highly correlated, which shows that the field probe system can perform at a similar level. However, the precision and latency are still below the values reached by the MPT system. But recent work has shown that field probes can in principle reach similar precision and a lower latency as well [33]. Thus, the choice of either tracking system comes down to the specific usage case while considering spatial constraints, line of sight, possible attachments of either system to the subjects and the desired sequences.

Contributions:

A. Aghaeifar wrote the motion correction library and programmed the GRE sequence. J. Bause programmed the MP2RAGE sequence, helped with the measurements and gave advice on the manuscript. J. Handwerker and J. Anders provided the transmit and

recieve electronics as well as parts of the software for the field probe measurements. E.-M. Engel provided the custom bite-bars for marker fixation. A. Thielscher advised on the measurements. K. Scheffler gave advice on the study design and on the manuscript. I built the field probes, implemented motion estimation into the software, conducted the measurements and wrote the manuscript.

7 CONCLUSION & OUTLOOK

We demonstrated the feasibility of prospective head motion correction using NMR field probes. With the use of dedicated microelectronic hardware it was possible to transition to a stand-alone setup that is independent of the MR scanner. Thus, the system can be used concurrently with the acquisition of MR images. The down-conversion of the field probe signal on the PCB inside the scanner bore makes the field probe measurements more robust against RF-interference from imaging experiments and also the other way around. Furthermore, we could improve field measurements and motion correction alike by employing a field probe position estimation that goes beyond the assumption of linear gradients. With the resulting increased accuracy of the motion estimates we could perform prospective head motion correction in different imaging scenarios and for different subjects. Motion artifacts in images that were subject to head motion could be reduced drastically compared to reference images without intentional head motion. The comparison to a commercially available optical motion tracking system showed a similar motion correction performance in terms of image quality even though the tracking precision was lower for the field probe based setup. The comparison of the concurrently measured motion tracking values of both systems showed a high correlation as well. For longer acquisition times, however, there seemed to be issues with the field probe fixation to the subjects' heads. This lead to a decrease in performance compared to optical motion tracking but image quality could still be improved when compared to the images acquired without any motion correction.

Nevertheless, the handling and cabling of the system is still quite cumbersome and further miniaturization of the electronics as well as a reduction of necessary cables would further increase usability and subject comfort. First steps in this direction have already been done with the development of an application specific integrated circuit (ASIC) based setup, which decreases the size of the electronic components and reduces the power

consumption as well as the amount of cables necessary. Also it might be possible to only use a single field probe to infer information about translational and rotational motion by evaluating the signal spectrum while the tracking gradients are applied. This would further mitigate the issues with attachment and cabling.

To conclude, there are still obstacles to overcome until prospective head motion correction can become a clinical standard. The requirements for a hypothetical clinically useful motion correction system include a reliable, rigid, fast and easy fixation of the marker(s) to the head, it should also be a system that does not produce erroneous motion information or at least reliably detects errors to prevent false motion updates. In addition, it should require minimal changes to the hardware and software (e.g. pulse sequences) of the MR system. Furthermore, the precision should be good enough for most clinical application scenarios. Ideally, all of this should be combined with a minimal monetary footprint.

The issue of marker fixation, however, can be circumvented by markerless motion tracking which uses one or several cameras to scan features of or on the face [21, 37]. Even though data processing in those approaches is more demanding which leads to an increased latency between motion detection and correction and the accuracy is not yet at the level of marker based optical tracking, both issues can be probably be tackled by better software and faster computing. This is why this is probably the most promising technology since it ensures ease of handling and does not require major changes to clinical procedures. So, if there is a demand for an implementation of head motion correction in clinical practice, we will probably see an increased use of those devices in the near future.

8 ACKNOWLEDGEMENTS

This work would not have been possible without the help and support from a lot of people. Therefore, I want to dedicate a few lines to express my gratitude.

First of all, I want to thank my supervisors Prof. Dr. Klaus Scheffler and Prof. Dr. Dr. Fritz Schick for giving me the opportunity to write this thesis, for their advice and their willingness to read through this amount of text.

I would also like to thank my collaborators and advisors from other institutes, Dr. Dr. Axel Thielscher from the Copenhagen University Hospital Hvidovre, Markus Kuehne from the TU Munich, Jonas Handwerker and Prof. Dr. Jens Anders, both from the Universities of Ulm and Stuttgart.

A big thank you is also due to Jonas Bause for the scientific support and the knowledge he provided as well as the mental support during all these years and in all of the coffee breaks.

Thanks also to my colleagues and former colleagues Ali, Chris, my former mentor Jens, Julia, Shajan, Alex, Mario, Dario, Paul, Sahar, Joana, Kai, Mihai, Philipp, Rolf, Tina, Juri, Johannes, Eric & Eric. I will also inevitably have forgotten to mention some people and I'm sorry!

Last, but by far not least, I want to thank my wife Anne who always supported me and believed in me through the past years. I also want to thank my sons, who were taking my sleep away at night, but made the days a lot more fun. I also want to thank my parents for supporting me even though they always had and have struggles of their own.

REFERENCES

[1] Christoph Barmet, Nicola De Zanche, Bertram J Wilm, and Klaas P Pruessmann. A transmit/receive system for magnetic field monitoring of in vivo MRI. *Magnetic Resonance in Medicine*, 62(1):269–76, jul 2009.

[2] Malcolm H. Levitt. *Spin Dynamics: Basics of Nuclear Magnetic Resonance*. Wiley, 2008.

[3] E. Mark Haacke, Robert W. Brown, Michael R. Thompson, and Ramesh Venkatesan. *Magnetic Resonance Imaging: Physical Principles and Sequence Design*. Wiley-Liss, 1999.

[4] Pierre-Marie Robitaille and Lawrence Berliner. *Ultra High Field Magnetic Resonance Imaging (Biological Magnetic Resonance)*. Springer, 2006.

[5] Martin Eschelbach. NMR Field Probes for Magnetic Resonance Tomography at 9.4 Tesla. Diploma thesis, University of Tuebingen, 2013.

[6] J.C. Tamraz, C. Outin, M. Forjaz Secca, and B. Soussi. *MRI Principles of the Head, Skull Base and Spine*. Springer, 2002.

[7] F. Bloch. Nuclear induction. *Phys. Rev.*, 70:460–474, Oct 1946.

[8] Matt A. Bernstein, Kevin F. King, and Xiaohong Joe Zhou. *Handbook of MRI Pulse Sequences*. Academic Press, 2004.

[9] Christoph Barmet and ND Zanche. Spatiotemporal magnetic field monitoring for MR. *Magnetic Resonance in Medicine*, 60(1):187–97, jul 2008.

[10] K.R. Minard and R.A. Wind. Solenoidal microcoil design. Part I: optimizing RF homogeneity and coil dimensions. *Concepts in Magnetic Resonance*, 13(2):128–142, 2001.

[11] Nicola De Zanche, Christoph Barmet, Jurek a Nordmeyer-Massner, and Klaas P Pruessmann. NMR probes for measuring magnetic fields and field dynamics in MR systems. *Magnetic Resonance in Medicine*, 60(1):176–86, jul 2008.

[12] Maxim Zaitsev, Julian Maclaren, and Michael Herbst. Motion artifacts in MRI: A complex problem with many partial solutions. *Journal of Magnetic Resonance Imaging*, 42(4):887–901, jan 2015.

[13] V. Menon, K. O. Lim, J. H. Anderson, J. Johnson, and A. Pfefferbaum. Design and efficacy of a head-coil bite bar for reducing movement-related artifacts during functional MRI scanning. *Behavior Research Methods, Instruments, & Computers*, 29(4):589–594, dec 1997.

[14] F Godenschweger, U Kägebein, D Stucht, U Yarach, A Sciarra, R Yakupov, F Lüsebrink, P Schulze, and O Speck. Motion correction in MRI of the brain. *Physics in Medicine and Biology*, 61(5):R32–R56, feb 2016.

[15] Alexander Loktyushin, Hannes Nickisch, Rolf Pohmann, and Bernhard Schölkopf. Blind retrospective motion correction of MR images. *Magnetic Resonance in Medicine*, 70(6):1608–1618, feb 2013.

[16] James G. Pipe. Motion correction with PROPELLER MRI: Application to head motion and free-breathing cardiac imaging. *Magnetic Resonance in Medicine*, 42(5):963–969, nov 1999.

[17] R L Ehman and J P Felmlee. Adaptive technique for high-definition MR imaging of moving structures. *Radiology*, 173(1):255–263, oct 1989.

[18] Tobias Kober, José P. Marques, Rolf Gruetter, and Gunnar Krueger. Head motion detection using FID navigators. *Magnetic Resonance in Medicine*, 66(1):135–143, feb 2011.

[19] Julian Maclaren, Brian S. R. Armstrong, Robert T. Barrows, K. A. Danishad,

Thomas Ernst, Colin L. Foster, Kazim Gumus, Michael Herbst, Ilja Y. Kadashevich, Todd P. Kusik, Qiaotian Li, Cris Lovell-Smith, Thomas Prieto, Peter Schulze, Oliver Speck, Daniel Stucht, and Maxim Zaitsev. Measurement and correction of microscopic head motion during magnetic resonance imaging of the brain. *PLoS ONE*, 7(11):e48088, nov 2012.

[20] M. Zaitsev, C. Dold, G. Sakas, J. Hennig, and O. Speck. Magnetic resonance imaging of freely moving objects: prospective real-time motion correction using an external optical motion tracking system. *NeuroImage*, 31(3):1038–1050, jul 2006.

[21] O. V. Olesen, R. R. Paulsen, L. Hojgaard, B. Roed, and R. Larsen. Motion tracking for medical imaging: A nonvisible structured light tracking approach. *IEEE Transactions on Medical Imaging*, 31(1):79–87, Jan 2012.

[22] Julian Maclaren, Michael Herbst, Oliver Speck, and Maxim Zaitsev. Prospective motion correction in brain imaging: A review. *Magnetic Resonance in Medicine*, 69(3):621–36, mar 2013.

[23] S. Umeyama. Least-squares estimation of transformation parameters between two point patterns. *IEEE Transactions on Pattern Analysis and Machine Intelligence*, 13(4):376–380, Apr 1991.

[24] Rachel W. Chan, Constantin von Deuster, Daniel Giese, Christian T. Stoeck, Jack Harmer, Andrew P. Aitken, David Atkinson, and Sebastian Kozerke. Characterization and correction of eddy-current artifacts in unipolar and bipolar diffusion sequences using magnetic field monitoring. *Journal of Magnetic Resonance*, 244:74–84, jul 2014.

[25] Daniel Hernandez, Ki Soo Kim, Eric Michel, and Soo Yeol Lee. Correction ofB0drift effects in magnetic resonance thermometry using magnetic field monitoring technique. *Concepts in Magnetic Resonance Part B: Magnetic Resonance Engineering*, 46B(2):81–89, apr 2016.

[26] Martin Eschelbach and Klaus Scheffler. NMR Field Probes for MRI at 9.4 T. In *16. Jahrestagung Deutschen Sektion der ISMRM e.V. (DS ISMRM 2013)*, pages 69–70, 2013.

[27] Boesch Ch., Gruetter R., and Martin E. Temporal and spatial analysis of fields generated by eddy currents in superconducting magnets: Optimization of corrections and quantitative characterization of magnet/gradient systems. *Magnetic Resonance in Medicine*, 20(2):268–284, 1991.

[28] Nikolaos G. Papadakis, Kay M. Martin, John D. Pickard, Laurance D. Hall, T. Adrian Carpenter, and Christopher L.-H. Huang. Gradient preemphasis calibration in diffusion-weighted echo-planar imaging. *Magnetic Resonance in Medicine*, 44(4):616–624, 2000.

[29] Ariane Fillmer, Signe Johanna Vannesjo, Matteo Pavan, Milan Scheidegger, Klaas Paul Pruessmann, and Anke Henning. Fast iterative pre-emphasis calibration method enabling third-order dynamic shim updated fMRI. *Magnetic Resonance in Medicine*, 75(3):1119–1131, may 2015.

[30] Vincent O Boer, Bart L van de Bank, Gerard van Vliet, Peter R Luijten, and Dennis W J Klomp. Direct B0 field monitoring and real-time B0 field updating in the human breast at 7 Tesla. *Magnetic Resonance in Medicine*, 67(2):586–91, feb 2012.

[31] Pekka Sipilä, Sebastian Greding, Gerhard Wachutka, and Florian Wiesinger. 2H transmit-receive NMR probes for magnetic field monitoring in MRI. *Magnetic Resonance in Medicine*, 65(5):1498–506, may 2011.

[32] Maximilian Haeberlin, Lars Kasper, Christoph Barmet, David O Brunner, Benjamin E Dietrich, Simon Gross, Bertram J Wilm, Sebastian Kozerke, and Klaas P Pruessmann. Real-time motion correction using gradient tones and head-mounted NMR field probes. *Magnetic Resonance in Medicine*, 00, sep 2014.

[33] Alexander Aranovitch, Maximilian Haeberlin, Simon Gross, Benjamin E. Dietrich, Bertram J. Wilm, David O. Brunner, Thomas Schmid, Roger Luechinger, and Klaas P. Pruessmann. Prospective motion correction with NMR markers using only native sequence elements. *Magnetic Resonance in Medicine*, 79(4):2046–2056, aug 2017.

[34] Benjamin Zahneisen, Chris Lovell-Smith, Michael Herbst, Maxim Zaitsev, Oliver Speck, Brian Armstrong, and Thomas Ernst. Fast noniterative calibration of an

external motion tracking device. *Magnetic Resonance in Medicine*, 71(4):1489–1500, jun 2013.

[35] G. Shajan, Mikhail Kozlov, Jens Hoffmann, Robert Turner, Klaus Scheffler, and Rolf Pohmann. A 16-channel dual-row transmit array in combination with a 31-element receive array for human brain imaging at 9.4 t. *Magnetic Resonance in Medicine*, 71(2):870–879, mar 2013.

[36] José P. Marques, Tobias Kober, Gunnar Krueger, Wietske van der Zwaag, Pierre-François Van de Moortele, and Rolf Gruetter. MP2rage, a self bias-field corrected sequence for improved segmentation and t1-mapping at high field. *NeuroImage*, 49(2):1271–1281, jan 2010.

[37] Julian Maclaren, Andre Kyme, Murat Aksoy, Benjamin Zahneisen, and Roland Bammer. Markerless Optical Tracking for Motion Correction in MR and PET/MR Imaging of the Brain. In *Proc. Intl. Soc. Mag. Reson. Med. 25*, page 1292, Honolulu, USA, 2017.

PUBLICATION LIST

Journal Articles

[A] P. Chang, S. Nassirpour, M. Eschelbach, K. Scheffler, and A. Henning. Constrained optimization for position calibration of an NMR field camera. *Magnetic Resonance in Medicine*, 80(1):380–390, 2017.

[B] M. Kuehne, M. Eschelbach, A. Aghaeifar, L. von Pflugk, A. Thielscher, M. Himmelbach, K. Scheffler, P. S. van der, and A. Peer. An MR-compatible haptic interface with seven degrees of freedom. *IEEE/ASME Transactions on Mechatronics*, 23(2):624–635, 2018.

[C] M. Eschelbach, A. Aghaeifar, J. Bause, J. Handwerker, J. Anders, E.-M. Engel, A. Thielscher, and K. Scheffler. Comparison of prospective head motion correction with NMR field probes and an optical tracking system. *Magnetic Resonance in Medicine*, 2018.

Conference Papers

[D] J. Handwerker, M. Eschelbach, P. Chang, A. Henning, K. Scheffler, M. Ortmanns, and J. Anders. An active TX/RX NMR probe for real-time monitoring of MRI field imperfections. In *2013 IEEE Biomedical Circuits and Systems Conference (BioCAS)*. IEEE, 2013.

[E] M. Eschelbach and K. Scheffler. NMR Field Probes for MRI at 9.4 T. In *16.*

Jahrestagung Deutschen Sektion der ISMRM e.V. (DS ISMRM 2013), Freiburg, Germany, 2013.

Contributions to Conferences and Workshops

[F] J. Handwerker, V. Bonehi, M. Eschelbach, K. Scheffler, M. Ortmanns, and J. Anders. An active transmit/receive NMR magnetometer for field monitoring in ultra high field MRI scanners. In *Dreiländertagung der Deutschen, Schweizerischen und Österreichischen Gesellschaft für Biomedizinische Technik (BMT 2013), Graz, Austria, Biomedical Engineering / Biomedizinische Technik, 58(Supplement 1)*. Walter de Gruyter GmbH, 2013.

[G] P. Chang, M. Eschelbach, N. Avdietvitch, K. Scheffler, and A. Henning. Fast Method for Parametric System Identification of Gradient Systems. In *Joint Annual Meeting ISMRM-ESMRMB, Milano, Italy*, 2014.

[H] P. Chang, M. Eschelbach, K. Scheffler, and A. Henning. Hybrid Digital Phase-Locked Loop and Moving Average Filtering Improves SNR in Spatio-Temporal Field Monitoring. In *Joint Annual Meeting ISMRM-ESMRMB, Milano, Italy*, 2014.

[I] J. Handwerker, A. Hoffmann, M. Eschelbach, K. Scheffler, M. Ortmanns, and J. Anders. A distributed active NMR sensor array for artifact correction in ultra high field MRI applications. In *48th Annual Conference of the German Society for Biomedical Engineering (BMT 2014), Hannover, Germany, Biomedical Engineering / Biomedizinische Technik, 59(Supplement 1)*, volume 59. Walter de Gruyter GmbH, 2014.

[J] M. Eschelbach, P. Chang, J. Handwerker, J. Anders, A. Henning, and K. Scheffler. Tracking Motion and Resulting Field Fluctuations Using 19F NMR Field Probes. In *Proceedings of the 23rd annual meeting of the ISMRM, Toronto*, page 266, 2015.

[K] M. Kuehne, M. Ergin, S. Klare, M. Eschelbach, A. Aghaeifar, A. Thielscher, and A. Peer. Towards an MR-compatible Haptic Interface with Seven Actuated Degrees of Freedom. In *IEEE International Conference on Robotics and Automation (ICRA 2015)*, Seattle, WA, USA, 2015.

[L] R. Pohmann, J. Bause, C. Mirkes, M. Eschelbach, E.-M. Engel, and K. Scheffler. Ultrahigh resolution anatomical brain imaging at 9.4 T using prospective motion correction. In *ESMRMB 2015, 32nd Annual Scientific Meeting, Edinburgh, UK*, volume 28, page 155. Springer Nature, 2015.

[M] P. Chang, M. Eschelbach, R. Syha, K. Scheffler, and A. Henning. Impact of Gradient Nonlinearity on the Accuracy of NMR Field Camera Readouts. In *23rd Annual Meeting and Exhibition of the ISMRM, Toronto, Canada*, 2015.

[N] J. Handwerker, M. Eschelbach, A. Hoffmann, M. Ortmanns, K. Scheffler, and J. Anders. An Array of Active TX/RX 19F NMR Field Probes for Gradient Trajectory Mapping. In *European Congress on Magnetic Resonance (EUROMAR 2015)*, 2015.

[O] M. Eschelbach, A. Loktyushin, P. Chang, J. Handwerker, J. Anders, A. Henning, A. Thielscher, and K. Scheffler. A Comparison of 19F NMR Field Probes and an Optical Camera System for Motion Tracking. In *Proceedings of the 24th annual meeting of the ISMRM, Singapore*, page 0340, 2016.

[P] A. Aghaeifar, M. Eschelbach, and K. Scheffler. Real time communications over UDP protocol. In *European IDEA Users Group Meeting 2016, Maastricht, The Netherlands*, 2016.

[Q] A. Aghaeifar, M. Eschelbach, J. Bause, A. Thielscher, and K. Scheffler. AMoCo, a software package for prospective motion correction. In *Proceedings of ISMRM annual meeting Honolulu, HI, USA*, page 0305, 2017.

[R] M. Eschelbach, A. Aghaeifar, J. Bause, J. Handwerker, J. Anders, A. Thielscher, and K. Scheffler. A Comparison of Prospective Motion Correction with 19F NMR Field Probes and an Optical Camera. In *Proceedings of the 25th annual meeting of the ISMRM, Honolulu*, page 1304, 2017.

[S] A. Aghaeifar, M. Eschelbach, and K. Scheffler. Multi-Modality Prospective Motion Correction of Human Head. In *ISMRM Workshop on Motion Correction in MRI & MRS (MoCor 2017), Cape Town, South Africa*, 2017.

[T] A. Aghaeifar, A. Loktyushin, M. Eschelbach, and K. Scheffler. Improving performance of linear field generation with multi-coil setup by optimizing coils position.

In *34th Annual Scientific Meeting of the European Society for Magnetic Resonance in Medicine and Biology (ESMRMB 2017), Barcelona, Spain*, 2017.

[U] J. Bause, A. Aghaeifar, M.-H. In, E.-M. Engel, P. Ehses, M. Eschelbach, K. Scheffler, and R. Pohmann. Distortion and prospective motion corrected zoomed functional imaging of the human brain at 9.4 Tesla. In *ESMRMB 2017, 34th Annual Scientific Meeting, Barcelona, ES*, volume 30, pages 125–126. Springer Nature, 2017.

[V] M. Eschelbach, A. Aghaeifar, E.-M. Engel, and K. Scheffler. Prospective Head Motion Correction Using Multiple Tracking Modalities. In *34th Annual Scientific Meeting of the European Society for Magnetic Resonance in Medicine and Biology (ESMRMB 2017), Barcelona, Spain*, 2017.

APPENDED PUBLICATIONS

The following publications have been reprinted with the permission of *IEEE* and *John Wiley & Sons, Inc.*.

PUBLICATION 1

An Active TX/RX NMR Probe for Real-Time Monitoring of MRI Field Imperfections

Jonas Handwerker, Maurits Ortmanns and Jens Anders
Institute of Microelectronics
University of Ulm
D-89081 Ulm, Germany
Email: jonas.handwerker@uni-ulm.de

Martin Eschelbach, Paul Chang, Anke Henning and Klaus Scheffler
High-Field MR Center
Max Planck Institute for Biological Cybernetics
D-72076 Tübingen, Germany

***Abstract*—In this paper, we present a PCB-based active miniaturized MR field probe for real-time monitoring of the magnetization's phase evolution during magnetic resonance (MR) experiments. The data obtained with the presented sensor can be used to correct gradient field imperfections which uncorrected result in significant distortions in the reconstructed MR images. The presented active field probe consists of a susceptibility matched solenoidal MR coil and a complete homodyne transceiver. Thanks to the local generation of the radio frequency signal required for the excitation of the spin ensemble and the downconversion of the recorded MR signal to low frequencies, the proposed architecture significantly reduces the crosstalk between the probe head and the MR imaging object compared to existing designs. MR measurements performed in an ultra high field 9.4 T full-body scanner prove the compatibility of the presented sensor with commercial MR imaging systems and demonstrate its excellent MR phase tracking performance.**

I. Introduction

Most in-vivo magnetic resonance (MR) experiments utilize magnetic gradient fields, which vary both in time and space, for signal encoding. Consequently, the correct interpretation of recorded MR data requires a precise knowledge of the spatiotemporal evolution of these gradient fields throughout the entire experiment, placing stringent requirements on the gradient producing hardware. Residual hardware induced artifacts can sometimes be corrected by sequence modification [1], but this method is not generally applicable. One universally applicable method consists of the direct measurement of the hardware induced artifacts in order to allow for either an a priori correction of the gradient evolution [2], [3] or a software based a posteriori correction of the MR images [4], [5].

Despite the aforementioned advances in MR artifact reduction residual imperfections in the magnetic fields such as finite gradient rise and fall times, long term drifts and patient induced nonrecurring field fluctuations (e.g. due to patient breathing or movement) still present one of the major obstacles in high field MRI applications with B_0-field strengths above 7 T which prevents MR image quality to fully benefit from the significantly enhanced signal-to-noise ratios (SNRs) associated with these elevated field strengths [6]. In order to be able to better correct these time-dependent, hard-to-be-predicted fluctuations, Barmet et al. [7] have suggested to monitor the real-time evolution of the magnetic field during the actual MR experiment and to use these real-time data for an a posteriori image correction. NMR probes provide both, a high field resolution in the sub-ppm range as well as high bandwidths up to several MHz and thus are a superior choice for field monitoring over other sensing principles [8].

The approach proposed in [7] utilizes miniaturized coils as local MR field probes in order to record the temporal evolution of the phase of the MR signal at different positions inside or closely around the field-of-view, to use these data for the construction of a time-dependent field map which can then be used for a correction of the distorted images. In the first generation of localized field probes, the miniaturized coils were operated in a receive-only mode, requiring an external excitation to produce an MR signal. Consequently, they displayed a considerable crosstalk between the field probe and the imaging object. To mitigate this undesirable coupling, field probes operating the microcoils in transmit-receive (TX/RX) mode were then presented in [9], which allowed for a significantly closer placement between field sensor and imaging object while keeping the coupling at a tolerable level. Boer et al. [10] successfully corrected for patient breathing motion using a receive-only field probe.

In this paper, we present a PCB-based active miniaturized MR probe head which combines a susceptibility matched solenoidal MR coil with a complete homodyne transceiver. Thanks to the local generation of the required RF-signal by means of an on-board PLL, the presented design removes the need for the transmission of high-frequency signals at or near the Larmor frequency through the MR scanner required in the existing designs, which can lead to significant distortion of the magnetization inside the MR imaging object. For a given tolerable amount of crosstalk between sensor and imaging object, the presented field probe can be placed closer to the imaging object and therefore in principle allows for a more precise field mapping compared to existing designs.

The paper is organized as follows: In section II, we present a brief review of the theoretical aspects of the proposed MR phase monitoring application. Section III then provides a description of the proposed active MR field probe and the experimental setup used for the MR experiments in a commercial MR scanner. In section IV, we present experimental MR data demonstrating the excellent performance of the proposed sensor, before we conclude the paper in section V.

978-1-4799-1471-5/13/$31.00

II. Theory of Operation

According to [7], the magnitude of the total magnetic field inside an MR scanner can be approximated by:

$$|\mathbf{B}(\mathbf{r},t)| = \sum_{l=0}^{N_L-1} c_l(t) \cdot f_l(\mathbf{r}) + B_{\text{ref}}(\mathbf{r}), \quad (1)$$

where the time-dependent coefficients $c_l(t)$ capture the dynamic part of the field evolution, the spatial basis functions $f_l(\mathbf{r})$ capture the position-dependency of the magnetic field and $B_{\text{ref}}(\mathbf{r}) = |\mathbf{B}(\mathbf{r},t)|$ denotes the magnitude of the magnetic field in some initial reference state. Since $B_{\text{ref}}(\mathbf{r})$ captures all static field components, in principal, only a small number of spatial basis functions is needed to expand the remaining smooth field components with dynamic coefficients $c_l(t)$ [7].

When exposed to a magnetic field described by (1), a spin ensemble with gyromagnetic ratio γ has a phase given by:

$$\phi(\mathbf{r},t) = \sum_{l=0}^{N_L-1} k_l(t) \cdot f_l(\mathbf{r}) + \omega_{\text{ref}}(\mathbf{r}), \quad (2)$$

where $\omega_{\text{ref}} = \gamma B_{\text{ref}}$ denotes the Larmor frequency in the reference state at position $\mathbf{r}$ and the phase coefficients $k_l(t)$ can be obtained from the time-dependent coefficients $c_l(t)$ by integration according to $k_l(t) = \gamma \int_0^t c_l(\tau)\,\mathrm{d}\tau$. The goal of real-time MR field monitoring is to extract the phase evolution of the imaging object's magnetization from measurements of the sample magnetization inside a distributed array of field probes, whose positions sample the basis functions $f_l(\mathbf{r})$ [7].

From the sensing principle, one can directly infer that in principle it is advantageous to be able to place the MR field probes as close to the imaging object as possible in order to reduce the required number of basis functions in (1), i.e. the number of required sensor nodes.

III. Design of the Active NMR Magnetometer

Fig. 1a illustrates the architecture of the presented MR probe head, which consists of the tuned and matched MR detection coil followed by the PCB-based homodyne transceiver. Fig. 1b shows a photograph of the corresponding PCB realization.

The required bandwidth of the homodyne transceiver can be derived from the desired field of view (FOV) $2x_{\text{max}} = 0.4\,\text{m}$ and the maximum gradient strength $G_{\text{max}} = 60\,\text{mT/m}$ according to $\Delta\nu_{\text{max}} = \gamma_{^1\text{H}}/(2\pi) x_{\text{max}} G_{\text{max}} \approx 500\,\text{kHz}$.

A. Field Probe

The MR detection coil shown as part of Fig. 1b is based on the design presented in [9]. A glass capillary (inner diameter 800 µm, outer diameter 1000 µm) is used as sample container for a liquid NMR sample. Enameled copper wire with a copper diameter of 200 µm is tightly wrapped around the capillary to form a 6-turn solenoidal TX/RX MR coil. Due to the B_1-sensitivity profile of the coil, the active sample volume is less than 1 µL. The size of the sample is a trade-off between SNR and resolution, since the maximum sample diameter is limited to twice the desired resolution [8]. To minimize susceptibility-induced line broadening, sample and coil are surrounded by

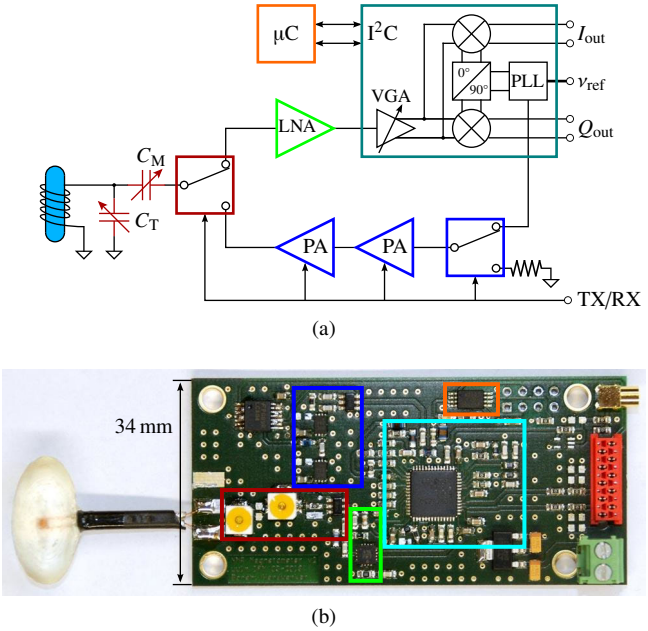

Fig. 1. (a) Block diagram of the NMR magnetometer and (b) photograph of the transceiver PCB with the attached field probe. In the block diagram and the photograph, corresponding blocks are highlighted with the same color.

a susceptibility-matching epoxy with an ellipsoidal shape. The MR field probe is connected to the transceiver on the PCB by means of a shielded transmission line to reduce field inhomogeneities induced by the PCB material and the electronic components. As MR sample inside the field probe, we use copper sulfate ($CuSO_4$) doped water. Here, doping the water allows to significantly lower the long T_1 time of pure water ($T_{1,\text{H}_2\text{O}} \approx 2\,\text{s}$ at 9.4 T) to enable high repetition rates while maintaining a relatively long T_2.

B. RF Transceiver

The field probe is tuned to the resonance frequency $\nu_0 = B_0 \gamma_{^1\text{H}}/(2\pi) = 399.72\,\text{MHz}$ and matched to the 50 Ω input impedance of the following stage by means of two MR compatible trimmer capacitors (Johanson Manufacturing Corporation, Boonton, NJ, USA) followed by a TX/RX-RF switch (HMC545, Hittite Microwave, Chelmsford, MA, USA) to alter between excitation of the MR sample and detection of the resulting MR signal.

In receive mode, the detected MR signal is first amplified by a low noise amplifier (LNA) (HMC616, Hittite Microwave, Chelmsford, MA, USA). The core component of the transceiver electronics is an integrated RF receiver (ADRF6850, Analog Devices, Cambridge, MA, USA) containing a variable gain amplifier (VGA), a quadrature demodulator and a phase-locked loop (PLL) for frequency synthesis. The PLL generates the local oscillator signal ν_{LO} from an externally supplied frequency reference at $\nu_{\text{ref}} = 9.993\,\text{MHz}$. This LO frequency is used for both excitation of the MR sample and donwnconversion of the resulting MR signal. The quadrature downconversion improves the achievable SNR by 3 dB and allows for homodyne detection thus reducing the required

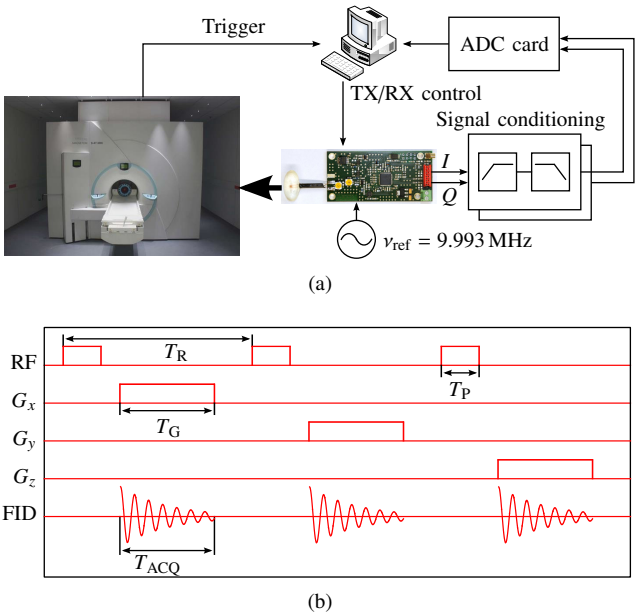

Fig. 2. Illustration of the (a) experimental setup for the NMR-based characterization and (b) acquisition sequence for the determination of the position of the field probe.

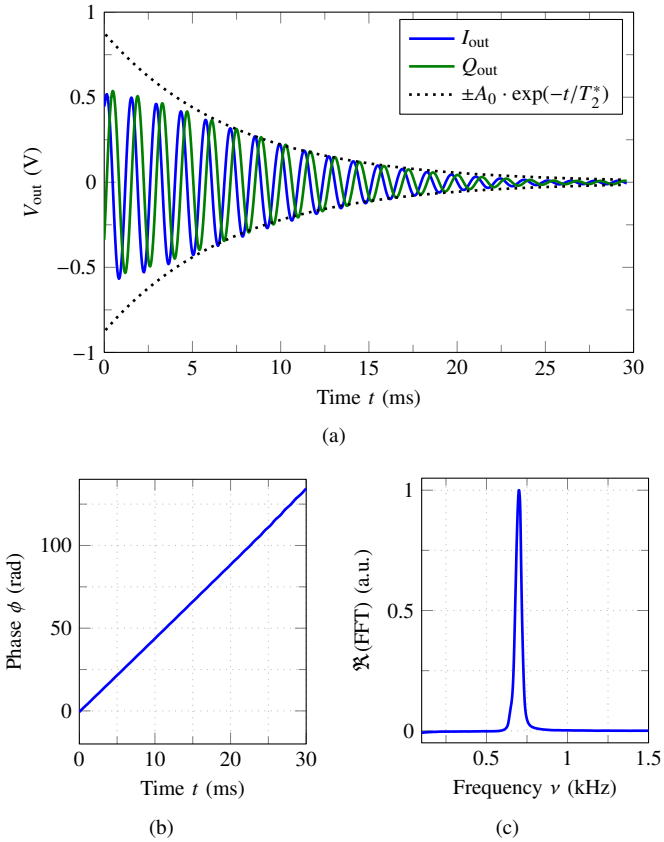

Fig. 3. (a) Time-domain FID of the field probe containing $CuSO_4$ doped water located in the scanner isocenter and fit of the envelope signal (inset: close-up view of the IQ signals; T_{ACQ} = 1 s, F_S = 1 MHz; measured T_2^* = 7.4 ms). (b) Corresponding unwrapped phase of the complex signal and (c) real part of the FFT showing the resonance frequency peak $\hat{\nu}_0$ = 708 Hz with ν_{FWHM} = 43 Hz

baseband bandwidth by a factor of two. During transmit, the TX switch directs the LO signal from the PLL to two cascaded power amplifiers (PAs) (MAX2616, Maxim Integrated, San Jose, CA, USA). The two PAs are disabled during receive mode by their built-in shutdown functionality in order to save power and reduce leakage into the detection signal. The PLL output power is programmable, in all experiments a TX power of 15.5 dBm was used as a compromise between pulse length and distortion. A microcontroller (µC) (ATtiny45, Atmel Corporation, San Jose, CA, USA) is used to program the registers of the receiver on each power-up.

C. Experimental Setup

The experimental setup used to perform the MR based characterization of the presented MR field probe is shown in Fig. 2a. The MR field probe is placed inside the B_0-field of the 9.4 T MR scanner (Magnetom 9.4 T, Siemens Healthcare, Erlangen, Germany) to polarize the spin ensemble, the reference signal ν_{ref} for the PLL-based synthesizer is supplied by an external signal generator. The quadrature outputs of the MR field probe PCB are connected to custom PCB-based anti-aliasing filters outside the scanner by means of a miniaturized twisted pair flatband cable, which minimizes inductive pickup. The anti-aliasing filters (AAFs) are not placed on the field probe PCB since their placement outside the magnet significantly improves the form factor of the resulting sensor PCB as well as the system performance because the AAFs can effectively filter RF signals induced into the cable from the scanner. The outputs of the AAFs are digitized by a commercial ADC (NI PCIe-6363, National Instruments, Austin, TX, USA). MR signal excitation and data acquisition are orchestrated by a custom LabVIEW program. Synchronization between this LabVIEW program and the scanner unit is achieved by an external TTL trigger signal generated by the scanner unit.

Fig. 2b shows the MR sequence used to determine the position of the field probe in the scanner. In the sequence, a 90°-RF pulse is followed by a static readout gradient (G_x, G_y or G_z) to acquire the sensor position along the spatial axes. For a reliable measurement, a reference signal without applied gradients is required and the sensor must be located within the linear range of the gradient system.

IV. Measurements

Using the setup described in the previous section, we performed several MR experiments to investigate the performance of the presented probe head. Fig. 3 shows the time-domain free induction decay (FID) after a 90°-excitation together with the corresponding unwrapped phase plot and real part of the FFT. In the FID, one clearly sees the effect of radiation damping due to the relatively large currents induced in the MR coil. The unwrapped phase plot in Fig. 3b shows no plateaus and thus can be used to extract the local Larmor frequency by linear regression. The full width at half maximum value in Fig. 3c without shimming compares to a measurement with a passive field probe, indicating that the nearby PCB and electronic components induce no additional line broadening. By optimizing the susceptibility-matching of the field probe,

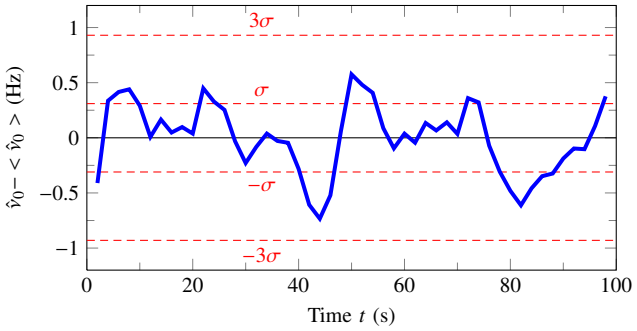

Fig. 4. Resonance frequency spread $\Delta\hat{\nu}_0 = \hat{\nu}_0 - < \hat{\nu}_0 >$ in a series of 49 measurements with a z-gradient $G_z = 2\,\mathrm{mT/m}$, $T_\mathrm{R} = 1\,\mathrm{s}$, $T_\mathrm{ACQ} = 32\,\mathrm{ms}$, $F_\mathrm{S} = 1\,\mathrm{MHz}$ resulting a frequency resolution $R_{\hat{\nu}_0} = 3\sigma = 0.93\,\mathrm{Hz}$

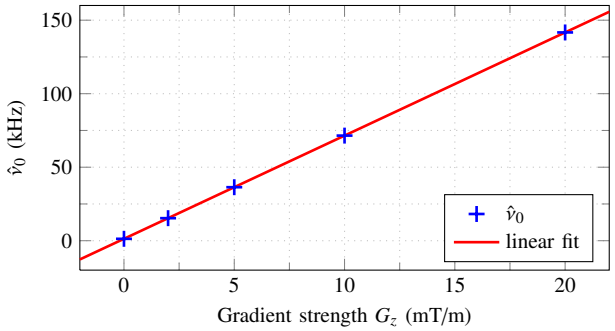

Fig. 5. Measurement and linear regression of the resonance frequency $\hat{\nu}_0$ for different gradient strengths G_z ($T_\mathrm{R} = 1\,\mathrm{s}$, $T_\mathrm{ACQ} = 32\,\mathrm{ms}$, $F_\mathrm{S} = 1\,\mathrm{MHz}$, 25 samples per point).

the linewidth could be further reduced, allowing for longer phase measurements.

Fig. 4 shows the calculated local Larmor frequency spread for 49 repetitions of a simple pulse acquire experiment, i.e. a 90°-RF pulse (the measured 90° pulse length is around $25\,\mu\mathrm{s}$) followed by acquisition of the FID, in the presence of a frequency encoding gradient with a strength of $G_z = 2\,\mathrm{mT/m}$ as a measure for the frequency stability of the presented MR field probe. Defining the frequency resolution as three times the standard deviation of the measured frequency spread, we obtain a value of $R_{\hat{\nu}_0} = 3\,\sigma = 0.93\,\mathrm{Hz}$ which corresponds to a magnetic field resolution of $R_{B_0} = 2\pi R_{\hat{\nu}_0}/\gamma_{^1\mathrm{H}} = 22\,\mathrm{nT}$ and a relative resolution of $R_{B_0}/B_0 = 2\,\mathrm{ppb}$.

Fig. 5 and Table I present the measured local Larmor frequency and corresponding frequency spread as a function of gradient strength. According to Fig. 5, the measured Larmor frequency displays the ideal linear change with applied gradient strength which is required for a precise initial positioning of the sensor inside the scanner unit. Table I illustrates the degradation of the measured frequency spread with increasing field strength due to gradient induced line broadening ($\sigma_{\hat{\nu}_0} \propto \sqrt{G_z}$, the value for $G_z = 2\,\mathrm{mT/m}$ is an outlier).

TABLE I
RESONANCE FREQUENCIES AND FREQUENCY SPREAD FROM FIG. 5.

G_z (mT/m)	0	2	5	10	20
$\hat{\nu}_0$ (kHz)	1.297	15.336	36.395	71.492	141.67
$\sigma_{\hat{\nu}_0}$ (Hz)	0.199	0.315	0.284	0.395	0.550

V. Conclusion and Outlook

In this paper, we presented an active PCB-based MR field probe for real-time monitoring of magnetic field imperfections for the correction of distorted MR images. MR experiments carried out in a 9.4 T full-body magnet at the Max Planck Institute in Tübingen both verify the excellent performance of the presented sensor with a relative resolution of 2 ppb which is comparable to the state-of-the-art given in [9], [10] and the feasibility of the proposed interface between the sensor and a commercial MR scanner unit. The main advantage of the proposed system compared to existing solutions lies in the local generation of the required RF signal and downconversion of the recorded MR signal removing the need for RF connections through the scanner which so far present a source for undesirable coupling with the imaging object's magnetization. This allows for a closer placement between sensor and imaging object which reduces the number of required sensor nodes to obtain a complete field map. As our next steps, we will further reduce the EM coupling between MR coil and field probe by changing the NMR sample from ^{1}H to ^{19}F, manufacture a first sensor array in order to perform true field mapping and use the resulting field maps for an a posteriori image correction of real MRI data.

References

[1] G. Wider, V. Dotsch, and K. Wuthrich, "Self-compensating pulsed magnetic-field gradients for short recovery times," *J. Magn. Reson Series A*, vol. 108, no. 2, pp. 255–258, 1994.

[2] M. A. Morich, D. A. Lampman, W. R. Dannels, and F. T. D. Goldie, "Exact temporal eddy-current compensation in magnetic-resonance imaging-systems," *IEEE Trans. Med. Imag.*, vol. 7, no. 3, pp. 247–254, 1988.

[3] C. Boesch, R. Gruetter, and E. Martin, "Temporal and spatial-analysis of fields generated by eddy currents in superconducting magnets - optimization of corrections and quantitative characterization of magnet gradient systems," *Magnet. Reson. Med.*, vol. 20, no. 2, pp. 268–284, 1991.

[4] R. J. Ordidge and I. D. Cresshull, "The correction of transient B0 field shifts following the application of pulsed gradients by phase correction in the time domain," *J. Magn. Reson*, vol. 69, no. 1, pp. 151–155, 1986.

[5] G. F. Mason, T. Harshbarger, H. P. Hetherington, Y. Zhang, G. M. Pohost, and D. B. Twieg, "A method to measure arbitrary k-space trajectories for rapid mr imaging," *Magnet. Reson. Med.*, vol. 38, no. 3, pp. 492–496, 1997.

[6] D. I. Hoult and R. E. Richards, "Signal-to-noise ratio of nuclear magnetic-resonance experiment," *J. Magn. Reson*, vol. 24, no. 1, pp. 71–85, 1976.

[7] C. Barmet, N. De Zanche, and K. P. Pruessmann, "Spatiotemporal magnetic field monitoring for mr," *Magnet. Reson. Med.*, vol. 60, no. 1, pp. 187–197, 2008.

[8] N. De Zanche, C. Barmet, J. A. Nordmeyer-Massner, and K. P. Pruessmann, "NMR probes for measuring magnetic fields and field dynamics in MR systems," *Magnet. Reson. Med.*, vol. 60, no. 1, pp. 176–186, 2008.

[9] C. Barmet, N. De Zanche, B. J. Wilm, and K. P. Pruessmann, "A transmit/receive system for magnetic field monitoring of in vivo MRI," *Magnet. Reson. Med.*, vol. 62, no. 1, pp. 269–276, 2009.

[10] V. O. Boer, B. L. vd Bank, G. van Vliet, P. R. Luijten, and D. W. J. Klomp, "Direct B0 field monitoring and real-time B0 field updating in the human breast at 7 tesla," *Magn. Reson. Med.*, vol. 67, no. 2, pp. 586–591, 2012.

PUBLICATION 2

Constrained Optimization for Position Calibration of an NMR Field Camera

Paul Chang,[1,2]* Sahar Nassirpour,[1,2] Martin Eschelbach,[1,3] Klaus Scheffler,[1,4] and Anke Henning[1,5]

Purpose: Knowledge of the positions of field probes in an NMR field camera is necessary for monitoring the B_0 field. The typical method of estimating these positions is by switching the gradients with known strengths and calculating the positions using the phases of the FIDs. We investigated improving the accuracy of estimating the probe positions and analyzed the effect of inaccurate estimations on field monitoring.

Methods: The field probe positions were estimated by 1) assuming ideal gradient fields, 2) using measured gradient fields (including nonlinearities), and 3) using measured gradient fields with relative position constraints.

The fields measured with the NMR field camera were compared to fields acquired using a dual-echo gradient recalled echo B_0 mapping sequence. Comparisons were done for shim fields from second- to fourth-order shim terms.

Results: The position estimation was the most accurate when relative position constraints were used in conjunction with measured (nonlinear) gradient fields. The effect of more accurate position estimates was seen when compared to fields measured using a B_0 mapping sequence (up to 10%–15% more accurate for some shim fields).

The models acquired from the field camera are sensitive to noise due to the low number of spatial sample points.

Conclusion: Position estimation of field probes in an NMR camera can be improved using relative position constraints and nonlinear gradient fields. **Magn Reson Med 80:380–390, 2018. © 2017 International Society for Magnetic Resonance in Medicine.**

Key words: Field monitoring; NMR field camera; NMR field probes; position calibration; high order B_0 shim.

INTRODUCTION

Spatiotemporal monitoring of the B_0 field can be used to measure the dynamics of the MR systems and has a variety of applications. The dynamics can be used to perform preemphasis for correcting eddy currents (1–3), frequency stabilization (4), and field stabilization with online control of the B_0 shim fields (5–7). Spatiotemporal monitoring of the B_0 field requires fast measurements of the B_0 field without compromising the spatial accuracy.

For this purpose, projection-based B_0 mapping methods such as FASTMAP (8,9) and FASTMAP (10) can be used. These methods can also be integrated into the sequence to perform real-time B_0 shimming (5,11). Alternatively, spatiotemporal monitoring can be done using very low-resolution B_0 maps or B_0 shim navigators (6,12,13). All of the above-mentioned methods need to be included in the pulse sequence, which increases the complexity of implementation and also the scan duration.

Alternative to these sequence-based techniques, one can use NMR field probes (henceforth referred to as field probes) for spatiotemporal monitoring (14,15). A field probe can measure the B_0 magnetic field at a single spatial point at a very high temporal resolution. An array of field probes (often called a field camera) can be used to measure the B_0 at many spatial points simultaneously (16,17). A field camera can be used independently of the MRI scanner and thus requires no additional scan time. The positions of the field probes need to be estimated before monitoring. One disadvantage of using the field camera is that it requires additional hardware.

A comparison of the different B_0 field measurement methods shows that there is a tradeoff between the spatial and temporal resolution of monitoring the B_0 field (Fig. 1). For applications in which high spatial resolution is required (e.g., calibrating shim systems), an entire B_0 map should be acquired. For applications in which high temporal resolution is required, the projection-based or low-resolution B_0 mapping methods should be employed. If even faster dynamics of the B_0 field need to be measured, use of a field camera can be appropriate. However, field cameras usually only have up to 16 field probes and thus have very low spatial resolution. Due to the low spatial resolution of the field camera, the B_0 field cannot be completely determined using a few sample points. Instead, the sample points are used to derive an approximation of the B_0 field using spherical harmonic decomposition (18,19). Spherical harmonic decomposition approximates arbitrary B_0 fields using a set of orthogonal basis functions (the Legendre polynomials). This is a common method of approximating and modeling B_0 fields (8,9,16,20).

Field probes and field cameras have been extensively used in (15–17) for dynamic field monitoring and in (4,7) for real-time feedback. In this study, we show that we can improve the spatial accuracy of the field camera by introducing prior knowledge about the field camera structure and about the gradient nonlinearities into the

[1]Max Planck Institute for Biological Cybernetics, Tuebingen, Germany.
[2]IMPRS for Cognitive and Systems Neuroscience, Eberhard-Karls University of Tuebingen, Germany.
[3]Department of Physics, Eberhard-Karls University of Tuebingen, Germany.
[4]Department of Biomedical Magnetic Resonance, Eberhard-Karls University of Tuebingen, Germany.
[5]Department of Physics, University of Greifswald, Greifswald, Germany.
*Correspondence to: Paul Chang, Max Planck Institute for Biological Cybernetics, Max-Planck-Ring 11, 72076 Tübingen, Germany.
E-mail: paul.chang@tuebingen.mpg.de.

Received 22 June 2017; revised 23 October 2017; accepted 25 October 2017
DOI 10.1002/mrm.27010
Published online 20 November 2017 in Wiley Online Library (wileyonlinelibrary.com).

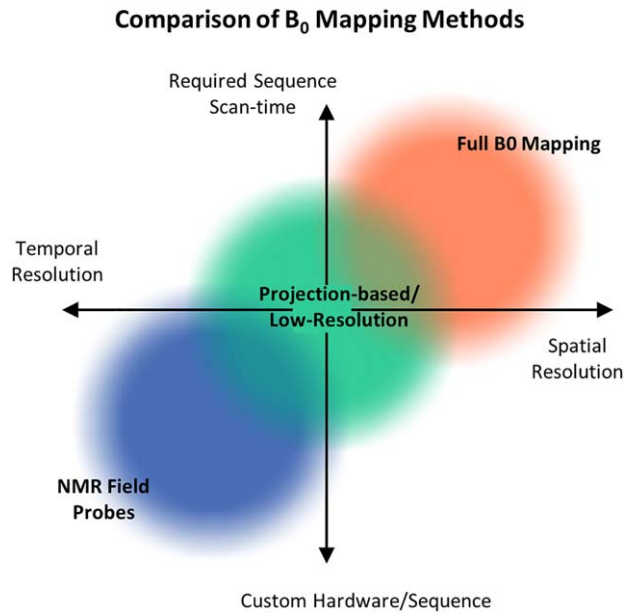

FIG. 1. Qualitative comparison of different B_0 mapping methods show a clear tradeoff between the spatial and temporal resolution. Although field probes require more special hardware, they can be used independently of the MRI scanner and thus do not increase the scan duration.

position calibration. We then extensively compare B_0 maps measured with a large number of field probes to static B_0 maps acquired using a full B_0 mapping sequence. We show that small perturbations in the measurements can result in spatial measurement inaccuracies despite the large number of field probes used in this study.

THEORY

The physics of field probes goes back to the very basics of MR. A field probe is a small sample of water (or fluorine (4,7) or ^{2}H (21) for in vivo measurements) that is excited using a small RF coil to generate a FID. It is well-known that the frequency of the FID (which can be calculated from the phase) is related to the magnetic field strength through the gyromagnetic ratio. Because the water or fluorine sample in the field probes is small, the magnetic field strength of this small volume at this position can be measured:

$$f = {}^{d\varphi}/_{dt} = \gamma B, \qquad [1]$$

where f is the frequency, γ is the gyromagnetic ratio, and B is the magnetic field strength. The gyromagnetic ratio of proton is approximately 42.576 Hz/uT.

Usually, several field probes are used to measure many spatial locations of the field simultaneously. These measurements are then modeled by spherical harmonic decomposition using Legendre polynomials to measure the spatiotemporal field dynamics. Legendre polynomials are used because they provide a number of benefits, such as orthogonality, coverage of a 3D space, and ease of use.

In order to decompose the B_0 field using spherical harmonics, the positions of the field probes (relative to the scanner) need to be determined prior to the measurements. In the case of field cameras, despite the field probes being mounted in fixed positions, accurately obtaining their positions relative to the scanner can be complicated. Even in the construction of the field camera, the field probes may be slightly misplaced. Furthermore, because the field probes are often encapsulated inside an epoxy mold (14), this may cause even more inaccuracies in the construction and prevent accurate relative position calibration based on optical methods.

Currently, the method of estimating the positions of the field probes is to use the scanner gradients. Known gradient strengths are applied in each of the *x*-, *y*-, and *z*-directions, and positions can be estimated from the measured frequencies of the field probes (16) using the following equation:

$$f = \gamma \cdot B = \gamma \cdot G_x \cdot x - f_{off\_res}, \qquad [2]$$

where f_{off_res} is the off-resonance calculated from FID without any gradients applied (as the reference); G_x is the gradient strength in the *x*-direction; and x is the *x*-position. Because the applied gradient strength is known and the frequency can be measured, the *x*-position can be estimated. Similarly, applying a gradient in the *y*- and *z*-directions gives us the *y*- and *z*-positions, respectively.

The problem with this method is that it relies on the assumption of the gradient fields being perfectly spatially linear. Unfortunately, deviations in the linearity of the gradient may introduce an error in the position estimate of the field probes. Note that this is not a problem if we only want to monitor first-order B_0 terms because the nonlinearities cancel each other out; however, for higher order spherical harmonic terms, the accuracy of the decomposition is heavily dependent on the accuracy of the position estimates.

Gradient spatial nonlinearities can be modeled using the following nonlinear equation:

$$f = \gamma \cdot G_x(x) - f_{off\_res}. \qquad [3]$$

This is simply a generalization of Equation (2).

METHODS

All the measurements were performed on a 9.4T Siemens human whole-body MR scanner (Erlangen, Germany). B_0 monitoring using full B_0 mapping was compared to B_0 monitoring using a field camera. The B_0 fields were generated from shim fields produced by a Resonance Research Inc. 28-channel insert shim (Billerica, MA) that has zero-, second-, third-, and fourth-order spherical harmonics and partial fifth- and sixth-order terms. For this investigation, only the shim terms up to the fourth order were used.

Each of the shim fields were measured using a high-resolution 2D dual-echo (gradient recalled echo (GRE)) B_0 mapping sequence. The reference field maps were acquired on a 170-mm diameter silicon oil spherical phantom with an eight-channel transceiver coil array (22). The sequence parameters were: resolution = $1.56 \times 1.56\,mm^2$; FOV = $200 \times 200\,mm^2$; slice thickness = 3 mm; slices = 40 (distance

Table 1
Shim Terms and Insert Shim Coil Sensitivities

Shim Term	Spherical Harmonic Function	Sensitivity ($Hz/cm^n/A$)
Z0	1	6058
Z2	$z^2-1/2*(x^2+y^2)$	6.942
ZX	zx	24.15
ZY	zy	24.15
C2	x^2-y^2	3.64
S2	2xy	3.64
Z3	$z(z^2-3/2*(x^2+y^2))$	0.4923
Z2X	$x(z^2-1/4*(x^2+y^2))$	1.0
Z2Y	$y(z^2-1/4*(x^2+y^2))$	1.0
ZC2	$z(x^2-y^2)$	1.77
ZS2	2zxy	1.77
C3	$x(x^2-3y^2)$	0.188
S3	$y(3x^2-y^2)$	0.188
Z4	$z^4-3z^2(x^2+y^2)+3/8*(x^2+y^2)$	0.04206
Z3X	$zx(z^2-3/4*(x^2+y^2))$	0.123
Z3Y	$zy(z^2-3/4*(x^2+y^2))$	0.123
Z2C2	$z(x^2-y^2)(z^2-1/6*(x^2+y^2))$	0.093
Z2S2	$2z(xy)(z^2-1/6*(x^2+y^2))$	0.093
ZC3	$x(x^2-3y^2)(z^2-1/8*(x^2+y^2))$	0.121
ZS3	$x(x^2-3y^2)\ (z^2-1/8*(x^2+y^2))$	0.121
C4	$x^4-6x^2y^2+y^4$	0.0187
S4	$4xy(x^2-y^2)$	0.0187

factor = 20%); TR = 1,200 ms; TE = 4.00/4.76 ms; and readout bandwidth = 1,500 Hz/px. B_0 maps were acquired for each of the shim channels of the Resonance Research Inc. insert shim (up to and including the fourth-order terms) by applying a current of 1.0 A. The sensitivities of the shim coils are given in Table 1.

These reference field maps were used as the benchmark B_0 fields and compared to the B_0 fields measured using a field camera. No gradient distortion correction was applied by the scanner in the image reconstruction.

A field camera consisting of 12 ^1H field probes was constructed (Fig. 2). The field probes were positioned on three layers at spacings of 56.25 mm. Each layer had four field probes, with equidistant spacings of 82.5 mm between adjacent field probes. To reduce the T_1 relaxation time of the field probes, the field probes were doped with $CuSO_4.5H_2O$ (16). However, due to the higher magnetic field strength, a lower doping concentration was recalculated based on (23) to be 3.0 g/L. The ^1H samples were contained inside a 10-mm glass capillary tube with an inner diameter of 0.8 mm. The field probes were encapsulated using doped epoxy to minimize magnetic susceptibility and homogenize the field within the field probe (24). The field probe samples were tilted at 45 degrees relative to the B_0 direction, which decreases the SNR. However, the SNRs of the field probes were sufficiently high (1,200–4,200) for the 12 probes of the field camera. The SNR was taken as the maximum amplitude of the water signal over the SD of the noise region. The field probes were also decoupled with cable traps tuned to the proton Larmor frequency (Fig. 2). An in-house splitter and transceiver chain were used to acquire the FIDs of the field probes using the MR scanner. A FID pulse sequence with the following parameters was used to acquire the FIDs: rectangular pulse excitation with 0.5 ms duration, 5 V; sampling rate = 100 kHz; vector size = 2,048; TR = 25 ms.

Before using the field camera to measure the B_0 fields of the insert shim, different position calibration methods were investigated to improve the position estimates of the field probes of the field camera.

Position Calibration

The actual positions of the field probes of the field camera with respect to each other needed to be measured for the position calibration study. However, the epoxy encapsulation of the field probes made the accurate measuring of the actual positions of the field probes difficult. To locate the actual positions of the field probes within the epoxy molds, a CT scan of the field camera was acquired. A CT scanner was chosen to circumvent the image distortions of the MR modality (due to the gradient nonlinearities or B_0 inhomogeneity). The resolution of the scan was: [1, 1, 0.6386] mm in the respective x-, *y*-, and z-directions.

The positions were marked and calculated from the CT scan and were then used as the reference positions. These positions could then be compared to the positions estimated using the MRI scanner.

Three different methods were used to estimate the positions of the field probes using the MRI scanner. The first method (denoted as *lin*) uses Equation [2] and assumes that the gradient fields are spatially linear (16,17). The second method (denoted as *nonlin*) considers the gradient field spatial nonlinearities by using Equation [3] for each field probe of the field camera. The last method uses the gradient nonlinearities in combination with the CT scan positions. Thus, the positions of all the field probes are optimized simultaneously by incorporating relative position constraints obtained from the CT scan positions. This method is denoted as *connonlin* (constrained nonlinear estimation).

For the nonlinear methods that use Equation [3], the $G_r(r)$ for $r \in [x, y, z]$ needs to be known for each gradient

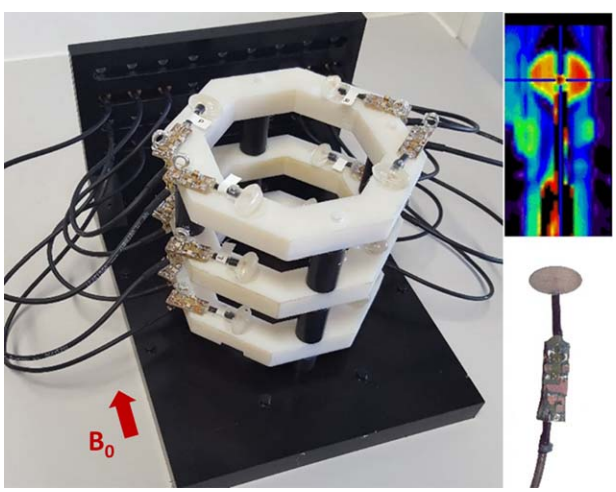

FIG. 2. The field camera (left) consists of 12 field probes (bottom-right). The direction of the B_0 field is also indicated. The CT scan of the field probe (top-right) shows that the sample within the epoxy mold can be easily identified.

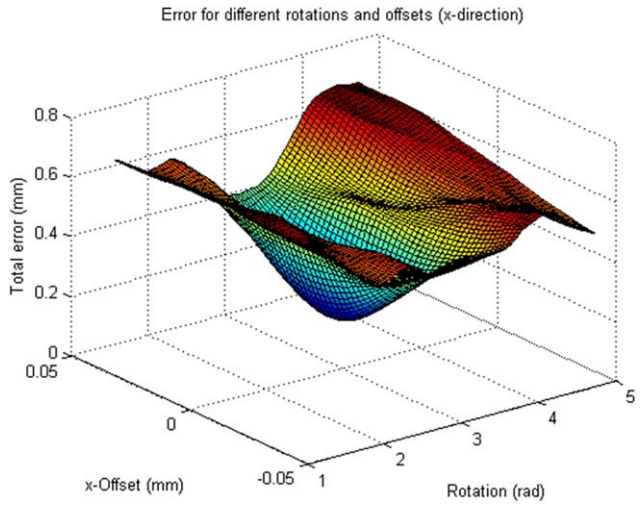

FIG. 3. The objective function for the position optimization for two of the parameters (*x*-position and θ-rotation). The objective function is the norm of the difference between the measured and predicted frequencies calculated from the gradient field models.

direction. Once we have a model for $\boldsymbol{G}(\boldsymbol{r}) = [G_x(\boldsymbol{r}), G_y(\boldsymbol{r}), G_z(\boldsymbol{r})]$, the frequencies measured at any position r can be estimated using Equation [2]. Therefore, we can find the optimal position (in the linear least squares sense) by solving the following minimization problem:

$$\min_{\boldsymbol{r}} ||\boldsymbol{f}_{\boldsymbol{meas}} - \gamma \boldsymbol{G}(\boldsymbol{r})||^2. \qquad [4]$$

In this equation, $\boldsymbol{G}(\boldsymbol{r})$ is the spatial model of the gradient fields and $\boldsymbol{f}_{\boldsymbol{meas}}$ are the frequencies measured for each corresponding gradient. To acquire the spatial model $\boldsymbol{G}(\boldsymbol{r})$, the gradient fields needed to be measured in a manner that is independent of the MR scanner to avoid biased estimates in the MR hardware and image reconstruction. Therefore, gradient fields were measured by using a single field probe and moving it to different positions on a fixed 3D grid. The dimensions of the sampling grid were $9 \times 4 \times 9$ (in the *x*–*y*–*z* dimensions), with a spacing of $32 \times 30 \times 32$ mm between each sample. The frequencies (and thus magnetic field strength) at each of these positions were measured for each of the gradients. These data were then used to model the nonlinearities of the gradient fields by decomposing them using up to fourth-order spherical harmonic functions:

$$\boldsymbol{G}(\boldsymbol{r}) = \sum_{l=0}^{N} \sum_{m=-l}^{l} k_l^m S_l^m(\boldsymbol{r}), \qquad [5]$$

where k_l^m is the coefficient corresponding to the spherical harmonic function S_l^m, and where N is the maximum order of the decomposition; l is the degree; and m is the order. Note, that if the gradients are perfectly linear, this reduces to $\boldsymbol{G}(\boldsymbol{r}) = \boldsymbol{G} \cdot \boldsymbol{r}$, which is the same as Equation [2].

A Newton optimization algorithm can be used to calculate the position of a single field probe. This algorithm is known for its quadratic convergence rate but is usually problematic because the Hessian matrix needs to be calculated at every step, and also because it does not always converge if a poor starting point is chosen. In this case, these are not significant problems because the function $\boldsymbol{G}(\boldsymbol{r})$ is a sum of polynomials (Eq. [5]) and thus the Hessian is relatively easy to calculate from the Jacobian. Additionally, if the starting point is chosen by assuming perfectly linear gradient fields, this should be a relatively good approximation of the optimal point, and thus initializing the starting point should not be a problem. This means that an optimization method with quadratic convergence speed can be used and the algorithm was found to typically converge in one step; the threshold for convergence was 1e-6. The *nonlin* method thus used this algorithm to calculate the positions for each of the field probes. The calculations for the Jacobian and Hessian are given in more detail in the Appendix (available online).

For the *connonlin* method, the positions of the field probes are fixed (relative to each other) and can thus be considered a rigid body. Therefore, only three translation and three rotation parameters $\tau = [x, y, z, \theta, \varphi, \rho]$ need to be

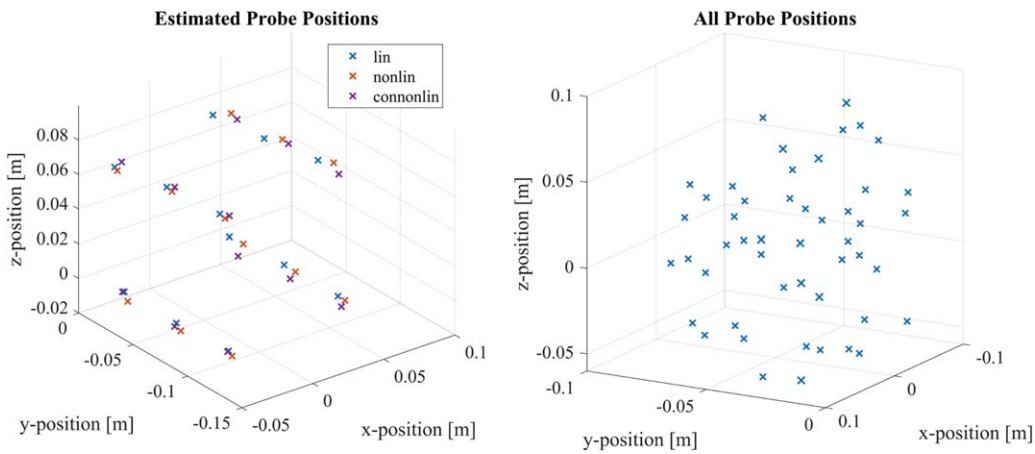

FIG. 4. The positions of the field probes (for one position of the field camera) using each of the three-position optimization methods (left). The differences are quite significant and can sometimes be more than 10 mm. All the field probe positions resulting from several field camera positions, limited to a 100-mm radius from the isocentre, are also shown (right).

found to find the optimal positions of all the field probes. The optimization problem from Equation (3) then becomes:

$$\min_{\tau=[x,y,z,\theta,\varphi,\rho]} \sum_{p=1}^{N_p} ||\boldsymbol{f}_{meas} - \gamma \boldsymbol{G}(\boldsymbol{r}(\boldsymbol{\tau}))||^2. \quad [6]$$

As an example, Figure 3 shows the optimization objective function for two of the parameters (*x*-coordinate and θ-rotation). The optimization was performed with a Newton optimization algorithm (implemented in C++) using the Jacobian and Hessian matrices with respect to the variable $\boldsymbol{\tau}$ (details are given in the Appendix, available online). The initial position and rotation parameters were calculated by using the *lin* method and registering the estimated positions to the relative positions of the field camera acquired from the CT scan.

B_0 Mapping Validation

As previously mentioned, field cameras use spherical harmonic decomposition to describe B_0 fields. Therefore, the number of measured sample points need to be greater than (or equal to) the number of spherical harmonic coefficients. Also, the sample positions are also important and need to be sufficiently well distributed for the matrix S in Equation [5] to be well conditioned (25). Because we used shim terms up to and including fourth-order spherical harmonics, each shim field was decomposed using up to fourth-order spherical harmonic functions. This resulted in a total of 25 coefficients that needed to be determined for each shim field. To acquire enough points, the field camera was placed in eight different positions to measure the shim fields. Eight positions and 12 field probes on the field camera gave 96 sample points of each shim field. However, all points outside of a 100-mm radius (from the isocenter) were discarded to be consistent with the FOV of the B_0 mapping.

A current of 1.0 A was applied to each of the shim channels for the measurements. Note, that when measuring the shim fields, the shim channels were switched on for several seconds (at least 5 s) before acquiring the FIDs using the field camera. This was to allow most eddy currents to settle before acquisition.

The field camera was calibrated using three different position estimation methods (*lin, nonlin*, and *connonlin*), and thus each calibration gave a different set of spherical harmonics coefficients. We determined which set of coefficients was more accurate by comparing them to the reference shim maps (acquired using a full B_0 mapping sequence). To compare these fields to the reference maps, the coefficients were used to reconstruct the field on a $200 \times 200 \times 200\,mm^3$ FOV. The errors between these reconstructed fields and the reference maps were compared using the SDs, as well as the Pearson product moment to compare the similarity between the reconstructed fields (26). The Pearson product-moment coefficient is defined as:

$$\rho_{X,Y} = \frac{cov(X,Y)}{\sigma_X \sigma_Y}. \quad [7]$$

This coefficient is a measure of the similarity between the two signals, which results in a value between −1 and 1, for which 1 indicates that the signals are identical and 0 indicates that there is no correlation between the signals.

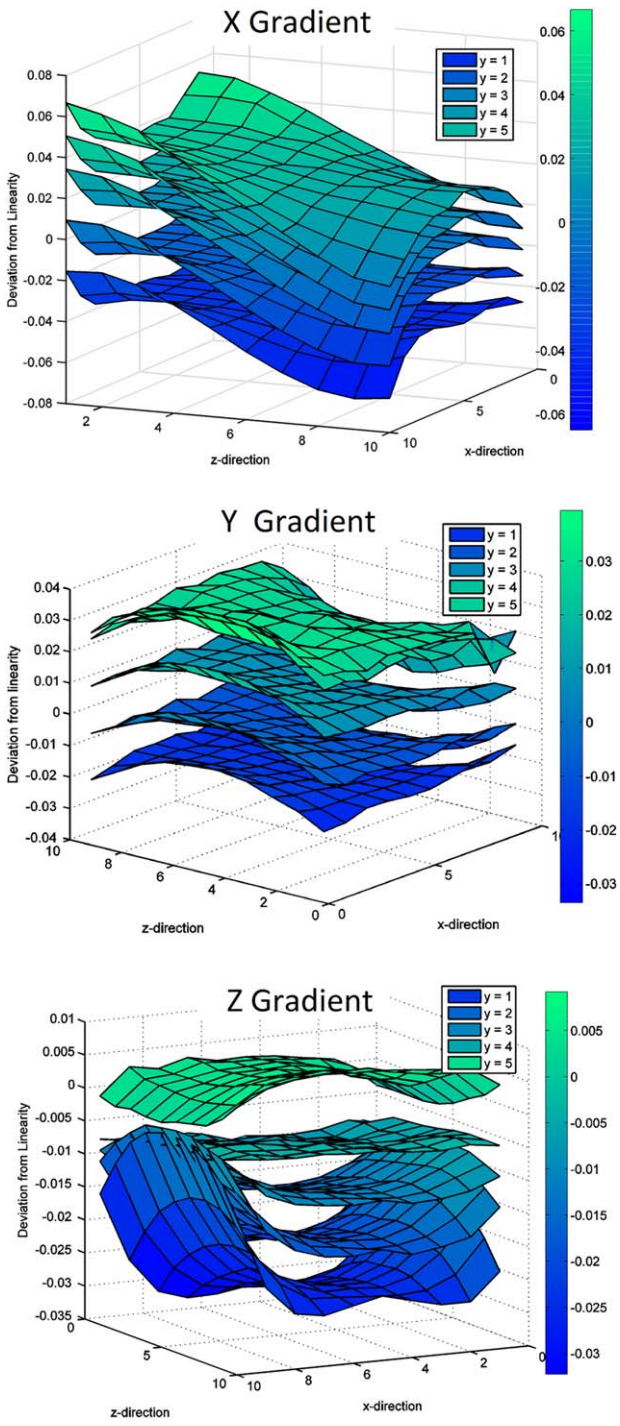

FIG. 5. The normalized gradient field deviation for 1 mT/m from spatial linearity are shown for five slices (y = 1…5), that is, if the gradient fields were perfectly linear, then each plane would be flat. The deviations are shown in percentage (of the gradient field strength).

Any error between the reconstructed and reference maps is a combination of the error in the position estimation and the error due to downsampling the B_0 field by acquiring only a few sample points with the field camera. We isolated and investigated the effect of downsampling by decomposing the fully sampled reference

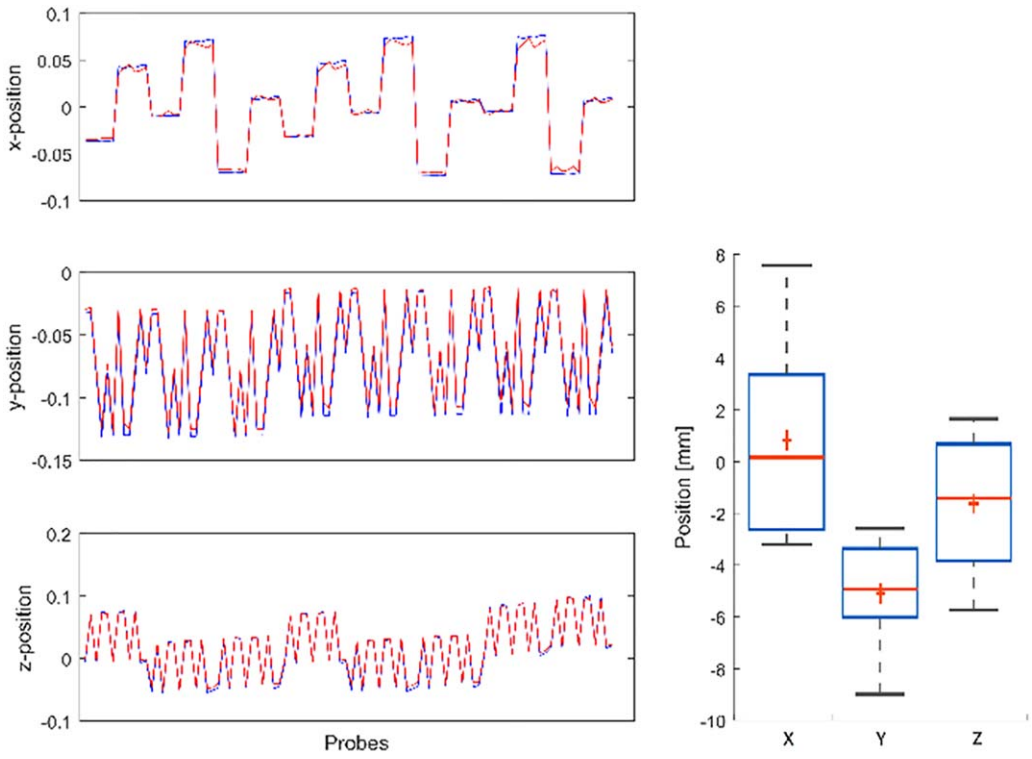

FIG. 6. (Left) The normalized gradient field frequencies for 1 mT/m for 96 field probes (blue) are compared to the frequencies measured from the reference field map using a B_0 mapping sequence (red). The figure shows good agreement between the two measuring techniques. (Right) The normalized mean differences between the frequencies shown on the left.

maps using only the sample points given by the constrained field camera positions. This is theoretically the most accurate B_0 field that we can acquire using a field camera (with the same number of sample points).

These decomposition coefficients were then compared to the original reference maps. Any resulting error is thus only due to downsampling.

Simulations

We performed simulations to investigate the possible factors causing differences between the position calibration methods. The simulations were performed as follows:

1. The field probe positions measured from CT scanner were used as the actual positions.
2. The frequencies at these positions for the *x*-, *y*-, and *z*-gradients were simulated using the fourth-order gradient models.
3. These frequencies were used to calculate the positions using the *lin, nonlin*, and *connonlin* methods.
4. The positions were used to decompose:
    a. The ideal theoretical shim fields; and
    b. The ideal theoretical shim fields with added random white Gaussian noise.
5. The decomposed models were then compared by reconstructing the field on a $100 \times 100 \times 100\,\text{mm}^3$ FOV (as described above).

A range of noise levels were simulated: 0.5%, 1%, 2%, and 5% of the shim coil strength.

RESULTS

Position Calibration

The positions of the field probes measured using the CT scanner can be seen in Figure 4 (see *connonlin*; this method uses the CT scanner data). The deviation of the distance between the *connonlin* and the *nonlin* is on average 5.0 ± 1.4 mm, with a maximum error of 7.0 mm. Similarly, the deviation of the distance between the *connonlin* and the *lin* method is on average 8.8 ± 4.0 mm, with a maximum error of 14.5 mm. As a reminder, the *lin* is the current method (in the literature) used to calculate the positions of the field probes, where the gradient fields are assumed to be spatially linear.

As mentioned earlier, the field camera was moved to multiple positions for the measurements to increase the number of spatial points (an effective total of 49 field probes). The distribution of the field probe positions calculated using the *connonlin* method are shown in Figure 4.

These positions were estimated based on measured gradient fields. The gradient field measurements showed that the fields were spatially relatively linear. The deviations from the ideal linear case are shown in Figure 5 (i.e., if the fields were perfectly linear, then each plane in the figure would be flat). The figure shows that there are still slight deviations from linearity. These gradient field measurements were modeled using up to fourth-order spherical harmonic coefficients. It was previously shown that the accuracy of the model saturates after approximately the sixth or seventh order (27). We thus further compared modeling the gradient fields using

sixth- and fourth-order decomposition. The Pearson product-moment coefficients were 0.9912, 0.9968, and 0.9945 for the *x*-, *y*-, and *z*-gradient fields, respectively (comparing fields reconstructed on a $200 \times 200 \times 200$ mm FOV). Because the coefficients were very close to 1.0, this showed that the difference between the fourth-order and sixth-order models was insignificant.

B_0 Mapping Validation

Firstly, we compared the field probe measurements to the B_0 mapping measurements of the gradient fields. Figure 6 shows the normalized frequencies of the gradient field reference maps compared to the field probes. The figure shows that, for the gradient fields, the frequencies measured from the field camera are very similar to the frequencies of the reference maps (acquired from the B_0 mapping sequence). Figure 6 shows that the mean error between the frequencies was 0.0008 mT/m, −0.0051 mT/m, and −0.0016 mT/m for the *x*-, *y*- and *z*-gradients, respectively (with gradient strength 1 mT/m). For spatially linear gradients, this translates into a position error of 0.8 mm, −5.1 mm, and −1.6 mm in the *x*-, *y*- and *z*-directions, respectively. Note that the slightly higher position error in the *y*-direction may be due to the distribution of the field probes covering mostly only the lower *y*-positions (with respect to the isocenter) (Fig. 6). If the field probes were more centered in the *y*-direction, then this error would most likely reduce (because gradients are more nonlinear further from the isocenter). The Pearson product-moment coefficients were 0.9990, 0.9968, and 0.9945 for the *x*-, *y*-, and *z*-gradients, respectively. This metric indicates that the modeled-and-measured gradient fields were very similar.

After the gradient fields, we analyzed the shim fields of the insert shim. The reconstructed maps (using the field probes) were compared to the reference shim field maps (acquired using a B_0 mapping sequence). A comparison of the reconstructed fields is shown in Figure 7 (only second-order terms are shown for illustration purposes). The fields were reconstructed for the B_0 mapping and for the field-probe measurements with two different field-camera calibrations, using the linear estimation and the constrained optimization method.

The root-mean-squared error (RMSE) for each shim field was calculated, and respective results are shown in Figure 8a. There was no single position calibration method that was the most accurate for every shim field. However, the *connonlin* method gave more consistent results. For example, shim terms ZX and Z3 were poorly estimated using the *lin* and *nonlin* methods, whereas the *connonlin* method was able to drastically improve the accuracy of measuring the B_0 map. However, the *nonlin* method gave slightly better accuracy than the *lin* method for most shim fields. Therefore, if the relative positions of the probes are unknown, using the gradient fields for estimating the positions still improves the accuracy of the position estimates.

Also shown on Figure 8a is the RMSE between the reference map and the downsampled reference map. As mentioned in the previous section, the reference map was spatially downsampled using the field probe positions. This value indicates the intrinsic error of spatial downsampling; in other words, this would be the error if the position calibration was perfect. The ZX, Z3, Z4, and ZC3 shim fields deviate the most and the largest improvements from the *connonlin* method is seen for the ZX, Z3, ZC2, ZS2, and ZC3 terms.

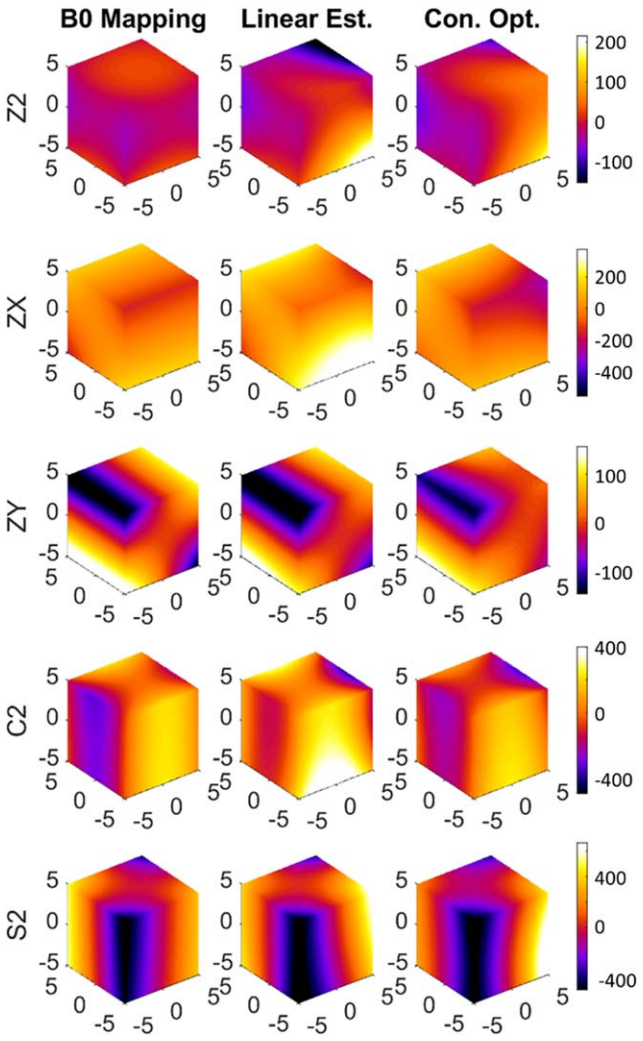

FIG. 7. Shim fields for the second-order terms measured using B_0 mapping (original reference maps) and measured using the field camera (with linear estimation and constrained optimization for position calibration). The fields are shown in Hz (for 1.0 A).

The RMSE for each shim field was also calculated for the simulated results without noise (Fig. 8b). The level of error of only downsampling is similar to the measured data. As expected, the *connonlin* method reaches the same level of error as the downsampling case.

Simulations

Figure 9 shows the simulated fields (resulting only from downsampling) with different levels of noise: 0.5%, 1%, 2%, and 5%. The trend of the deviations between the theoretical fields and the reconstructed fields from simulations is similar to the deviations in the measured data in Figure 8a.

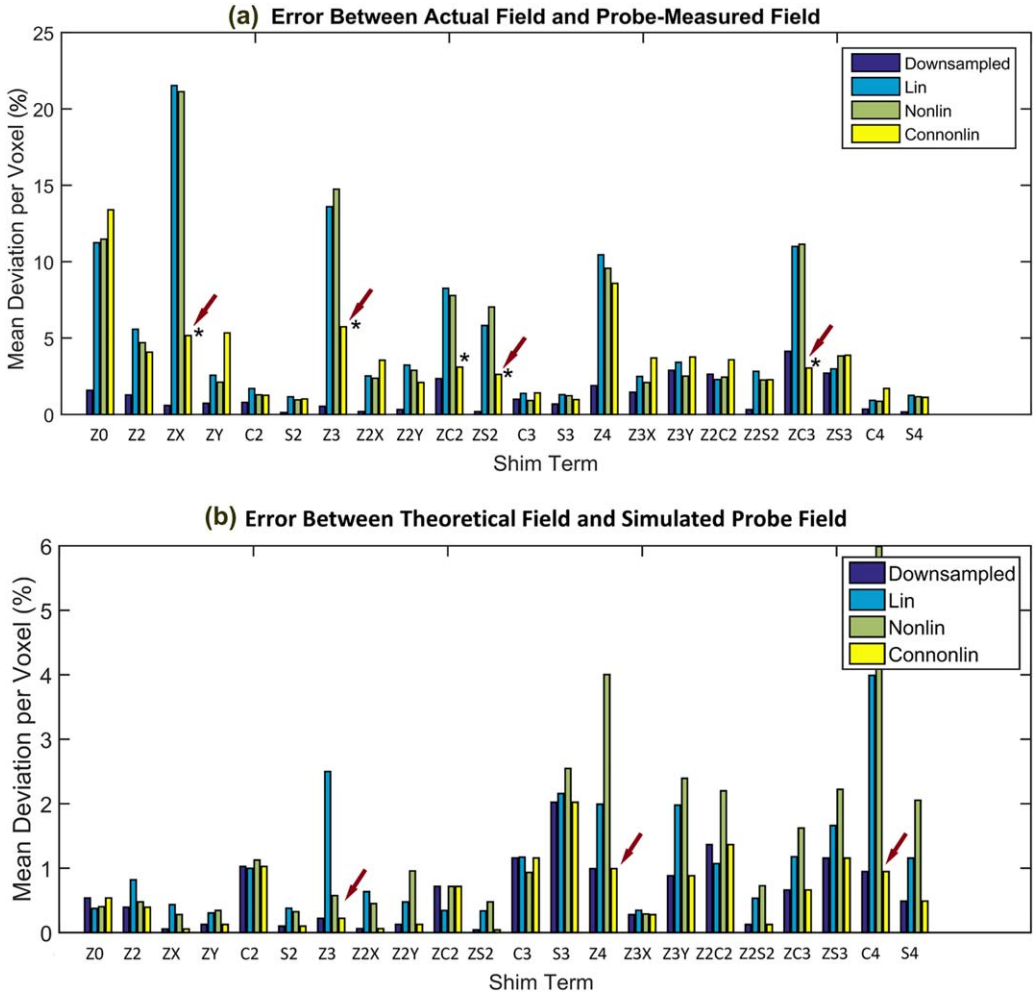

FIG. 8. Mean deviation between the reference shim field maps and the field probes measurements (top). The significant improvements of the *connonlin* method are shown (*). Also shown are the RMSEs of the theoretical fields and the simulated fields from the field probes calculated from simulations (bottom). In both cases, although the *connonlin* position optimization does not always perform better, it is more consistent and can improve the accuracy of most B_0 fields. RMSE, root-mean-square error.

DISCUSSION

Position Calibration

Three different calibration methods for calculating the positions of the field probes in a field camera were investigated. In the current literature, only the linear estimation has previously been used. However, our investigation showed that this is not sufficient for accurate B_0 monitoring. Instead, a constrained nonlinear optimization should be used. This requires that the relative field probe positions be measured (which we did using a CT scan), and also requires that the gradient field

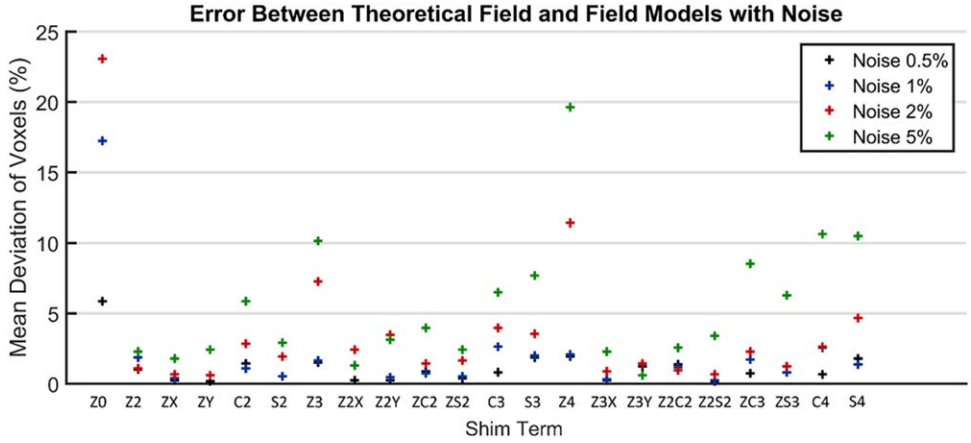

FIG. 9. Mean deviation between the theoretical shim fields and the downsampled field probe fields calculated from simulations. Different levels of noise were applied to the simulated shim fields, and the reconstructed fields were compared. The trend of the deviations is similar to the results from the measured field probe data.

nonlinearities be measured and modeled. The *connonlin* method gave the best consistency of monitoring the B_0 field.

As shown previously in the results section, the gradient fields could be sufficiently modeled using a fourth-order decomposition. Increasing the modeling order to six resulted in very similar coefficients. This is because the gradient fields only have small imperfections. Another limiting factor on spherical harmonic decomposition is the fact that it inherently is radially symmetric, which means that local asymmetric inhomogeneities of the field cannot be properly modeled. The caveat is that, as we have seen, small differences in the field probe positions result in the B_0 field models differing significantly. Therefore, the position of the field probes should be determined as accurately as possible. To overcome slight modeling errors in the gradient fields, a constrained position calibration optimization is recommended.

Intuitively, the constrained optimization should yield the most accurate result because it considers the fixed positions of the field probes and also considers the gradient nonlinearities. The results of the position calibration of the 12-probe field camera showed that consideration of the gradient field nonlinearities significantly affected the estimated positions of the field probes; that is, the difference could be more than 10.0 mm, which in turn will affect the spherical harmonic decomposition. Furthermore, the *nonlin* optimization showed very similar results to the *connonlin* optimization for the gradient fields, indicating that the gradient fields were relatively well modeled in this region and that the two methods are in agreement. Although this implied that the *nonlin* optimization could be used for position calibration, the *connonlin* approach was still used because it was more robust in measuring the B_0 fields.

B_0 Mapping Validation

The reference shim field maps were used as the benchmark fields because the spatial resolution that can be achieved by using the mapping sequence is much greater and thus gives more spatial fidelity. Although the mapping sequence is susceptible to imaging artifacts induced by, for example, gradient nonlinearities and geometric distortion, the artifacts should be minimal because the phantom's spatial coverage was within the gradient fields' linear range and the high readout bandwidth minimized the geometric distortion (27). However, it should be noted that the magnetic susceptibility of the material used for the B_0 mapping setup and the field camera setup were different and could thus result in slight inconsistencies between the two methods.

The results show that the low spatial sampling of the field camera (compared to the B_0 mapping sequence) is an important factor in the accuracy of the field model. Even when the positions of the field probes are perfectly calibrated, the field model still deviates significantly from the mapping sequence model. This is shown by the error of the downsampled field (Fig. 7). There are two contributing factors for the error between the downsampled field and the field maps: 1) the lower spatial resolution, and 2) the field models were calculated using up to fourth-order spherical harmonic terms. Therefore, the higher spatial frequency information (and field imperfections) cannot be accurately modeled with fourth-order terms. This is also consistent with the level of error shown in the simulations compared to the measured data (Fig. 8). It was also shown in (27) that there is a significant loss of accuracy when the fields are modeled using up to fourth-order terms instead of using up to sixth-order terms. Andersen et al. (25) also found that using 16 field probes is not sufficient to model the field using up to third-order decomposition.

The field comparison was performed by reconstructing the fields from the spherical harmonic coefficients and comparing the difference between them. The field coefficients were not directly used as a comparison because they are difficult to interpret. Firstly, the coefficients depend on the units of measurement that they are decomposed with. For example, decomposing using meters will result in the coefficients increasing exponentially with the order of the spherical harmonic function, whereas decomposing using centimeters results in the coefficients an exponential decrease with the order. This makes it difficult to compare B_0 fields using only coefficients due to the different orders of magnitudes of the coefficients. Secondly, coefficients are difficult to compare because two similar fields can have widely varying coefficients, especially if the measurements are noisy. Thus, the fields were reconstructed from the coefficients to better perform the comparison of the models.

The results showed that comparing the RMSE between the models (in Hz) using the *connonlin* optimization was the most similar to the downsampled model from the mapping sequence. The remaining difference between the downsampled model and *connonlin* model can be explained by the noise in the B_0 maps or field-probe measurements (because the signals dephase in strong applied fields). The models acquired from the field camera are sensitive to noise due to the low number of spatial sample points. The noise level is similar to the simulated noise levels for approximately 1% to 2% noise. This noise can be result from measurement noise or any inconsistencies between the B_0 mapping setup with the phantom and the field camera setup. A limitation of this study is that the magnetic susceptibility effects of the field camera mount material were not matched to the field probe. Therefore, the measured magnetic fields could deviate between the two setups. Although for position calibration purposes this would be minimized because of the relative position constraints, the effect of the magnetic susceptibility could explain the residual inconsistencies between the two field measurement methods.

The difference between the RMSEs showed that the linear optimization of the position calibration can lead to significant errors in the modeled B_0 fields. Although using *connonlin* optimization can reduce the errors, for some shim channels they could not be reduced any further.

CONCLUSION

In this study, we compared position calibration methods for the field probes. We introduced a method that used information about the gradient field spatial nonlinearities

and relative field probe positions to estimate the probe positions.

Furthermore, we compared the spatial fidelity of the field camera to B_0 mapping sequences. We showed that a limited number of field probes (thus reduced number of sample points) resulted in a loss of spatial accuracy. Furthermore, a constrained optimization calibration yielded the best results for the shim fields. However, for some shim fields, all calibration methods performed similarly.

The low spatial sampling of the field camera results in an unavoidable loss of spatial accuracy. The linear position calibration method that is currently used is more inaccurate than a constrained optimization method that uses prior knowledge about gradient nonlinearities and relative field probe positions. A more accurate probe position estimate means that field monitoring will be more accurate, especially for higherorder terms. Therefore, B_0 shimming with the field camera will be more accurate.

APPENDIX

The Jacobian and Hessian for the optimisation functions from Equations [4] and [5] can be calculated as follows. For the cost function:

$$\boldsymbol{F} = ||\boldsymbol{K}(\boldsymbol{r}) - \boldsymbol{f_{meas}}||2$$

where $\boldsymbol{K}(\boldsymbol{r})$ is defined as $\gamma\boldsymbol{G}(\boldsymbol{r})$, and $\boldsymbol{G}(\boldsymbol{r})$ is defined by Equation [5], the Jacobian is:

$$\nabla\boldsymbol{F} = (\boldsymbol{K}(\boldsymbol{r}) - \boldsymbol{f_{meas}})^T \cdot \nabla\boldsymbol{K}(\boldsymbol{r})$$

and the Hessian is:

$$\nabla^2\boldsymbol{F} = \nabla\boldsymbol{K}(\boldsymbol{r})^T \cdot \nabla\boldsymbol{K}(\boldsymbol{r}) + (\boldsymbol{K}(\boldsymbol{r}) - \boldsymbol{f_{meas}})^T \cdot \nabla^2\boldsymbol{K}(\boldsymbol{r})$$

Since $\boldsymbol{K}(\boldsymbol{r})$ is a linear combination of Legendre polynomials (Eq. [5]), the partial derivatives are given by:

$$\begin{aligned}
\frac{\partial\boldsymbol{K}}{\partial x} &= k_1^1 S_0^0 + k_2^1 S_1^0 + \left(2k_2^2 - k_2^0\right) S_1^1 + k_2^{-2} S_1^{-1} + k_3^1 S_2^0 \\
&\quad + \left(2k_3^2 - 3k_3^0\right) S_2^1 + k_3^{-2} S_2^{-1} + \left(3k_3^3 - \frac{1}{4}k_3^1\right) S_2^2 \\
&\quad + \left(6k_3^{-3} - \frac{1}{2}k_3^{-1}\right) S_2^{-2} + k_4^1 S_3^0 + \left(2k_4^2 - 6k_4^0\right) S_3^1 \\
&\quad + k_4^{-2} S_3^{-1} + \left(3k_4^3 - \frac{3}{4}k_4^1\right) S_3^2 + \left(6k_4^{-3} - \frac{3}{2}k_4^{-1}\right) S_3^{-2} \\
&\quad + \left(4k_4^4 - \frac{1}{6}k_4^2\right) S_3^3 + \left(k_4^{-4} - \frac{1}{12}k_4^{-2}\right) S_3^{-3} \\
\frac{\partial\boldsymbol{K}}{\partial y} &= k_1^{-1} S_0^0 + k_2^{-1} S_1^0 + k_2^{-2} S_1^1 + \left(-2k_2^2 - k_2^0\right) S_1^{-1} + k_3^{-1} S_2^0 \\
&\quad + k_3^{-2} S_2^1 + \left(-2k_3^2 - 3k_3^0\right) S_2^{-1} + \left(3k_3^{-3} - \frac{1}{4}k_3^{-1}\right) S_2^2 \\
&\quad + \left(-6k_3^3 - \frac{1}{2}k_3^1\right) S_2^{-2} + k_4^{-1} S_3^0 + k_4^{-2} S_3^1 \\
&\quad + \left(-2k_4^2 - 6k_4^0\right) S_3^{-1} + \left(3k_4^{-3} - \frac{3}{4}k_4^{-1}\right) S_3^2 \\
&\quad + \left(-6k_4^3 - \frac{3}{2}k_4^1\right) S_3^{-2} + \left(k_4^{-4} + \frac{1}{12}k_4^{-2}\right) S_3^3 \\
&\quad + \left(-4k_4^4 - \frac{1}{6}k_4^2\right) S_3^{-3} \\
\frac{\partial\boldsymbol{K}}{\partial z} &= k_1^0 S_1^0 + 2k_2^0 S_1^0 + k_2^1 S_1^1 + k_2^{-1} S_1^{-1} + 3k_3^0 S_2^0 + 2k_3^1 S_2^1 \\
&\quad + 2k_3^{-1} S_2^{-1} + k_3^2 S_2^2 + k_3^{-2} S_2^{-2} + 4k_4^0 S_3^0 + 3k_4^1 S_3^1 \\
&\quad + 3k_4^{-1} S_3^{-1} + 2k_4^2 S_3^2 + 2k_4^{-2} S_3^{-2} + k_4^3 S_3^3 + k_4^{-3} S_3^{-3}
\end{aligned}$$

If there are multiple positions $\boldsymbol{r}_1, \ldots, \boldsymbol{r_n}$ and the positions are constrained relative to each other (as in the case of the constrained optimisation), then the positions can be a function of a rigid transformation (a rotation and a translation) defined by parameters $\boldsymbol{\tau} = [x_0, y_0, z_0, \theta, \varphi, \rho]$:

$$\boldsymbol{r_i} = \begin{bmatrix} \cos\varphi\cos\rho & \cos\rho\sin\theta\sin\varphi - \cos\theta\sin\rho & \cos\theta\cos\rho\sin\varphi \\ \cos\varphi\sin\rho & \cos\theta\cos\rho + \sin\theta\sin\varphi\sin\rho & -\cos\rho\sin\theta + \cos\theta\sin\varphi\sin\rho \\ -\sin\varphi & \cos\varphi\sin\theta & \cos\theta\cos\varphi \end{bmatrix} \cdot \boldsymbol{r}_{i,0} + \begin{bmatrix} x_0 \\ y_0 \\ z_0 \end{bmatrix}$$

The function $\nabla\boldsymbol{K}(\boldsymbol{r}(\boldsymbol{\tau}))$ can now be calculated with respect to $\boldsymbol{\tau}$, where $\boldsymbol{r}_{i,0}$ is the initial position of position $\boldsymbol{r_i}$. So the Jacobian (for Eq. [6]) is then:

$$\nabla\boldsymbol{F} = (\boldsymbol{K}(\boldsymbol{r}(\boldsymbol{\tau})) - \boldsymbol{f_{meas}})^T \cdot \nabla\boldsymbol{K}(\boldsymbol{r}(\boldsymbol{\tau})) \cdot \nabla\boldsymbol{r}(\boldsymbol{\tau})$$

and the Hessian can be similarly calculated.

REFERENCES

1. Boesch C, Gruetter R, Martin E. Temporal and spatial analysis of fields generated by eddy currents in superconducting magnets: optimization of corrections and quantitative characterization of magnet/gradient systems. Magn Reson Med 1991;20:268–284.
2. Papadakis NG, Martin KM, Pickard JD, Hall LD, Carpenter TA, Huang CL, Gradient preemphasis calibration in diffusion-weighted echo-planar imaging. Magn Reson Med 2000;44:616–624.
3. Fillmer A, Vannesjo SJ, Pavan M, Scheidegger M, Pruessmann KP, Henning A. Fast iterative pre-emphasis calibration method enabling third-order dynamic shim updated fMRI. Magn Reson Med 2016;75:1119–1131.
4. Boer VO, van Vliet G, Luijten PR, Klomp DW. Direct B0 field monitoring and real-time B0 field updating in the human breast at 7 Tesla. Magn Reson Med 2012;67:586–591.
5. Keating B, Ernst T. Real-time dynamic frequency and shim correction for single-voxel magnetic resonance spectroscopy. Magn Reson Med 2012;68:339–1345.
6. Hess AT, Tisdall MD, Andronesi OC, Meintjes EM, van der Kouwe AW. Real-time motion and B0 corrected single voxel spectroscopy using volumetric navigators. Magn Reson Med 2011;66:314–323.
7. Wilm BJ, Duerst Y, Dietrich BE, Wyss M, Vannesjo SJ, Schmid T, Brunner DO, Barmet C, Pruessmann KP. Feedback field control improves linewidths in in vivo magnetic resonance spectroscopy. Magn Reson Med 2014;71:1657–1662.
8. Gruetter R, Boesch C. Fast, noniterative shimming of spatially localized signals. In vivo analysis of the magnetic field along axes. J Magn Reson 1992;96:323–334.
9. Gruetter R. Automatic, localized in vivo adjustment of all first- and second-order shim coils. Magn Reson Med 1993;2:804–811.

10. Shen J, Rycyna RE, Rothman DL. Improvements on an in vivo automatic shimming method (FASTERMAP). Magn Reson Med 1997;38:834–839.
11. Ward HA, Riederer SJ, Jack CR. Real-time autoshimming for echo planar timecourse imaging. Magn Reson Med 2002;48:771–780.
12. Bogner W, Hess AT, Gagoski B, Tisdall MD, van der Kouwe AW, Trattnig S, Rosen B, Andronesi OC. Real-time motion- and B0-correction for LASER-localized spiral-accelerated 3D-MRSI of the brain at 3T. Neuroimage 2014;88:22–31.
13. Saleh MG, Alhamud A, Near J, van der Kouwe AW, Meintjes EM. Volumetric navigated MEGA-SPECIAL for real-time motion and shim corrected GABA editing. NMR Biomed 2016;29:248–255.
14. Barmet C, De Zanche N, Wilm BJ, Pruessmann KP. A transmit/receive system for magnetic field monitoring of in vivo MRI. Magn Reson Med 2009;62:269–276.
15. De Zanche N, Barmet C, Nordmeyer-Massner JA, Pruessmann KP. NMR probes for measuring magnetic fields and field dynamics in MR systems. Magn Reson Med 2008;60:176–186.
16. Barmet C, De Zanche N, Pruessmann KP. Spatiotemporal magnetic field monitoring for MR. Magn Reson Med 2008;60:187–197.
17. Vannesjo SJ, Haeberlin M, Kasper L, Pavan M, Wilm BJ, Barmet C, Pruessmann KP. Gradient system characterization by impulse response measurements with a dynamic field camera. Magn Reson Med 2013;69:583–593.
18. Romeo F, Hoult DI. Magnetic field profiling: analysis and correcting coil design. Magn Reson Med 1984;1:44–65.
19. Ashburner J, Friston KJ. Nonlinear spatial normalization using basis functions. Hum Brain Mapp 1999;7:254–256.
20. MackKenzie IS, Robinson EM, Wells AN, Wood B. A simple field map for shimming. Magn Reson Med 1987;5:262–268.
21. Sipila P, Greding S, Wachutka G, Wiesinger F. 2H transmit–receive NMR probes for magnetic field monitoring in MRI. Magn Reson Med 2011;65:1498–1506.
22. Avdievich NI. Transceiver-phased arrays for human brain studies at 7T. Appl Magn Reson 2011;41:483–506.
23. Tofts PS. Quality assurance, accuracy, precision and phantoms. In: Tofts PS ed. Quantitative MRI of the Brain: Measuring Changes Caused by Disease. Chichester, UK: John Wiley & Sons; 2003.
24. McClurg G. Magnetic field distributions for a sphere and for an ellipsoid. Am J Phys 1956;24:496–499.
25. Andersen M, Hanson LG, Madsen KH, Wezel J, Boer VO, van der Velden T, van Osch MP, Klomp D, Webb AG, Maarten JV. Measuring motion-induced B0-fluctuations in the brain using field probes. Magn Reson Med 2016;75:2020–2030.
26. Juchem C, Muller-Bierl B, Schick F, Logothetis NK, Pfeuffer J. Combined passive and active shimming for in vivo MR spectroscopy at high magnetic fields. J Magn Reson 2006;183:278–289.
27. Chang P, Nassirpour S, Henning A. Modeling real shim fields for very high degree (and order) B0 shimming of the human brain at 9.4T. Magn Reson Med 2018;79:529–540.

PUBLICATION 3

Received: 27 October 2017 | Revised: 21 March 2018 | Accepted: 12 April 2018

DOI: 10.1002/mrm.27343

FULL PAPER

Magnetic Resonance in Medicine

Comparison of prospective head motion correction with NMR field probes and an optical tracking system

Martin Eschelbach[1] | Ali Aghaeifar[1] | Jonas Bause[1] | Jonas Handwerker[2,3] | Jens Anders[2,3] | Eva-Maria Engel[4] | Axel Thielscher[1,5,6] | Klaus Scheffler[1,7]

[1] Max Planck Institute for Biological Cybernetics, Tuebingen, Germany

[2] Institute of Microelectronics, University of Ulm, Ulm, Germany

[3] Institute of Smart Sensors, University of Stuttgart, Stuttgart, Germany

[4] Department of Prosthodontics, Center of Dentistry, Oral Medicine, and Maxillofacial Surgery, University Hospital Tuebingen, Germany

[5] Department of Electrical Engineering, Technical University of Denmark, Lyngby, Denmark

[6] DRCMR, Copenhagen University Hospital Hvidovre, Hvidovre, Denmark

[7] Department for Biomedical Magnetic Resonance, University of Tuebingen, Tuebingen, Germany

Correspondence
Martin Eschelbach, Max-Planck-Ring 11, 72076 Tuebingen, Germany.
Email: martin.eschelbach@tuebingen.mpg.de

Funding information
This work was supported by the Deutsche Forschungsgemeinschaft (DFG) grants SCHE658/4 and TH1330/5

Purpose: The aim of this study was to compare prospective head motion correction and motion tracking abilities of two tracking systems: Active NMR field probes and a Moiré phase tracking camera system using an optical marker.

Methods: Both tracking systems were used simultaneously on human subjects. The prospective head motion correction was compared in an MP2RAGE and a gradient echo sequence. In addition, the motion tracking trajectories for three subjects were compared against each other and their correlation and deviations were analyzed.

Results: With both tracking systems motion artifacts were visibly reduced. The precision of the field probe system was on the order of 50 µm for translations and 0.03° for rotations while the camera's was approximately 5 µm and 0.007°. The comparison of the measured trajectories showed close correlation and an average absolute deviation below 500 µm and 0.5°.

Conclusion: This study presents the first in vivo comparison between NMR field probes and Moiré phase tracking. For the gradient echo images, the field probes had a similar motion correction performance as the optical tracking system. For the MP2RAGE measurement, however, the camera yielded better results. Still, both tracking systems substantially decreased image artifacts in the presence of subject motion. Thus, the motion tracking modality should be chosen according to the specific requirements of the experiment while considering the desired image resolution, refresh rate, and head coil constraints.

KEYWORDS
head motion, prospective, motion correction, field probes, tracking, Moiré phase tracking

1 | INTRODUCTION

Subject motion is a major problem in functional and anatomical head MRI. The resulting artifacts such as ghosting and blurring may complicate image interpretation, or in the worst case, render acquired images useless. Thus, measurements have to be repeated or entire patient populations, such as elderly or pediatric patients, have to be excluded from certain

studies. Furthermore, the high spatial resolution achievable with ultra-high field MRI scanners might be limited by the range of involuntary motion even in trained, cooperative subjects.

Many different methods have been proposed to overcome this obstacle.[1] Retrospective motion correction methods[2-4] use the acquired data and try to eliminate motion artifacts with approaches such as image co-registration or entropy-based methods.[5] While there are manifold powerful retrospective motion correction methods available, inconsistently sampled k-space data and spin-history effects can limit the ability of those methods to eliminate motion artifacts in the images. In addition, especially the coregistration-based methods require multiple shots of the same volume to work which is usually only applicable for functional imaging. Prospective motion correction (PMC), on the other hand, uses a motion tracking modality of choice to continuously update the orientation and position of the FOV during data acquisition.[6] Those tracking modalities include MR-based methods such as navigators[7,8] or external tracking devices such as NMR markers[9] and optical tracking devices.[10] The latter two will be briefly discussed subsequently.

Optical tracking with camera(s) have become an established tool in prospective head motion correction. Those devices demonstrated a high accuracy, fast sampling rate and are almost independent from the imaging sequence. However, they require direct line of sight to an optical target or the subject's face[11] and a cross-calibration to convert camera coordinates to scanner coordinates. In addition, they are still expensive, mainly due to the demanding hardware such as a shielded, MR-compatible camera. In contrast, NMR markers such as NMR field probes (FPs)[12,13] are an alternative that does not require a line of sight and naturally operates in the scanner coordinate system. However, the tracking of NMR markers usually requires additional tracking gradients in all three gradient axes, which can be implemented as a separate gradient block,[9] as a modification of imaging gradients[14] or as recently demonstrated, even with the unmodified native imaging gradients.[15] NMR FPs have already successfully been used for prospective head motion correction,[14,15] but to the authors' knowledge, there has not been any comparison of FP-based PMC against other methods available. This work compares the prospective head motion correction capabilities of an optical Moiré phase tracking (MPT) camera-marker system[10] and ^{19}F NMR FPs[15] in healthy volunteers.

2 | METHODS

2.1 | Motion tracking with NMR FPs

The FP motion tracking setup consisted of four custom built NMR magnetometers (Figure 1A). Each magnetometer contained a glass capillary tube (inner diameter 0.8 mm) filled with hexafluorobenzene (C_6F_6) as an NMR active sample and a copper solenoid (inner diameter 1 mm; length $\sim$ 2 mm; six turns) wound around it. To decrease line broadening due to the susceptibility mismatch between air and copper,[12] the tubes were embedded in an ellipsoid epoxy casing (radii: $\sim$1.5 cm and $\sim$1 cm), which was susceptibility matched to the copper wire. The probe head was attached to a tuning and matching circuit. It was designed as a transmit/receive system, such that excitation of the sample and signal reception was performed by the same microcoil. The received signals of the FPs were processed by a custom-built printed circuit board (PCB), which was connected to the probes by means of a short (25 cm) coaxial cable. The PCB hosted a low noise amplifier for the received signal, a power amplifier for transmission and a phase locked loop to set the frequency of the transmit RF pulse and to demodulate the received signal. A more detailed description of the electronics can be found in Handwerker et al.[16] The PCB was powered from an external source outside the scanner room. A standard twisted pair Ethernet cable was used for transmitting all signals from and to the board including the reference frequency for RF transmission and signal demodulation, the trigger for switching between transmit and receive mode and the demodulated FP signal.

The received demodulated low frequency signal coming from the PCB was digitized by an analog-to-digital converter (National Instruments, Austin, TX) with 2 MS/s per channel and 16-bit resolution. An in house developed LabVIEW (National Instruments, Austin, TX) program was used to process the digitized data. It extracted the phase from the complex FID signals and also calculated the position of the FPs. The determination of the FP position in respect to the isocenter of the scanner was realized by switching bipolar gradients on all three axes (Figure 1B). The tracking gradient block of approximately 4 ms was inserted into the sequence after the readout before the excitation pulse of the next TR to minimize RF interference with the electronics on the board. Each gradient had a length of approximately 1 ms and a strength of 15 mT/m which was found to be the optimal trade-off between tracking precision and signal dephasing in the FP sample. Bipolar gradients were chosen to avoid influences of B_0 changes, for example due to subject breathing or movement, on the position measurement. A linear fit to the phase of the negative and positive plateau $\dot{\varphi}_{\pm(r)}$ (see Figure 1C) was applied to determine the gradient amplitudes $\boldsymbol{g}(\boldsymbol{r})$ at a given FP position $\boldsymbol{r}$. The residual error of the linear fit was used as a measure of the signal quality and to reject noise corrupted measurements. The FP position r was then calculated from the measured gradient amplitudes as:

$$\boldsymbol{\omega}_{\pm(r)} = \dot{\varphi}_{\pm(r)} = \gamma 1 B_0(\boldsymbol{r}) \pm \gamma \boldsymbol{g}(\boldsymbol{r}) + \boldsymbol{\eta} \quad (1)$$

$$\boldsymbol{g}(\boldsymbol{r}) = \frac{\dot{\varphi}_{+(\boldsymbol{r})} - \dot{\varphi}_{-(\boldsymbol{r})}}{2\gamma} \quad (2)$$

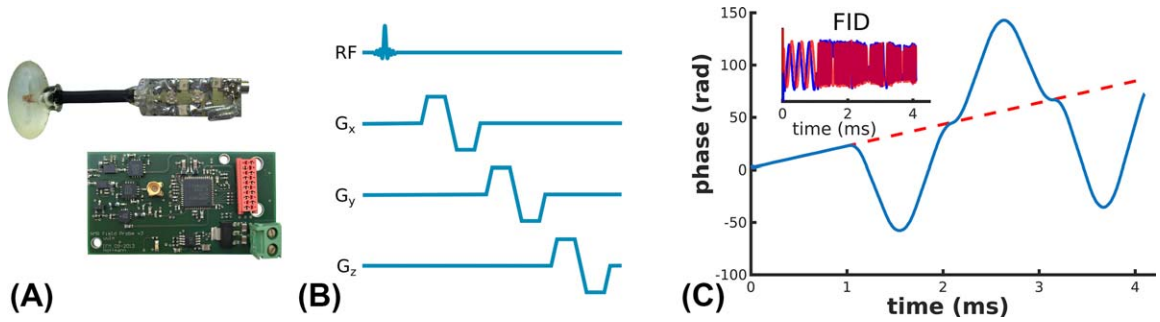

FIGURE 1 A, ^{19}F NMR FP with tuning/matching-circuitry and PCB for signal processing. B, Bipolar gradients used for position tracking of the FPs. C, Corresponding measured phase and FID for one FP when applying three orthogonal bipolar gradients

$$\boldsymbol{g}(\boldsymbol{r}) = \boldsymbol{G}\boldsymbol{r} \tag{3}$$

$$\boldsymbol{r} = \boldsymbol{G}^{-1}\boldsymbol{g}(\boldsymbol{r}) \tag{4}$$

where $\boldsymbol{\omega}_{\pm(\boldsymbol{r})}$ is a vector containing the fitted phase changes acquired during the two gradient lobes at the position $\boldsymbol{r}$ of the FP. γ denotes the gyromagnetic ratio, $1B_0(\boldsymbol{r})$ the identity matrix and the main magnetic field, $\boldsymbol{\eta}$ the measured noise and $\boldsymbol{G}$ a diagonal matrix with the applied gradient strengths along each axis as diagonal entries.

Because the assumption of linear gradients does not hold true for actual gradients and would thus decrease the tracking accuracy of the system, a 3rd order spherical harmonics correction based on the scanner vendor's gradient specifications was implemented into the program which generalizes Equation 3 to the nonlinear version

$$\boldsymbol{g}(\boldsymbol{r}) = \boldsymbol{G}(\boldsymbol{r})\boldsymbol{r} \tag{5}$$

so r can be determined by solving the minimization problem

$$\boldsymbol{r} = \arg\min_{\boldsymbol{r}} \left(\boldsymbol{G}(\boldsymbol{r})\boldsymbol{r} - \boldsymbol{g}(\boldsymbol{r}) \right), \tag{6}$$

with a starting value of $\boldsymbol{r}$ calculated from the linear Equation 4. In addition to that, no further calibration or gradient characterization was implemented to determine the FP positions. The calculated FP positions were used to derive the translation of the FPs' geometric center and the rotation using an algorithm proposed by Umeyama.[17] The data acquisition and processing including the position calculation for four FPs took approximately 70 ms.

Previous experiments have already evaluated the precision[18] and long-term stability of motion tracking with the used FP setup. The tracking precision, defined as the standard deviation of the tracking noise, for translational motion was measured to be 60 µm, 64 µm, and 54 µm along the x-, y-, and z-axis, respectively, while the rotation could be resolved to a precision of 0.026° (average standard deviation). Long-term stability experiments revealed a drift of 71 µm and 0.006° over a time span of approximately 50 min which is in the same order of magnitude as the precision and in principle also allows the usage in scans with longer acquisition times. The precision values for NMR FPs found in recent literature[14] are even lower and amount to 6.1 µm, 6.3 µm, 10.5 µm along x, y, and z, respectively, as well as 0.003°, 0.004°, 0.004° for rotation around x-, y-, and z-axis, respectively, at a field strength of 7T.

2.2 | MPT motion tracking

The optical tracking system is commercially available (Kineticor Inc, HI), and consists of a camera attached to the top of the scanner bore (Figure 2B) and a reflective $15 \times 15\,\text{mm}^2$ MPT marker (Figure 2A). This setup allows for the estimation of all six motion parameters with a single camera with a frame-rate of 85 Hz (for details see Maclaren et al[10] and Stucht et al).[19]

The precision of the MPT tracking system according to literature[10] is 1 µm, 12 µm, and 1 µm in the scanner x, y, and z directions, respectively, and better than 0.01° in all three rotations which was approximately confirmed in our own experiments[18] with results of 6 µm, 2 µm, 5 µm and 0.006°, 0.008°, 0.006°, respectively.

Because the camera detects marker motion in its own coordinate system, a cross-calibration is needed to convert the measured data from camera coordinates to the scanner coordinate system. The calibration procedure involves moving a structured phantom with a rigidly attached MPT marker. The motion in scanner coordinates is calculated with a co-registration method while the same motion is also recorded with the camera. With at least three different phantom positions, it is possible to calculate the cross-calibration.[20] With more motion repetitions this cross-calibration can be further refined.

2.3 | Sequence update

Both systems, FPs and camera-based motion tracking, require an external PC that sends the calculated motion parameters to the scanner by means of User Datagram Protocol. There, it is processed by a custom-built library[21] which has a modular design to adapt to different motion tracking sources. The tracking systems used in this study provide

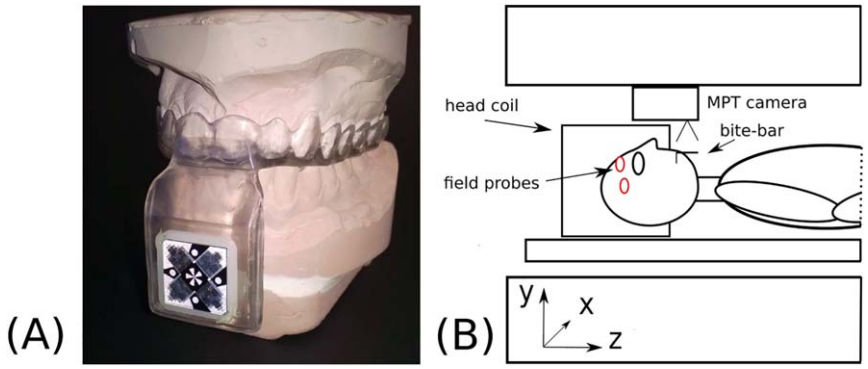

FIGURE 2 A, MPT marker on a custom-made bite-bar. B, Positioning of the MPT tracking camera and the FPs in the scanner bore for a closed coil setup

information about the orientation (rotation matrix $\boldsymbol{R}_i$) and position ($\boldsymbol{p}_i$) of the MPT marker or the geometric center of FPs, respectively. The input is then used to calculate the update of the FOV position and orientation accordingly. The rotation change relative to the initial orientation ($\boldsymbol{R}_{rel}$) can be applied directly to update the FOV. If rigid coupling between the skull and the marker(s) is assumed, a vector $\boldsymbol{v}$ of constant length between the center of the FOV ($\boldsymbol{s}_0$) and the initial marker position $\boldsymbol{p}_0$ can be calculated. This vector and the rotation matrix can then be used to determine the translation $\Delta \boldsymbol{t}$:

$$\boldsymbol{v} = \boldsymbol{s}_0 - \boldsymbol{p}_0 \tag{7}$$

$$\boldsymbol{R}_{rel} = \boldsymbol{R}_i \boldsymbol{R}_0^{-1} \tag{8}$$

$$\Delta \boldsymbol{t} = \boldsymbol{p}_i + \boldsymbol{R}_{rel} \boldsymbol{v} - \boldsymbol{s}_0. \tag{9}$$

If tracking data for one or multiple measurements is not received, no update of the FOV position is performed and the last valid measurement is used. This is also the case for data points considered invalid (translational motion > 50 mm).

2.4 | Motion stage experiment

The MR scanner used in all experiments was a 9.4T human scanner (Siemens Healthcare, Erlangen, Germany) equipped with a whole-body gradient system (SC72).

A custom-built motion stage was used to assess the accuracy of the motion tracking of both systems. The motion stage consisted of a sledge that hosted the MPT marker and a FP (Figure 3). The sledge was mounted onto a threaded rod with an attached MR-compatible sliding caliper to measure the distance traveled by the sledge. The fine scale of the caliper was used to acquire position measurements in 500 µm steps. The MPT marker was moved concurrently with a FP over a total distance of 3 cm and back by turning the screw of the positioning stage inside the scanner bore. For each motion step the position was recorded simultaneously with the FP and the MPT camera. The starting point of the measurement was at around +16 cm off-isocenter in z-direction with direction of the motion approximately along positive z. This position was chosen because it is far enough from the isocenter to also capture nonlinear effects of the gradients in the FP measurements.

2.5 | In vivo experiments

Three healthy volunteers (male, 26–38 years) were measured in accordance to the local ethics protocol using a custom built 16Tx/31Rx head coil.[22] The MPT marker was attached to the subjects on a custom-built bite-bar, specifically designed to fit the unique dental impression of each subject (Figure 2A). This ensures a fairly rigid coupling to any movements of the skull and free line of sight of the camera to the marker, despite the closed coil cover. The FPs were attached to the nose bridge and the temples of the subjects using medical tape to minimize the effect of skin movement on the motion measurement. An additional mount for the FPs (as for example in Haeberlin et al[14] and Aranovitch et al[15] could not be used due to spatial constraints of the receive array.

To compare PMC with both modalities, three subjects were scanned with a 2D gradient echo (GRE) sequence

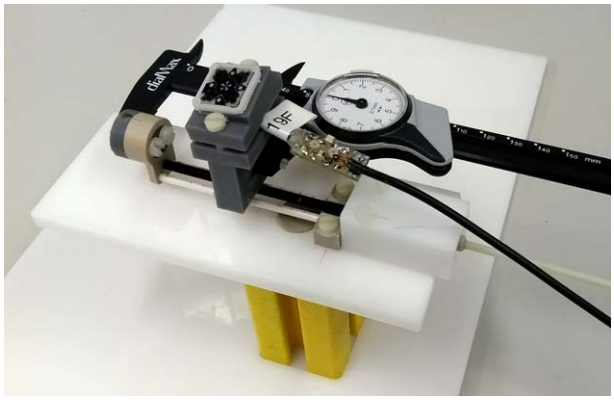

FIGURE 3 Motion stage. The sledge with the MPT marker and an NMR FP can be moved by turning a screw while obtaining exact position information from the caliper

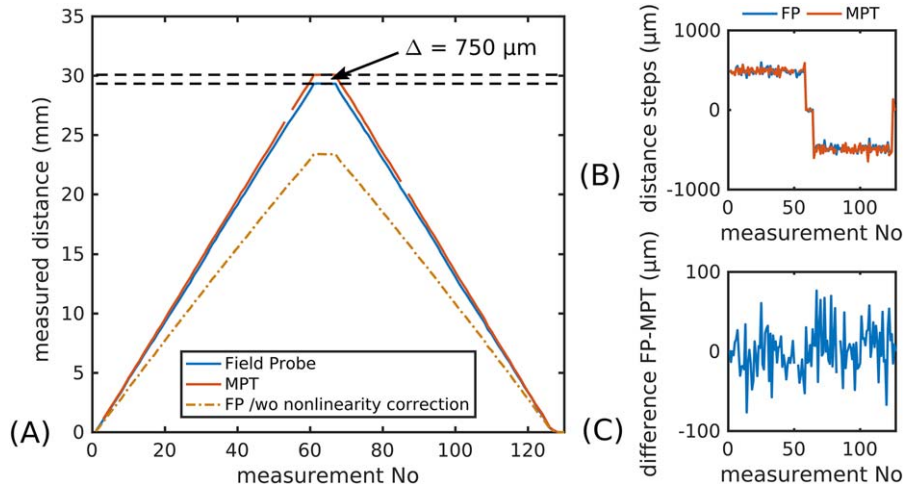

FIGURE 4 Results of the motion stage experiment. A, Measured distance from starting point (approx. + 16 cm from isocenter along z) for both tacking systems. B, Measured distance between successive motion steps. C, Difference of FP and MPT measurements for the distance between successive steps

(matrix: 400×400; resolution: $0.5 \times 0.5 \times 1.6\,mm^3$; slices: 10; slice spacing: 9.6 mm; flip angle: 15°; TA: 1:21 min; TR: 160 ms; TE: 9 ms). Each subject was asked to perform the following motion patterns: no motion, small motion, fast motion, and big motion. Images for each motion pattern were acquired once with no correction, FP correction, and MPT correction, respectively. The sequence motion update was performed every k-space line for the MPT correction but only every fourth line for the FP correction due to the calculation time needed to process the FP data.

For all GRE measurements, no matter whether the prospective correction was enabled or disabled, the motion trajectories were recorded simultaneously with both tracking modalities to compare the recorded trajectories against each other. For the tracking comparison, clear outliers in the motion tracking ($>2\,mm/2°$ between successive tracking steps) were removed during post processing.

Additionally, two subjects were scanned with a whole-brain MP2RAGE[23] sequence (time-resampled frequency-offset corrected inversion,[24] resolution: 0.55 mm isotropic; matrix: $384 \times 384 \times 512$; $FA_{1/2}$: 4°/8°; $TI_{1/2}$: 730/1950 ms; TR: 6 ms; MP2RAGE TR: 5000 ms; TE: 3 ms; GRAPPA: 2×2; 6/8 partial Fourier in secondary phase encoding direction, reconstructed with the projections onto convex sets algorithm; TA: 9.03 min). The MP2RAGE images were acquired with three settings: no correction, FP correction and MPT correction and the subject being instructed to hold still.

In these measurements, the motion update for both, MPT and FP correction, was performed only before each inversion pulse, every 5 s, due to the short readout TR which hampered the implementation of the additional gradient switching required for encoding the FP's position. In addition to the MP2RAGEs, an actual flip angle map,[25] 3.3 mm isotropic, flip angle: 50°, TR1/2: 20/100 ms, GRAPPA: 2×2, TA: 1:20 min) was acquired. This allowed to correct for residual B_1^+ influences caused by the high flip-angle chosen for the MP2RAGE measurements by using the approach described by Hagberg et al.[26]

3 | RESULTS

3.1 | Motion stage

The measured total displacement during the motion stage experiment for both tracking systems is depicted in Figure 4A. The trajectories are very similar but the measured final displacement of 30.08 mm for the MPT tracking and 29.33 mm for the FP yield a difference of 750 µm between both methods. The differences to the ground truth are 80 µm and 670 µm, respectively. While the former is within the precision of the motion stage caliper, the latter likely represents a mismatch of the measured value to the ground truth. In addition, the effect of the correction of gradient nonlinearities is plotted in the uncorrected trajectory of the FPs. Figure 4B shows the displacement difference between successive steps. Here, the measurements of both modalities stay within the motion stage's precision. The difference between both tracking modalities for the measured displacement steps is shown in Figure 4C. The mean absolute difference between both systems amounted to 21 µm.

3.2 | Motion tracking comparison

For a quantitative comparison of the measured trajectories, all motion data-points of the in vivo GRE measurements were compared against each other. Tracking data from 36 scans was used to create a scatter plot of FP tracking versus

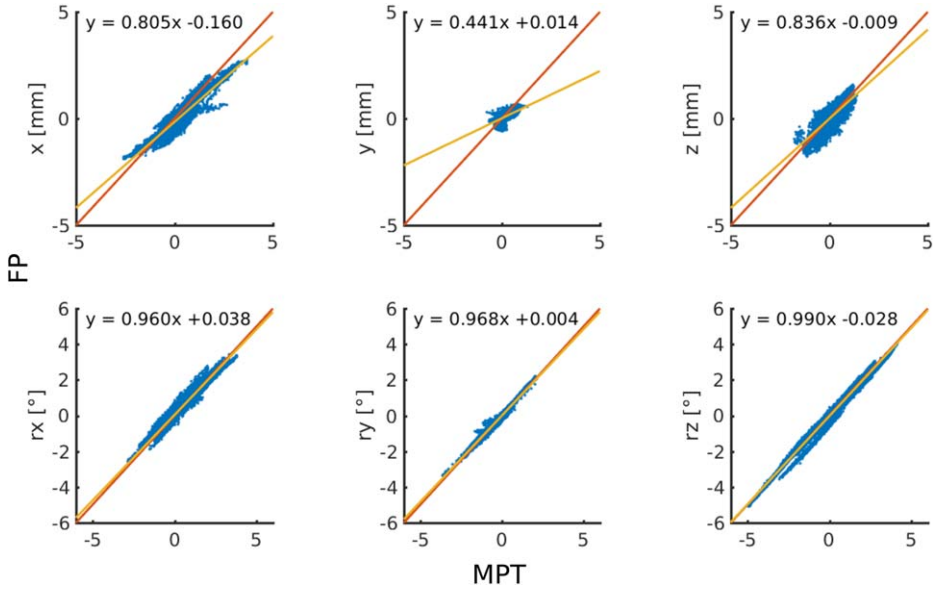

FIGURE 5 Scatter plots of all 6 degrees of freedom for in vivo motion tracking (three subjects, 36 measurements). FP tracking against MPT tracking with linear fit and the red line indicating identity

MPT tracking (Figure 5). The scatter plot shows again the underestimation of translational motion for the FPs compared with the MPT tracking which was already visible in the results of the motion stage experiment (Figure 4). Table 1 summarizes the comparison of the two tracking modalities. The motion range covered by the experiments is a few millimeters in translational motion, with maximum values of -2.59 mm up to + 3.68 mm in x-direction and several degrees of rotational motion with a minimum of -4.95° and a maximum of +4.17°, both around the z-axis. The mean absolute deviation is well below 1 mm/1° for all degrees of freedom even when including the corresponding standard deviations.

However, the maximum absolute deviation for the two systems was 2.02 mm along z and 0.9° around the z-axis. In addition to the slopes calculated from the linear fits in Figure 5, the table also shows the Pearson correlation coefficient, which provides a measure for correlation between two variables with values between -1 and 1, with 1 representing perfect correlation, -1 negative correlation and 0 no detectable correlation at all. The coefficients show positive correlation with a correlation coefficient above 0.9 for all degrees of freedom other than the translations in y and z where the correlation coefficient is only 0.61 and 0.79, respectively.

3.3 | 2D GRE

An exemplary slice of the acquired 2D GRE images of one subject for all 12 imaging conditions along with sample motion trajectories for each motion condition is depicted in Figure 6. A full slice view for all 12 measurements is shown in Supporting Information Figure S1, which is available online. All corresponding motion trajectories for both tracking devices can be found in Supporting Information Figures S2 and S3. The images without voluntary motion show the consistency across all three imaging conditions. There is no visible decrease in image quality when the PMC is enabled

TABLE 1 Motion range (MPT values), maximum absolute difference (Max abs diff), mean absolute deviation (MAD), mean squared deviation (MSD), and corresponding standard deviations (σ) as well as the slopes from Figure 5 and the calculated Pearson correlation coefficients (PCC) for field probes against MPT tracking for the motion experiments across three subjects (36 measurements).

	Motion range	Max abs diff	MAD ± σ	MSD ± σ	Slope	PCC
Tx [mm]	−2.59 − 3.68	2.02	0.23 ± 0.21	0.10 ± 0.17	0.81	0.92
Ty [mm]	−0.78 − 1.30	1.08	0.12 ± 0.10	0.03 ± 0.04	0.44	0.61
Tz [mm]	−1.78 − 1.39	1.26	0.20 ± 0.15	0.06 ± 0.10	0.84	0.79
Rx[°]	−2.85 − 3.81	0.89	0.14 ± 0.13	0.04 ± 0.07	0.96	0.97
Ry [°]	−3.63 − 2.12	0.78	0.07 ± 0.05	0.01 ± 0.02	0.97	0.99
Rz [°]	−4.95 − 4.17	0.90	0.10 ± 0.11	0.02 ± 0.06	0.99	0.99

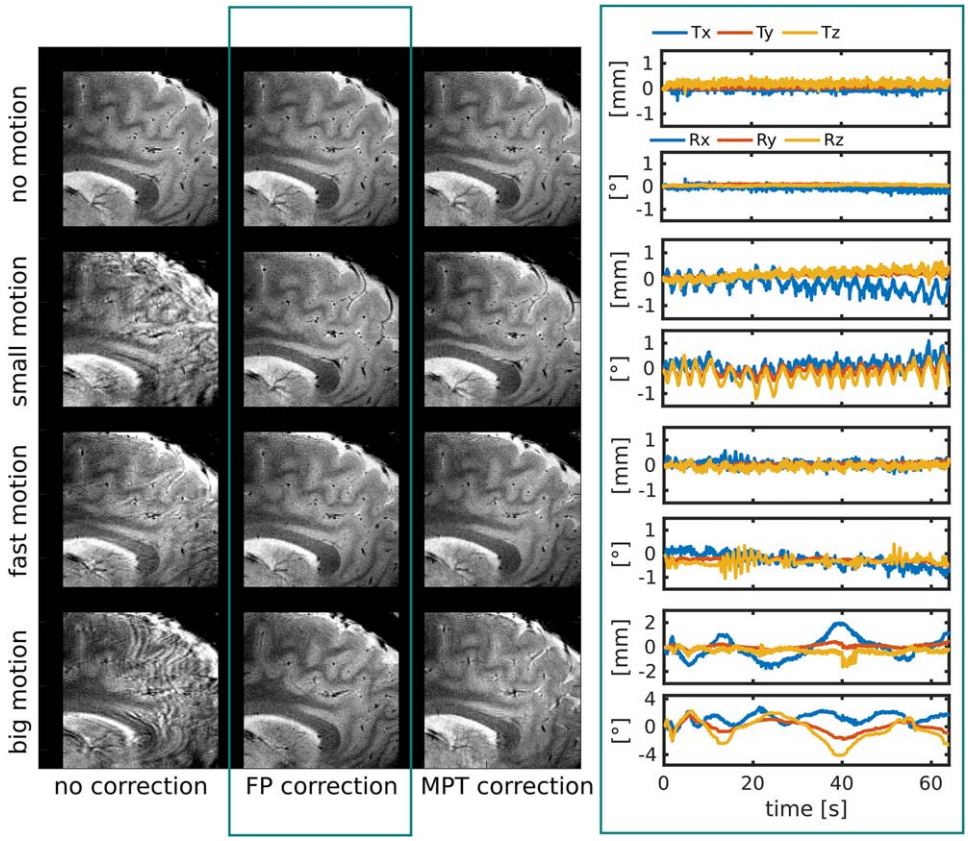

FIGURE 6 2D GRE images with an in-plane resolution of 0.5 mm × 0.5 mm and a through-plane resolution of 1.6 mm. Zoomed images for all 12 imaging conditions in one subject along with one FP motion trajectory for each motion condition. The full slice view of the measurements can be found in Supporting Information Figure S1. The motion trajectories for all 12 measurements are depicted in Supporting Information Figures S2 and S3

(top row in Figure 6). The images acquired with voluntary subject motion (rows 2-4 in Figure 6) clearly show motion artifacts in the uncorrected case which are substantially reduced when enabling PMC with either tracking modality. However, the quality of the corrected images is still a little decreased compared with the images without voluntary motion. This is especially true when looking at images for the case of big motion where remaining motion artifacts are still visible for both correction modalities.

One sample trajectory for both tracking modalities corresponding to the 2D GRE measurement with FP correction and big motion is shown in Figure 7. The lower precision of the FP system is clearly visible in its noisier data. Once more, there is a visible tendency of underestimation of translational motion in the FP data versus the camera measurements, where translations in z-direction show the least correlation between the two tracking systems. There are two types of deviations in Tz: First, short jumps of the trajectory after 22 s and 40 s. Second, diverging trajectories, e.g., during the time intervals from 4 to 7 s, 17 to 26 s, and 46 to 54 s. One can also see that there are a few missing data points in the camera trajectory. Missing data and tracking errors of the camera typically stem from reflections of the camera light on the marker that occur when it is orthogonal to the light beam. Thus, the marker is usually slightly tilted to avoid reflections. However, reflections might still occur for larger head rotations. Besides that, both trajectories match well, especially for rotational motion.

3.4 | MP2RAGE

Figure 8 shows a slice for the MP2RAGE measurements in one subject using three different motion correction settings. The range of motion in all three measurements was very similar as shown in the corresponding motion trajectories captured by the MPT camera system. The images for the second subject are not shown here because the captured motion range varied more between the individual scans (the images can be found in Supporting Information Figure S4). In the displayed measurements, upon closer inspection, the FP corrected image shows an improvement over the uncorrected case but does not quite reach the quality of the MPT corrected image. The final head position during the measurement with FP correction deviated by -0.32 mm, -0.34 mm, and -0.50 mm along x, y, and z, respectively, and -0.49°, -0.14°, and 0.24° around x, y, and z, respectively, from the simultaneously acquired camera data.

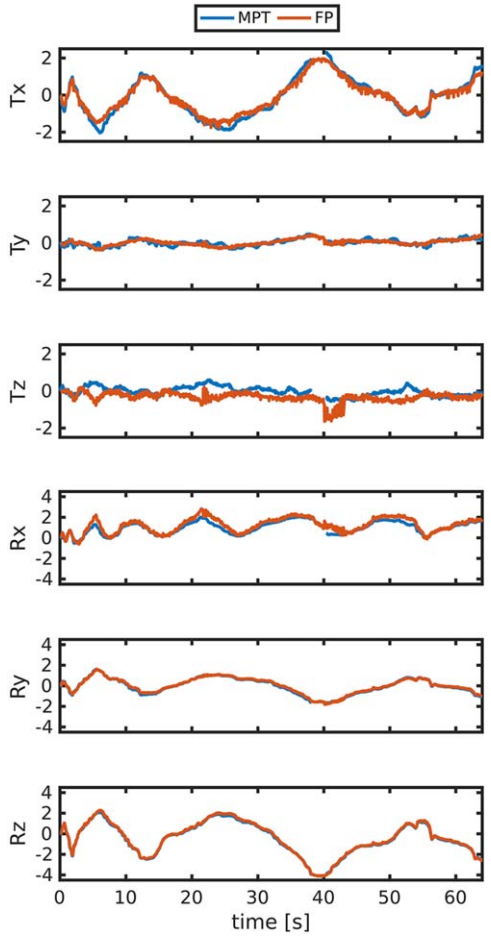

FIGURE 7 Motion trajectory for both tracking modalities from the 2D GRE measurement with big motion and FP correction in Figure 6. Outliers in the MPT tracking have been removed for better visualization; they are shown in the corresponding trajectory of Supplementary Information Figure 3

4 | DISCUSSION

The motion stage experiment showed that the displacements between successive steps determined with the FPs agreed very well with the measurements from the camera as well as with the ground truth from the motion stage. However, for large motion and positions of the FPs far away from the isocenter, the 3rd order nonlinearity correction does not seem to be sufficient anymore. But with the FPs usually being closer to the isocenter when attached to the head and translations of 3 cm being an example of extreme motion, it is not expected that this deviation affects the prospective correction to a large extend in most usage scenarios. But this still shows that an accurate gradient characterization remains crucial for the exact position determination of the FPs and a gradient characterization beyond the vendor's specifications, e.g., by measuring its full impulse response function,[27] might further improve the accuracy of the tracking results. However, such measurements would ideally require a field camera that was not available for this study.

The results of the motion tracking comparison revealed a close agreement in measured rotational motion while translational motion tended to be underestimated by the FPs in comparison to MPT tracking.

There are several reasons for the remaining discrepancies between both systems. Because both motion tracking methods are marker based, a rigid attachment of the respective marker(s) is an important factor for the accuracy and stability of the measurements. Unwanted FP motion can occur due to residual motion of the skin, stretching or loosening of the tape used to fixate the probes or due to single probes hitting parts of the receive helmet. Therefore, an attachment of the FPs to the bite-bar has also been tested. But in this configuration, the inherent noise of the FP position measurements was leveraged by the longer distance to the imaging region. Thus, it was found to be the best solution if the FPs were placed as close as possible to the imaged region.

The geometrical configuration of the FPs will also influence the measurements. Ideally, they would be arranged in a regular tetrahedral manner to cover all rotational axes with the same precision. But in a realistic setup within a tight fitting receive helmet, the configuration will be less precise for one or more axes. In our case, the Rx values are a little more scattered as visible in Figure 5. This in turn will also influence the variance of Ty and Tz (see Equation 9) and explains why their correlation coefficients are lower. For Ty, in addition, the overall range of motion was rather small which can be explained by the limited available space along that direction inside the receive helmet. Thus, the performed motion is already very close to the precision limit of the FPs.

Apart from the aforementioned gradient nonlinearity as a source for tracking discrepancies, there is also the remaining noise in the FP measurements that leads to a decreased precision in their position determination. Parts of the noise were already removed by demodulating the signal in the scanner and low-pass-filtering the demodulated signal before digitization as well as rejecting some of the noisy measurements. However, further improvements may be achieved by increasing the sample size of the FPs or using short-lived probes[15] to increase SNR.

In contrast to the FPs, the camera accuracy mainly depends on the quality of the cross-calibration[28] and invalid measurements were typically caused by reflections of the camera light on the MPT marker. In addition, the marker can also move out of the camera's field of view or be obscured by the coil which will lead to missing tracking data as well.

The motion corrected 2D GRE images show the ability of both, the MPT system and the FP-based motion correction, to substantially reduce motion artifacts in the presence of subject motion. The tracking differences especially for measured translational motion are not visibly translated in a decreased image quality. One reason might be that natural head motion mainly consists of rotations while translational

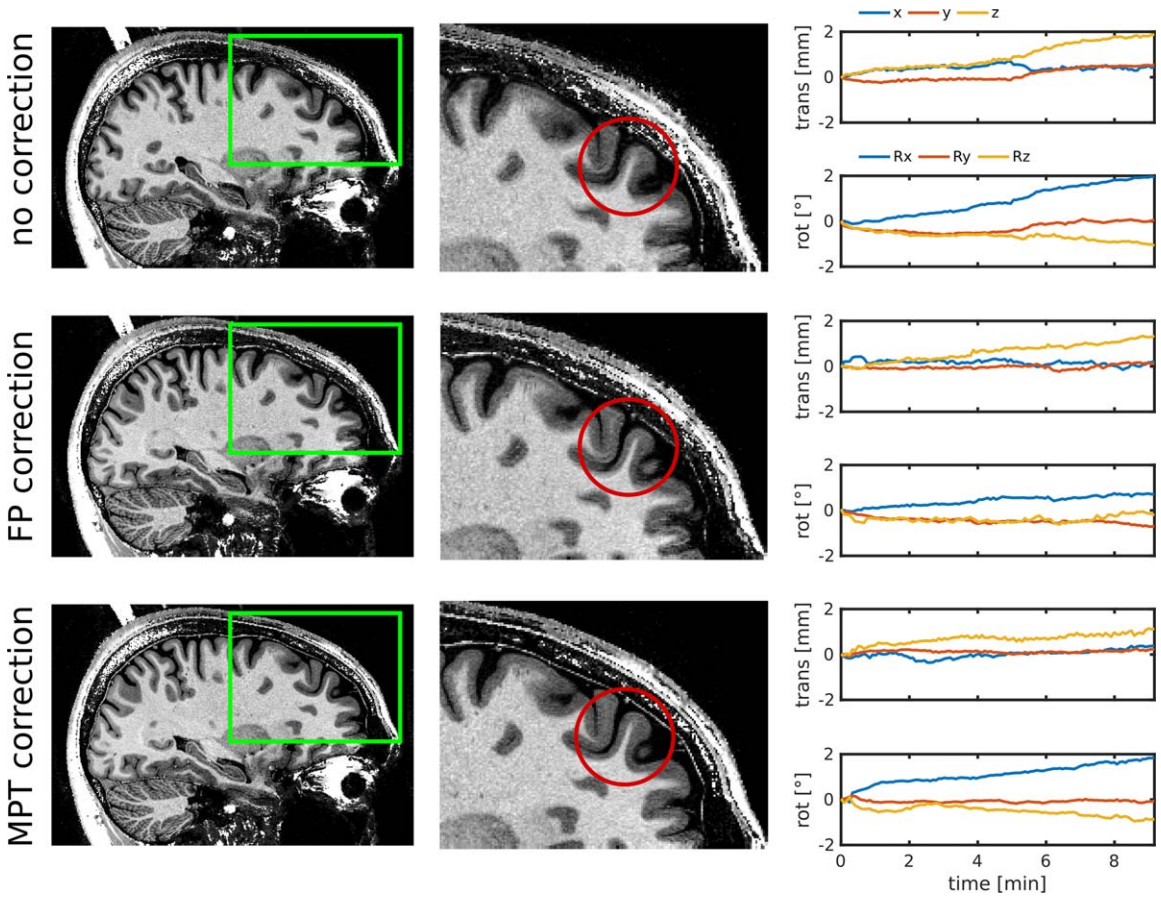

FIGURE 8 MP2RAGE images (0.5 mm^3 isotropic, acquisition time 9:03 min) for three motion correction conditions with corresponding motion trajectories acquired with the camera

motion tends to be small. Also, the mean absolute deviation between camera and FPs for the translational motion (see Table 1) was still below half the voxel size.

The displayed motion trajectory (Figure 7) shows that the general motion pattern in terms of magnitude and direction is very similar for both tracking modalities. However, some of the limitations of the FP tracking system that have been described above can also be detected here. The short jumps of the Tz trajectory are caused by a FP hitting the receive helmet, because they also coincide with the time points of maximal head rotation around z in that measurement. Then there are short intervals when the Tz trajectories start to diverge. If we look at the trajectories of Rx during those same intervals, we notice that there is a slight overestimation of the values measured by the FPs compared with the camera trajectory. Because these values are also used for the calculation of translational motion (see Equation 9), this leads to the divergence of the Tz trajectories during those intervals.

For the MP2RAGE measurements the improvement in image quality for both correction methods is clearly visible. Here, however, the camera corrected images show a higher quality than the ones corrected with the FPs. During the longer measurement it is more likely for the FPs' locations to move due to nonrigid attachment to the skin. But still the calculated tracking deviation between the two systems for the final head position was only in the order of a voxel size. Overall, the FP measurements still proved sufficient to substantially increase image quality compared with the uncorrected case.

Because all measurements were carried out at a field strength of 9.4T, one might argue that there is an SNR advantage which might increase the precision of the FP measurements compared with experiments at scanners with a lower field strength. But it has been shown that a comparable precision can be also attained at 3T systems.[14]

One drawback of our implementation of FP motion correction is the necessity of altering the sequence and the need for additional time in each TR for implementing the tracking gradients as well as for processing the FP data. But as recent work has shown, it is also possible to use the imaging gradients for encoding the FP position.[15] The processing time could possibly be decreased further by outsourcing parts of the LabVIEW code to an implementation with a faster programming language.

Advantages of the FPs include the lack of a cross-calibration procedure and the fact that no line of sight to a target is needed, thus there is no need for a bite-bar even in closed coil setups. This increases subject comfort according

to the subjects participating in this study. On the other hand, one still has to attach the FPs to the subject's head which again reduces comfort and currently remains a time-consuming procedure, therefore, still preventing an application in clinical environments. In addition, the signal transmission and power supply to the PCBs still requires a set of cables. Moving to wireless[29] or optical transmission would increase the applicability in a clinical setup.

In conclusion, even though the inherent precision of our implementation of FP based tracking is 1 order of magnitude worse than the MPT camera systems' (approx. 50 µm versus 5 µm, 0.03° versus 0.007°), for an imaging resolution well above the precision limit (voxel size $0.5 \times 0.5 \times 1.6\,mm^3$), both systems performed similarly well regarding the quality of the motion corrected 2D GRE images. For the MP2RAGE measurements, however, the MPT system performed better probably due to FP motion during the longer acquisition time. Image quality was nevertheless improved substantially for both motion correction methods. While there is still room for improvement in the precision and calculation time of NMR FP tracking, the most crucial point for reliable prospective head motion correction remains to be the rigid attachment of the respective tracking markers to the skull. If this is taken into account, FPs can be a suitable alternative to optical tracking systems especially when considering recent advances in precision and the use of imaging gradients for position encoding.[15] In addition, there are further possible applications of FPs, such as field monitoring[30] or collecting physiological data,[31] which could be obtained from the concurrently measured B_0 component of the signal.

ORCID

Martin Eschelbach http://orcid.org/0000-0003-3600-1526
Ali Aghaeifar http://orcid.org/0000-0002-6964-0992

REFERENCES

[1] Godenschweger F, Kägebein U, Stucht D, et al. Motion correction in MRI of the brain. *Phys Med Biol*. 2016;61:R32-R56.

[2] Morgan VL, Dawant BM, Li Y, Pickens DR. Comparison of fMRI statistical software packages and strategies for analysis of images containing random and stimulus-correlated motion. *Comput Med Imaging Graph*. 2007;31:436-446.

[3] Batchelor PG, Atkinson D, Irarrazaval P, Hill DLG, Hajnal J, Larkman D. Matrix description of general motion correction applied to multishot images. *Magn Reson Med*. 2005;54:1273-1280.

[4] Atkinson D, Hill DLG, Stoyle PNR, et al. Automatic compensation of motion artifacts in MRI. *Magn Reson Med*. 1999;41:163-170.

[5] Loktyushin A, Nickisch H, Pohmann R, Schölkopf B. Blind retrospective motion correction of MR images. *Magn Reson Med*. 2013;70:1608-1618.

[6] Maclaren J, Herbst M, Speck O, Zaitsev M. Prospective motion correction in brain imaging: A review. *Magn Reson Med*. 2013;69:621-636.

[7] Van Der Kouwe AJW, Benner T, Dale AM. Real-time rigid body motion correction and shimming using cloverleaf navigators. *Magn Reson Med*. 2006;56:1019-1032.

[8] Welch EB, Manduca A, Grimm RC, Ward HA, Jack CR Jr. Spherical navigator echoes for full 3D rigid body motion measurement in MRI. *Magn Reson Med*. 2002;47:32-41.

[9] Ooi MB, Krueger S, Thomas WJ, Swaminathan SV, Brown TR. Prospective real-time correction for arbitrary head motion using active markers. *Magn Reson Med*. 2009;62:943-954.

[10] Maclaren J, Armstrong BSR, Barrows RT, et al. Measurement and correction of microscopic head motion during magnetic resonance imaging of the brain. *PLoS One*. 2012;7:e48088.

[11] Maclaren J, Kyme A, Aksoy M, Zahneisen B, and Bammer R. Markerless optical tracking for motion correction in MR and PET/MR imaging of the brain. In Proceedings of the 25th Annual Meeting of ISMRM, Honolulu, HI, 2017. Abstract 1292.

[12] De Zanche N, Barmet C, Nordmeyer-Massner JA, Pruessmann KP. NMR probes for measuring magnetic fields and field dynamics in MR systems. *Magn Reson Med*. 2008;60:176-186.

[13] Barmet C, De Zanche N, Wilm BJ, Pruessmann KP. A transmit/receive system for magnetic field monitoring of in vivo MRI. *Magn Reson Med*. 2009;62:269-276.

[14] Haeberlin M, Kasper L, Barmet C, et al. Real-time motion correction using gradient tones and head-mounted NMR field probes. *Magn Reson Med*. 2015;74:647-660.

[15] Aranovitch A, Haeberlin M, Gross S, et al. Prospective motion correction with NMR markers using only native sequence elements. *Magn Reson Med*. 2018;79:2046-2056.

[16] Handwerker J, Eschelbach M, Chang P, et al. An active TX/RX NMR probe for real-time monitoring of MRI field imperfections. In Proceedings of the Biomedical Circuits and Systems Conference (BioCAS), 2013 IEEE, Rotterdam, Netherlands, 2013. pp. 194-197.

[17] Umeyama S. Least-squares estimation of transformation parameters between two point patterns. *IEEE Trans Pattern Anal Mach Intell*. 1991;13:376-380.

[18] Eschelbach M, Loktyushin A, Chang P, et al. A Comparison of 19F NMR Field probes and an optical camera system for motion tracking. In Proceedings of the 24th Annual Meeting of ISMRM, Singapore, 2016. Abstract 0340.

[19] Stucht D, Danishad KA, Schulze P, Godenschweger F, Zaitsev M, Speck O. Highest resolution in vivo human brain MRI using prospective motion correction. *PLoS One*. 2015;10:1-17.

[20] Zahneisen B, Lovell-Smith C, Herbst M, et al. Fast noniterative calibration of an external motion tracking device. *Magn Reson Med*. 2013;1500:1489-1500.

[21] Aghaeifar A, Eschelbach M, Bause J, Thielscher A. Scheffler K. AMoCo, a software package for prospective motion correction. In Proceedings of the 25th Annual Meeting of ISMRM, Honolulu, HI, 2017. Abstract 0305.

[22] Shajan G, Kozlov M, Hoffmann J, Turner R, Scheffler K, Pohmann R. A 16-channel dual-row transmit array in combination

with a 31-element receive array for human brain imaging at 9.4 T. *Magn Reson Med*. 2013;71:870-879.

[23] Marques JP, Kober T, Krueger G, van der Zwaag W, Van de Moortele PF, Gruetter R. MP2RAGE, a self bias-field corrected sequence for improved segmentation and T1-mapping at high field. *NeuroImage*. 2010;49:1271-1281.

[24] Hurley AC, Al-Radaideh A, Bai L, et al. Tailored RF pulse for magnetization inversion at ultrahigh field. *Magn Reson Med*. 2010;63:51-58.

[25] Yarnykh VL. Actual flip-angle imaging in the pulsed steady state: a method for rapid three-dimensional mapping of the transmitted radiofrequency field. *Magn Reson Med*. 2007;57:192-120

[26] Hagberg G, Bause J, Ethofer T, et al. Whole brain MP2RAGE-based mapping of the longitudinal relaxation time at 9.4T. *NeuroImage*. 2016;144:203-216.

[27] Vannesjo SJ, Haeberlin M, Kasper L, et al. Gradient system characterization by impulse response measurements with a dynamic field camera. *Magn Reson Med*. 2013;69:583-593.

[28] Zahneisen B, Keating B, Ernst T. Propagation of calibration errors in prospective motion correction using external tracking. *Magn Reson Med*. 2014;72:381-388.

[29] Ooi MB, Aksoy M, Maclaren J, Watkins RD, Bammer R. Prospective motion correction using inductively coupled wireless RF coils. *Magn Reson Med*. 2013;70:639-647.

[30] Vionnet L, Aranovitch A, Duerst Y, et al. Simultaneous prospective motion correction and feedback field control: T2* Weighted imaging at high field. In Proceedings of the 25th Annual Meeting of ISMRM, Honolulu, 2017. Abstract 306.

[31] Gross S, Vionnet L, Kasper L, Dietrich BE, Pruessmann KP. Physiology recording with magnetic field probes for fMRI denoising. *Neuroimage*. 2017;154:106-114.

SUPPORTING INFORMATION

Additional Supporting Information may be found in the online version of this article.

FIGURE S1 Full slice view for all twelve imaging conditions for the 2D GRE measurements in Figure 6.

FIGURE S2 Field probe motion trajectories for all twelve motion and correction combinations for the 2D GRE measurements in Figure 6. For the no motion measurements, in two cases the field probe measurement was delayed (grey boxes on the left and right). There is also one measurement with a tracking error (grey box in the middle).

FIGURE S3 MPT motion trajectories for all twelve motion and correction combinations for the 2D GRE measurements in Figure 6. A few exemplary tracking errors and missing tracking data is highlighted in the grey boxes.

FIGURE S4 MP2RAGE images of the second subject ($0.5\,mm^3$ isotropic, acquisition time 9:03 min) for three motion correction conditions with corresponding motion trajectories acquired with the camera. Here, the involuntary head motion varies more between scans.

How to cite this article: Eschelbach M, Aghaeifar A, Bause J, et al. Comparison of prospective head motion correction with NMR field probes and an optical tracking system. *Magn Reson Med*. 2019;81:719–729. https://doi.org/10.1002/mrm.27343